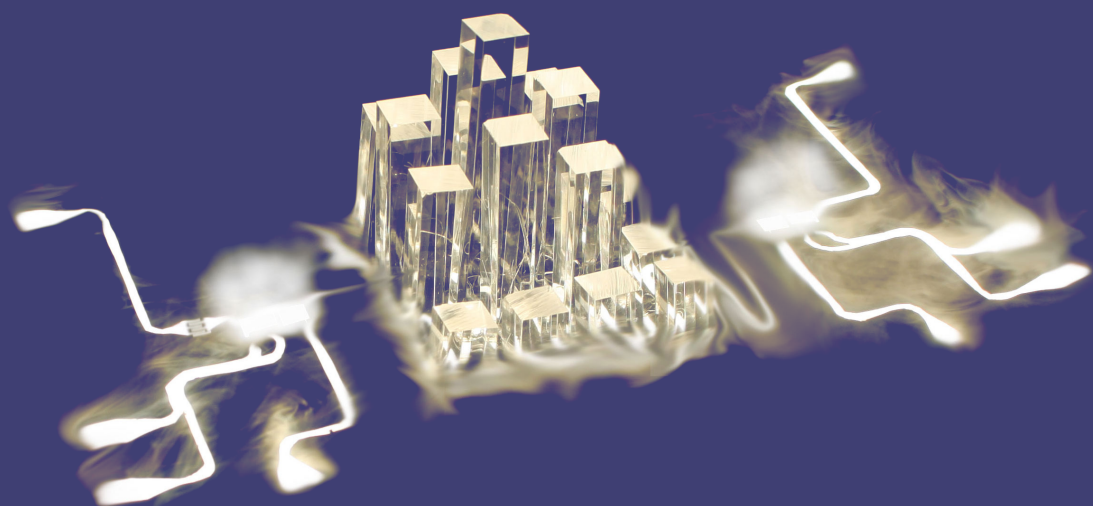# Resonant Collective Interactions in Circuit Quantum Electrodynamics

Jonas Mlynek

DISS. ETH NO. 22099

Resonant Collective Dynamics in Circuit Quantum Electrodynamics

A dissertation submitted to

ETH ZURICH

for the degree of

Doctor of Sciences

presented by

Jonas Mlynek

Dipl. Phys., FU Berlin

born August 12, 1984

citizen of Germany

accepted on the recommendation of

Prof. Dr. Andreas Wallraff, examiner
Dr. Patrice Bertet, co-examiner

2014

Abstract

The coupling of superconducting qubits to coplanar transmission line resonators has proven to be a fertile system to study the fundamental aspects of light-matter interaction.

A major advantage of this particular physical implementation is that the system's key parameters that govern the interaction can be designed in advance and fabrication is achieved under highly controllable conditions. Moreover coupling constants can be realized with very high accuracy, which allows to observe collective effects so far difficult to observe other system. Especially those experiments are challenging, which require almost identical coupling of multiple qubits to a single mode of the field. At the same time coupling constants can be varied over several orders of magnitude, which offers the possibility to perform and compare measurements in various distinct parameter regimes.

In this thesis I will present how the collective dynamics in a strongly coupled circuit QED system is explored to efficiently generate maximally entangled multi-particle states. Thereby we explicitly take advantage of the fact that the simultaneous interaction of multiple two-level systems with a single mode of the field leads to a significant enhancement of the interaction.

The strong coupling allows for a coherent exchange of excitations between two-level systems and the microwave field. For weak coupling in contrast, the resonator simply acts as a controlled dissipation channel. As a consequence any radiation that is emitted during collective dissipative processes may be guided efficiently to a detection system, where it can be fully characterized. Moreover experiments strongly benefit from the ability to observe and compare collective decay dynamics for different, well-defined initial states. Therefore superradiance, an effect mostly studied in large atomic ensembles, has been studied in this thesis from a new and unforeseen quantum mechanical point of view.

The results presented in this thesis indicate a promising path for future investigations, where coherent and furthermore dissipative photon-atom interactions may shed light on the essential concepts of quantum mechanics and where collective dynamics may work as a key resource for practical applications in the field of quantum information technology.

Zusammenfassung

Die Kopplung von supraleitenden Qubits mit koplanaren Mikrowellenresonatoren hat sich als erkenntnisreiches System für die Untersuchung der elementaren Wechselwirkungsbeziehungen zwischen Licht und Materie gezeigt.

Ein grosser Vorteil dieser speziellen physikalischen Implementierung ist, dass viele Kerngrössen, die die Wechselwirkung bestimmen, im Vorfeld geplant und unter kontrollierten Bedingungen fabriziert werden können. Insbesondere, die hohe Präzession, mit der die Kopplungskonstanten realisiert werden können, erlaubt die Beobachtung von kollektiven Effekten, wie sie in vergleichbaren Systemen nur schwer realisierbar sind. Davon sind insbesondere solche Experimente betroffen, bei denen nahezu identische Kopplung mehrerer Qubits an eine einzelne Feldmode verlangt wird. Gleichzeitig erlaubt die Tatsache, dass die Kopplungskonstanten über viele Grössenordnungen variiert werden können, kollektive Dynamiken in unterschiedlichen Parameterkonfigurationen zu messen und miteinander zu vergleichen.

In dieser Arbeit werde ich aufzeigen, wie die kollektive resonante Dynamik in einem stark gekoppelten supraleitenden Schaltkreissystem genutzt werden kann um effizient maximal verschränkte Vielteilchenzustände zu generieren. Dabei ist entscheidend, dass eine gleichzeitige Wechselwirkung mehrerer Zwei-Niveau-Systeme mit derselben Feldmode, mit einer signifikanten und nachweisbaren Beschleunigung der Wechselwirkung einhergeht.

Während eine starke Kopplung den kohärenten Austausch von Anregung zwischen dem Zwei-Niveau-System und dem Mikrowellenfeld erlaubt, stellt der Resonator bei schwacher Kopplung einen kontrollierten Zerfallskanal dar. Dadurch ist es möglich, die während der kollektiven dissipativen Dynamik entstehende Strahlung praktisch verlustfrei an Detektoren weiterzuleiten und umfassend zu charakterisieren. Bei unseren Experimenten haben wir dabei speziell von der Möglichkeit gebraucht gemacht, Zerfälle für verschiedene, wohl-definierte Ausgangszustände, miteinander zu vergleichen. Dies hat dazu geführt, dass der bisher hauptsächlich in grossen atomaren Ensembles beobachtete Effekt der Superstrahlung unter bisher ungeahnten quantenmechanischen Gesichtspunkten studiert und bewertet werden konnte.

Die in dieser Arbeit beschriebenen Resultate weisen einen vielversprechenden Weg für zukünftige Projekte auf, bei der sowohl eine kohärente als auch eine dissipative Licht-Atom Wechselwirkung wesentliche quantenmechanis-

che Konzepte in Erscheinung treten lässt und bei denen die involvierten kollektiven dynamischen Prozesse im Zuge der Quanteninformationsverarbeitung gezielt zur Anwendung kommen könnten.

Contents

1

Introduction

Since its development, starting around the beginning of the 20th century, the theory of quantum electrodynamics has celebrated a remarkable story of success. It's key statements are recovered from the insight that light and matter are constituted of elementary, inseparable entities, namely quanta. However, evidence for a quantization of the electromagnetic field were first obtained independently of the discretization that was applied to the atomic model by a quantization of its energy states. The classical description of electromagnetic fields is governed by the Maxwell equations, which are simple and elegant. Nevertheless they were doomed to fail when it came to the description of certain effects, such as the black-body radiation. Its adequate explanation was achieved by Planck's quantum hypothesis (1900), which together with Einstein's description of the photoelectric effect (1905) was one of the early models that were based on a quantized field with the photon being its elementary particle. The key success of quantum mechanics, in the sense of a quantization of atomic energy states (Bohr 1913, de Broglie 1924, Schrödinger 1926) lay in explaining the spectral emission lines of simple elements such as Hydrogen and explaining only empirical justified predictions as for example Rydberg's formula. A more rigorous treatment of both quantum mechanics and the quantization of electromagnetic fields was then accomplished by the work of Born, Heisenberg, Jordan (all in 1925) and finally Dirac (1927), by describing the field as an ensemble of harmonic oscillators and including interactions with a single charged particle such as an electron in an atom. His effort of also respecting the

invariance principles of special relativity was further pursued by Richard Feynman, Freeman Dyson, Julian Schwinger and Din-Itiro, finally giving quantum electrodynamics its modern face [Schwinger58].

In retrospective this development has led to the situation, that today's scientists are equipped with one of the most stringently tested theories allowing for highly precise predictions of experimental results. One of the main concepts that constitute the difference between a classical and quantum description of nature are state superposition and entanglement. The first includes the fact that the outcome of measurements can only be described statistically. The statistical character of measurement outcomes becomes even more relevant when two conjugate variables are to be determined out of multiple instances of the same experiment. In such a situation the Heisenberg inequality asserts a fundamental limit about the information that can be obtained over the system. Entanglement furthermore implies that multiple particles cannot be described independently as their quantum states may be highly correlated. It was shown by Bell (1964), and later proven experimentally by Aspet (1982), that the concept of entanglement required physicists to abandon the concept of locality. Due to its striking and nonintuitive properties, quantum mechanics has also raised a lot of discussion. Because of dealing with the fundamental feasibility and limitations of experimental observations, quantum theory has always been subject to an intense philosophical debate. It was therefore the declared goal of experimental scientist to resolve all confusion performing tests in the laboratory to only leave to philosophy what overreaches the mathematical framework. Obtaining control over the elementary particles that constitute light and matter, i.e. atoms and photons, therefore was a ground-breaking advance, as also reflected by the nobel prize in physics being awarded to Haroche and Wineland (2012) for their development of pioneering methods pursuing this goal. The application of various experimental optical techniques to single quantum systems has given rise to a research field known as quantum optics and in particular cavity QED. Those experiments involve a high level of technical intricacy and comprise a high number of practical challenges. However their complexity can be broken down to the simple mutual interaction of a two-level system with a harmonic oscillator. Two-level systems generally offer the possibility to store digital information, by either being in the ground $|0\rangle$ or the excited state $|1\rangle$. The similarity to classical bits, combined with the possibility of being in a quantum

superposition between those two distinct states, led to the fact that the two-level system is often refereed to as quantum bit or qubit. Up to today a variety of qubit systems have been identified as suitable testbeds for the fundamental aspects of quantum electrodynamics. Next to Rydberg atoms [Saffman10, Haroche13] and ions [Häffner08, Duan10, Monroe13] this includes quantum dots [Hanson07, Awschalom13], photonic systems [Kok07], nuclear spins [Vandersypen04], electron spins in diamond [Bernien13] and superconducting circuits [Clarke08, Devoret13], a system, in which superconducting qubits are coupled to on chip-transmission line resonators. The fascination of the latter mentioned field awakes from the macroscopic dimensions of superconducting qubits, even visible by bare eyes. This remarkable property hints at the possibility that there is no principle limit for the size of quantum objects, which will act according to the laws of quantum mechanics as long as they are well isolated from their environment. Furthermore another reason why circuit QED has made tremendous progress in the last ten years is because experiments can be simply designed and prepared using standard nano-fabrication methods. This makes the system not only interesting for fundamental research in quantum optics, but also for scalable solid state quantum information processing. The atom like-behavior combined with the fact of being manmade devices is why superconducting qubits also became known as "artificial atoms." One of the main advantages of this system is the outstanding control over the number of coupled two-level systems and furthermore over their individual coupling rates with respect to the resonator's field mode. Depending on the design, coupling rates can be varied over several order of magnitudes, which allows to enter various regimes, such as the strong or bad cavity limit of circuit QED. At the same time the spread in coupling rates for multiple qubit's is low enough such that they might be considered equal, which finally makes the circuit QED architecture an ideal toolbox for the investigation of collective resonant effects.

<div style="text-align: right; font-size: 3em;">*2*</div>

Concepts of circuit quantum electrodynamics

2.1 Superconducting transmon qubits

The basic idea of superconducting qubits can be understood by imagining them to be built up out of the most basic components that can be found in any electronic circuit. By taking a capacitor C and placing it in parallel width an inductor L we end up with a simple parallel LC resonator. By carefully choosing C and L and exposing the resonator to a sufficiently low temperature T we may expect this circuit to behave quantum mechanically. Nevertheless due to its harmonicity the energy of adding a quanta is independent of the number of quanta already present in the system. To make the resonator act as a qubit, it is therefore required to add some nonlinearity. This nonlinearity can be introduced by a Josephson junction. This junction is a barrier between two superconductors through which electrons, bound into Cooper pairs, can tunnel coherently [Clarke06]. All Cooper pairs inside a superconductor are condensed into a macroscopic state described by a single wavefunction. This gives rise to the two relevant quantum mechanical variables for the Josephson junction, which are the phase difference between the wavefunctions for each of the two superconducting electrodes $\hat{\varphi}$ and the difference of Cooper pairs $\hat{n}$ across the junction. The phase and the number difference can be associated with the Josephson coupling energy E_J respectively the charging energy E_c. Today a large variety of different superconducting electronic circuits, involving flux-, phase- and charge qubits are explored experimentally [Clarke08]. The latter one is also known as a
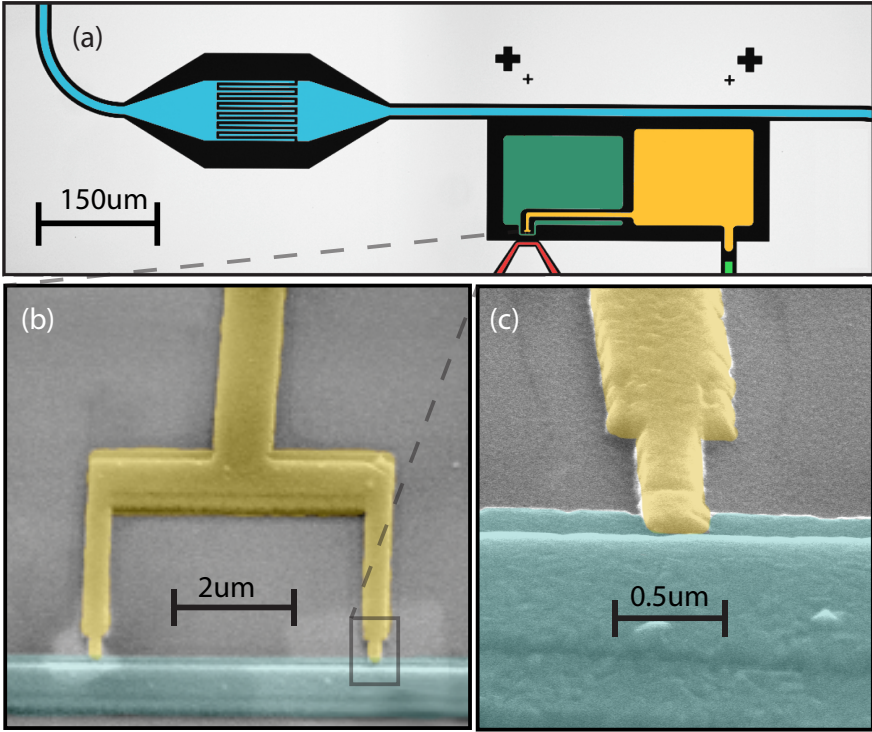
Figure 2.1: (a) False color microscope image of a superconducting qubit (orange) coupled to resonator (blue). (b) SEM image of the SQUID loop consisting of two parallel junctions. (c) SEM-image of a single junction.

Cooper pair box (CPB) and is of special interest for the work presented in this thesis. A micrograph of such a device, here coupled to a resonator, is shown in figure 2.1(a). In the heart of the device is a superconducting island connected via a Josephson junction to a reservoir. Physically the Josephson tunnel junction is fabricated from two superconducting layers, typically Aluminum, which are separated by a very thin (only a few nm thick) insulating oxide layer as shown in figures 2.1(c) and 2.2(a).

The Hamiltonian of the CPB is given by [Devoret97]

$$H_{qb} = 4E_C(\hat{n} - n_g)^2 - E_J \cos \hat{\varphi}. \tag{2.1}$$
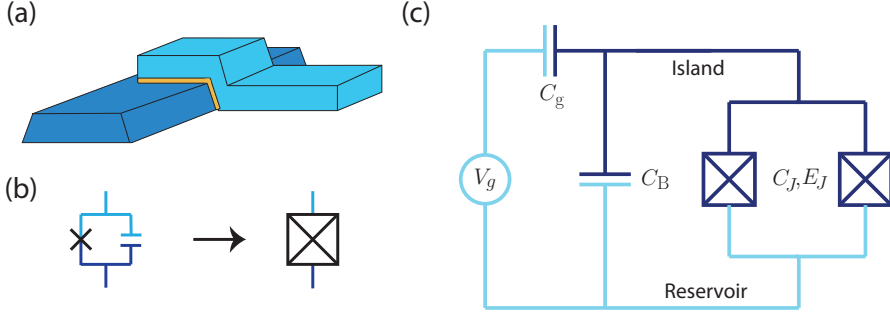
Figure 2.2: (a) Schematic image of a Josephson tunnel junction. Island (dark blue) and reservoir (light blue) are connected by a single oxide layer (orange). (b) The electronic circuit symbol for the Josephson junction before further simplification is represented by a capacitance in parallel with a nonlinear inductance. (c) Effective circuit diagram of a transmon qubit with a SQUID loop.

It describes the effective circuit shown in figure 2.2(c). The first term can be associated with the excess charges on the island and the second term is the Josephson energy, i.e. the energy that is associated with the tunneling of a Cooper pair across the junction. It can be understood as a measure for the overlap of the Cooper pair wavefunctions of the two electrodes. $\hat{n} = -\hat{q}/(2e)$ denotes the number of Cooper pairs transferred between the islands and $\hat{\phi}$ is the gauge-invariant phase difference between the superconductors. $n_g = Q_r/2e + C_g V_g/2e$ is the offset charge, where Q_r is some environment induced charge and $C_g V_g$ is the induced charge due to the voltage applied using an external source. Both $\hat{n}$ and $\hat{n}_g$ are expressed in units of $2e$. The charging energy is given by

$$E_C = \frac{e^2}{2C_\Sigma} \tag{2.2}$$

and represents the energy needed in order to put an additional electron on the island. $C_\Sigma = C_J + C_B + C_g$ is the total capacitance between island and reservoir. The Hamiltonian can either be solved analytically in the phase basis using Mathieu functions or by diagonalization when it is written in a
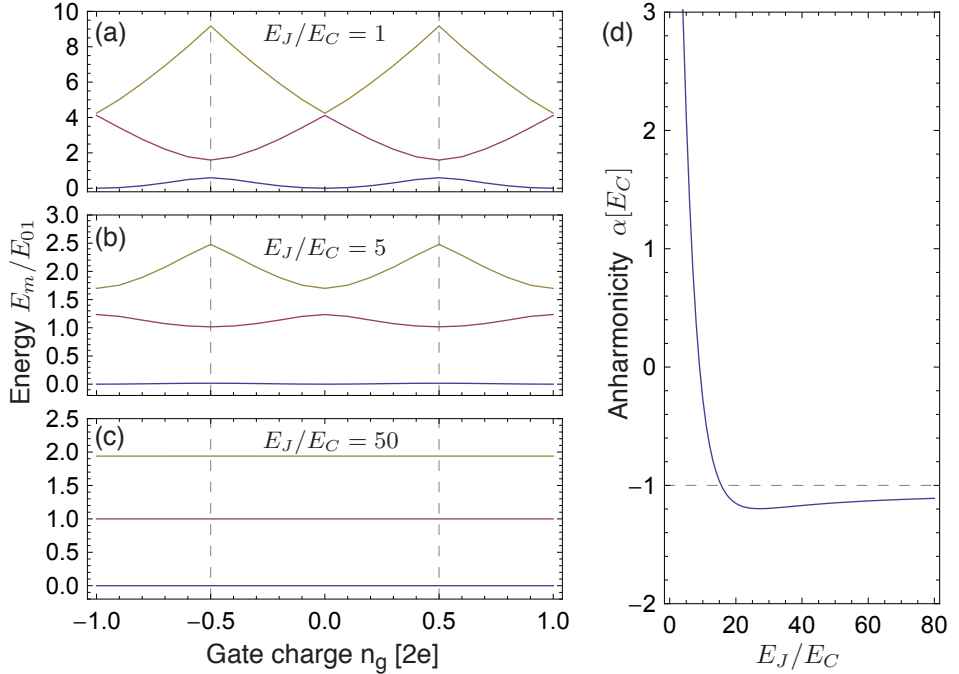
Figure 2.3: (a-c) Eigenenergies E_m (m=0,1,2,3) of the qubit Hamiltonian as a function of the offset charge n_g for different ratios of E_J/E_C. The energies are given in units of the transition energy E_{01} at $n_g = 1/2$. (d) Anharmonicity in units of E_C as a function of E_J/E_C. (Image courtesy [Koch07, Steffen13a]).

truncated charge basis, i.e the basis of eigenstates $|n\rangle$ of the Cooper pair number operator $\hat{n}|n\rangle = n|n\rangle$ [Bouchiat98]. It then reads

$$H_{qb} = 4E_C \sum_n (n - n_g)^2 |n\rangle\langle n| - E_J \sum_n (|n\rangle\langle n+1| + |n+1\rangle\langle n|). \quad (2.3)$$

The concrete choice of the truncation depends on the ratio of E_J/E_C and on the specific eigenstates of interest. The major drawback of the CPB is the energy dependence on the gate charge, which in the presence of charge noise leads to dephasing and decay. The transmon (transmission line shunted plasma oscillation qubit) [Koch07] differs from the CPB by

a larger additional capacitance C_B between island and reservoir, resulting in a higher ratio of E_J/E_C. The basic idea of the transmon is that an increase of this ratio leads to an exponential suppression of charge noise, while the anharmonicity decreases with a weak power law only. The gate charge dependence for different ratios of E_J/E_C is illustrated in figure 2.3. In the limit $(E_J/E_C) \gg 1$ equation 2.1 can be treated by perturbation theory and leads to the following gate charge independent energy of the transmon state m:

$$E_m \approx -E_J + \sqrt{8E_C E_J}\left(m + \frac{1}{2}\right) - \frac{E_C}{12}(6m^2 + 6m + 3). \qquad (2.4)$$

The ground to excited state transition energy is then given by

$$E_{01} = E_1 - E_0 \approx (\sqrt{8E_J E_C} - E_C) \qquad (2.5)$$

and the anharmonicity $\alpha \equiv E_{ef} - E_{ge} \approx -1.2\ E_C$ (see figure 2.3(d)). The residual sensitivity of a transmon qubit to charge noise can be quantified by the charge dispersion $\epsilon_m \equiv E_m(n_g = 1/2) - E_m(n_g = 0)$, which is given by

$$\epsilon_m \approx (-1)^m E_C \frac{2^{4m+5}}{m!} \sqrt{\frac{2}{\pi}} \left(\frac{E_J}{2E_C}\right)^{\frac{m}{2}+\frac{3}{4}} e^{-\sqrt{8E_J/E_C}} \qquad (2.6)$$

As can be seen from this equation the charge dispersion is exponentially decreasing with $\sqrt{E_J/E_C}$. Note that even though the transmon is almost insensitive to DC-electric fields it still couples to AC electric fields resonant to transitions frequencies of the transmon. The choice of E_J/E_C is a trade-off between a low charge dispersion and a sufficiently high anharmonicity to enable fast manipulations of individual transitions. The Josephson energy of a single junction depends on its geometry and material properties. If the junction is split into two spatially separated junctions forming a superconducting loop (see figure 2.1), the total Josephson energy becomes flux dependent and can by tuned by applying an external magnetic field inducing a magnetic flux ϕ to the loop, such that

$$E_J(\phi) = E_{J_{max}} \left|\cos\left(\frac{\pi\phi}{\phi_0}\right)\right|, \qquad (2.7)$$

2.2 Coplanar waveguide resonators

2.2.1 General description of transmission line resonators

Coplanar waveguide resonators (CPWR) are based on a geometry that resembles a coaxial line with the ground in the same plane as the center conductor (see figure 2.4(a), which then is capacitively coupled to input and output lines either via a simple gap or a interdigitated capacitor. The main advantages of a CPW construction is the avoidance of uncontrolled stray inductances and capacitances even for frequencies up to 10 GHz and beyond. The small lateral dimensions and the 1D-architecture ensure a very small mode volume and thus a very strong coupling to any dipoles exposed to the electric field. Moreover the impedance is mostly defined by the geometry and the dielectric constant of the substrate. As can be shown a coplanar waveguide resonator can be mapped to a simple harmonic oscillator, which then can be described quantum mechanically.

The nominal frequency is determined by the CPWR's effective length on the chip and the phase velocity v_{ph}. The resonance condition for the fundamental standing wave harmonic mode reads

$$\lambda_0 = v_{ph}/\nu_0 = 2l \qquad \text{with} \qquad v_{ph} = 1/\sqrt{L_l C_l} = c/\sqrt{\epsilon_{eff}}. \qquad (2.8)$$

$\epsilon_{eff} \sim 6.1$ is the effective permittivity of the CPW [Pozar11, Simons01]. C_l and L_l are the capacitance and inductance per unit length. All three values depend on the substrate material and the dimensions as denoted in figure 2.4b and can either be obtained analytically using conformal mapping techniques [Simons01], or more accurately from experimental data as well as from finite element electrostatic simulations. By using the first technique the capacitance per unit length C_l results in [Simons01]

$$C_l = 4\epsilon_0 \epsilon_{eff} \frac{K(k_0)}{K(k_0')}. \qquad (2.9)$$

K is the complete elliptic integral with modulus $k_0 = \frac{W}{W+2S}$ and $k_0' = \sqrt{1 - k_0^2}$.

The characteristic impedance of the CPW is given by $Z_0 = \sqrt{\frac{L_l}{C_l}}$ and typically chosen to be $50\,\Omega$. The CPWR can be represented by the model in figure 2.5. Though many of its useful properties strongly rely on its
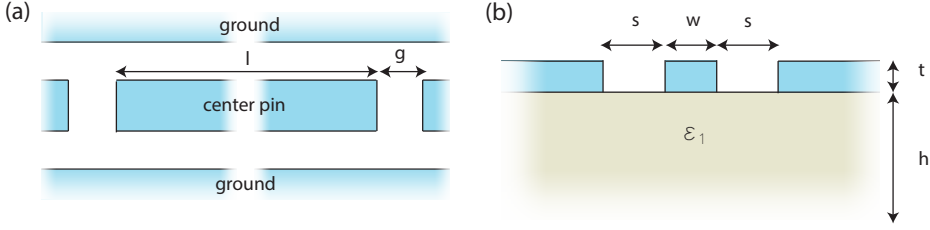
Figure 2.4: Coplanar waveguide resonator geometry. (a) Top view of a CPW resonator of length l with a gap capacitor of size g. (b) Cross section of a CPW resonator. The center conductor has a width w and is spaced by two gaps of width s to the ground plane. The metallization is typically etched Nb of thickness $t \sim 200\,\text{nm}$ patterned via standard single layer photo-lithography. The substrate is Sapphire with a thickness of $500\,\mu\text{m}$ and a relative permittivity of $\epsilon_1 \sim 11$.

distributed element character it is helpful to restrict the treatment to a single mode, which then can be represented by a lumped element circuit as shown in figure 2.5. This model qualifies for a later quantization of the circuit and also simplifies the calculation of important properties such as the Q-factor and the resonance frequency. Moreover it is very useful to gain a qualitative understanding of parasitic effects.

Mapping the distributed element model to a lumped element model (neglecting material losses) results in the following relations [Göppl09]:

$$C = \frac{C_l l}{2} \tag{2.10}$$

$$L_n = \frac{2L_l l}{n^2 \pi^2} \tag{2.11}$$

where n is the mode number and l is the length of the resonator. The resonance frequency of a simple lumped element LC-oscillator is given by $\omega_0 = \frac{1}{\sqrt{L_n C}}$. Using the expressions for Z_0, C, L_n and ω_0 we can express C

and L_n as a function of Z_0 and ω_0 by

$$C = \frac{\pi}{2Z_0\omega_0} \tag{2.12}$$

$$L_n = \frac{2Z_0}{n^2\pi\omega_0}. \tag{2.13}$$

$\omega_0 = 2\pi\nu_0$ is the nominal frequency of the fundamental mode ($n = 1$). Once the LC circuit is embedded between two coupling capacitances its nominal frequency is shifted due to the capacitive loading of C_i and C_o of the input and output line. This shift is given by

$$\nu_r = \frac{\nu_n}{\sqrt{1 + \frac{C_i+C_o}{C}}} = \frac{1}{\sqrt{L_n(C + C_i + C_o)}}. \tag{2.14}$$

ν_r corresponds to the desired frequency and ν_n is the nominal frequency for a certain mode. C_i and C_o determine the desired external quality factor. Choosing $C_o \gg C_i$ allows to gain a factor of two in the signal on the strongly coupled resonator output port going to the detection line. The loaded Q is given by [Göppl09, Pozar11]

$$\frac{1}{Q_L} = \frac{1}{Q_{int}} + \frac{1}{Q_{ext}}. \tag{2.15}$$

Here the internal quality factor Q_{int} is in the order of 10^5 and most of our resonators are in the overcoupled regime ($Q_{ext} \ll Q_{int}$), where Q_L is governed by Q_{ext} and the loaded quality factor can be fully controlled by the choice of the coupling capacitances. If we further assume a perfect impedance match between the resonator and its feedlines, the quality factor is given by

$$Q = \frac{\left(4\pi^2\nu_0^2 n^2 Z_0^2 C_i^2 + 1\right)\left(4\pi^2\nu_0^2 n^2 Z_0^2 C_o^2 + 1\right)}{8\pi\nu_0^2 n Z_0^2 \left(C_i^2\left(8\pi^2\nu_0^2 n^2 Z_0^2 C_o^2 + 1\right) + C_o^2\right)}, \tag{2.16}$$

and in case of $C_o, C_i \ll C$ with C given by equation 2.12 we get

$$Q = \frac{\nu_r}{\delta\nu} = \frac{1}{8\nu_0^2 n^2 \pi Z_0^2 (C_0^2 + C_i^2)}. \tag{2.17}$$

For example if we desire $\nu_r = 7\,\text{GHz}$ for $n=2$ (first harmonic), $\delta\nu = \kappa/2\pi = 100\,\text{MHz}$, an asymmetry $C_o = 10\,C_i$ and take an impedance of
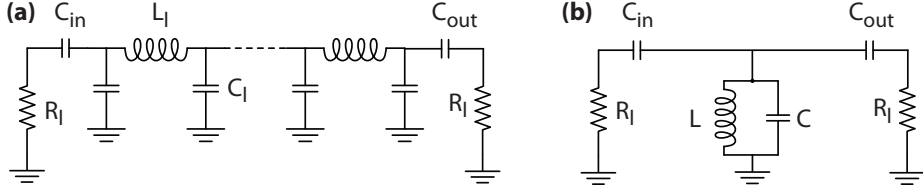
Figure 2.5: (a) Distributed element representation of an asymmetrically coupled transmission line resonator. The input/output ports are coupled via C_{in}/C_{out}. The impedance of the input and output line is R_L and the capacitance and inductance per unit length are C_l and L_l. (b) Parallel LCR oscillator representation of the transmission line resonator. A single mode can be modeled with an effective capacitance C and inductance L.

$50\,\Omega$, we can use the system of equations 2.12, 2.14, 2.17 to solve for capacitances $C_o = 10\,C_i = 92.5\,\text{fF}$ and a nominal frequency of $\nu_{n=2} = 7.25\,\text{GHz}$, which according to equations 2.12 and 2.13 corresponds to $L_{n=2} = 0.35\,\text{nH}$ and $C = 1.38\,\text{pF}$. Using equation 2.8 this results in an effective length of about $16.7\,\text{mm}$. The transmitted amplitude is given by the transmission coefficient S_{21} and can either be obtained from calculations of the transmission ABCD matrix [Göppl09] or be derived by input output formalism [Eichler13]. Around the resonance frequency the transmission coefficient $|S_{21}|^2$ can be approximated by a Lorentzian line shape

$$T_{Lor}(\nu) = T_0 \, \frac{\delta\nu^2}{\frac{\delta\nu^2}{4} + (\nu - \nu_r)^2} \tag{2.18}$$

where

$$T_0 = 4 \left(\frac{2C_i C_o}{C_i^2 + C_o^2} \right)^2 . \tag{2.19}$$

Once the obtained *LC* oscillator is described quantum mechanically its energy is given by diagonalization of the Hamiltonian

$$\hat{H} = \hbar\omega_0 (\frac{1}{2} + \hat{a}^\dagger \hat{a}) \tag{2.20}$$

with $\omega_0 = 2\pi f_0$ the angular resonance frequency, $\hat{a}$ and $\hat{a}^\dagger$ the usual ladder operators of a quantum harmonic oscillator.

13

2.2.2 Finite element simulations

Given the capacitance values of the input and output ports of the resonator we are able to calculate its expected Q-factor. However the question remains, how a desired capacitance relates to a specific design of our used multi-finger capacitors. This problem can be resolved by modeling the capacitor in a finite element electrostatic solver like *Ansoft Maxwell*. A model for a 2x14 finger output-capacitor C_o is shown in figure 2.6 (a). The same can be done for the input capacitance C_i, though it can be normally neglected because we chose $C_o \gg C_i$. Taking these values together with the analytically calculated values *L* and *C* of our analogue circuit, we are able to predict the resonator's linewidth. This can be done either by using equation 2.17 or by simulating the circuit 2.5(b) in a commercial microwave modeling software such as *AWR Microwave Office*. The simulated response is shown in figure 2.6(b). Fitting to a Lorentzian curve results in a width of 90.9 MHz, which is consistent with the fact, that this finger-capacitor was designed for a resonator with $\kappa/2\pi$=100 MHz.

However the capacitance calculated with *Ansoft Maxwell* only gives the DC-value of our design. It is therefore advantageous to compare this number to one obtained by electrodynamic finite element solvers such as *SONNET*. This software is able to calculate the scattering S-matrix in dependence on frequency. In fact any N-port network can be complectly described by a scattering S-matrix. Next to finite element simulations of specific geometries this matrix can also be obtained experimentally by vector network analyzer measurements. The scattering S-matrix can easily be converted one-to-one into equivalent matrices like the ABCD-matrix, the impedance Z-matrix or the admittance Y-matrix [Pozar93]. Though each of this matrices provides a complete description, the specified circuit or element is considered as a "black box" (see figure 2.7(a)). Therefore, to attribute some meaningful physical attributes to the network it is useful to translate these matrices into an equivalent circuit containing a few idealized components (see figure 2.7(b)). For a two-port reciprocal network the most complex equivalent circuit in the π-configuration can be obtained from the Y-matrix as shown in figure 2.7(b). It consists of three *LCR*-elements between N1-GND, N2-GND and N1-N2, where the latter is the most relevant for our simulations. Once the admittance of a single *LCR*-subcircuit is

(a)

(b)
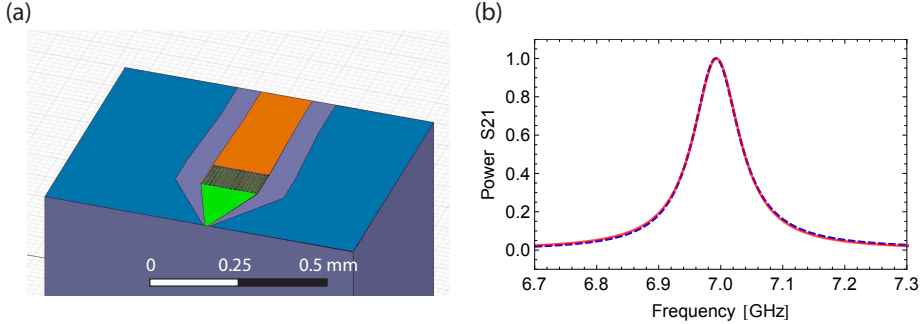
Figure 2.6: (a) 2x14-finger capacitor as modeled in *ANSOFT Maxwell*. The substrate is Sapphire and the metallization is assumed to be lossless. The calculation gives a value of 143 fF. (b) Linewidth calculation using *AWR Microwave Office*.

known the specific parameters of the idealized elements are related by

$$Y_{LCR} = i\omega C + \frac{1}{R_1} + \frac{R_2}{\omega^2 L^2 + R_2^2} - \frac{i\omega L}{\omega^2 L^2 + R_2^2}. \qquad (2.21)$$

Given the complex admittance matrix Y for two closely separated frequencies the values of all four components are fully determined.

If the number of fingers of the coupling capacitors is large it is expected that it shows additionally an inductive behavior at GHz frequencies and its effective capacitance derivates from DC-calculations. Our calculated S-matrix response is mapped to a Y-matrix, which then is mapped to the π-equivalent circuit. For DC and low-frequency it is expected that the device acts as if solely consisting of the capacitive elements as marked in green. As frequencies increase it is necessary to introduce a single inductive element between node 1 and 2. For even higher frequencies we also have to introduce inductances to ground. We have calculated the capacitance between node 1 and 2 up to 12 GHz for a 2x14-finger device as required for low Q-resonators. Figure 2.7(c) shows how the values relate to the DC-performance. The effective capacitance is increasing with higher frequencies, which effectively result in a lower Q of the resonator. It can be seen that even for frequencies of about 7 GHz a correction of about 20 % needs to be taken into account with respect to the static response of the device. The calculated DC-value

15
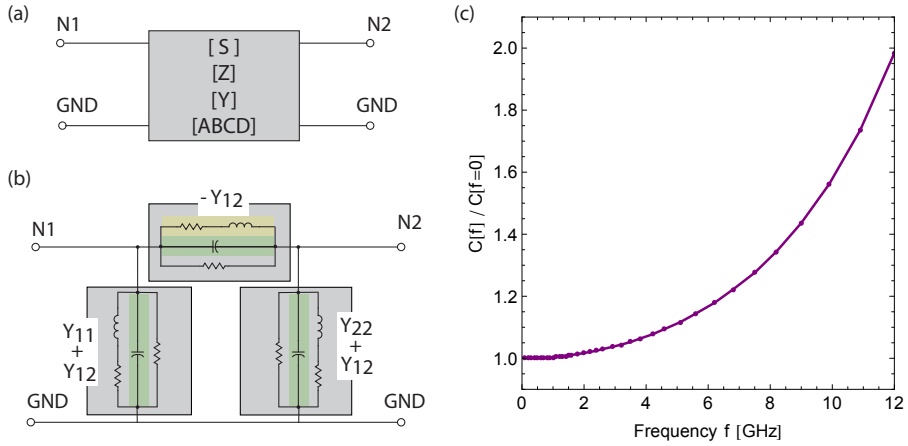
Figure 2.7: (a) General matrix-representations for a two-port reciprocal network. (b) Equivalent circuit in the π-configuration. The overall Y-matrix can be decomposed into Y-matrices for the three different LCR subcircuits. (c) Effective capacitance $C(\nu)$ as obtained from simulations by *SONNET* for a 2x14-finger capacitor.

of 135 fF is comparable to the one obtained by *Maxwell* namely 143 fF. The discrepancy might be due to a different geometry of the boundary box and the fact that *Maxwell* does not take into account the anisotropy of sapphire. Moreover both results still contain numerical errors.

2.3 The coupling of a qubit to a resonator

2.3.1 Jaynes Cummings model in circuit QED

The energy of the transmon qubit is related to the share of the voltage drop across its junction. This voltage might as well be provided by the strong electric field of the transmission line resonator. In fact the two-dimensional architecture leads to a very strong spacial confinement of the field mode and the resulting small mode volume gives rise to large coupling rates, which allow for a coherent exchange of energy, faster than the both subsystem's decoherence rates. It is discussed here how the coupled system is described

in the relevant circuit QED parameters and how a precise expression for the coupling rate g can be obtained. The transmon Hamiltonian (equation 2.1) can be written in the basis of its uncoupled eigenstates $|i\rangle$

$$H_{qb} = \hbar \sum_i \omega_i |i\rangle\langle i|, \tag{2.22}$$

with $\hbar\omega_i$ being the energy of state $|i\rangle$. The Hamiltonian of the combined system including the Hamiltonian of the resonator (equation 2.20) reads

$$H = \hbar \sum_i \omega_i |i\rangle\langle i| + \hbar\omega_r a^\dagger a + \hbar \sum_{i,j} g_{ij} |i\rangle\langle j|(a + a^\dagger), \tag{2.23}$$

where the zero point energy was omitted. The coupling energies are given by

$$\hbar g_{ij} = 2e\beta V_{rms}\langle i|n|j\rangle = \hbar g_{ji}^* \tag{2.24}$$

with $\hat{n}$ the Cooper pair number operator, $V_{rms} = \sqrt{\frac{\hbar\omega_r}{2C_r}}$, ω_0 the frequency of the fundamental mode ($n=1$). C_r is the resonator's effective capacitance (see equation 2.12), β is the splitting parameter and can be derived from the effective transmon network. If we use the approximation $E_J \ll E_C$, i.e. $\langle i|\hat{n}|j\rangle$ being dominated by nearest neighbor couplings, $j = i \pm 1$, and further take advantage of the rotating wave approximation (justified by the coupling energy being small compared to the qubit and resonator transition frequencies) equation 2.23 can be written in the eigenbasis of the transmon Hamiltonian and leads to the generalized Jaynes-Cummings Hamiltonian

$$H = \hbar \sum_i \omega_i |i\rangle\langle i| + \hbar\omega_r a^\dagger a + \left(\hbar \sum_i g_{i,i+1} |i\rangle\langle i+1|a^\dagger + h.c. \right). \tag{2.25}$$

The coupling then is given by

$$g_{i,i+1} \approx \frac{2e}{\hbar}\beta\sqrt{\frac{\hbar\omega_0 n}{2C_r}}\sqrt{\frac{i+1}{2}}\left(\frac{E_J}{8E_C}\right)^{1/4}. \tag{2.26}$$

If we restrict our system to two levels the generalized Jaynes Cummings Hamiltonian simplifies to the well known standard Jaynes-Cummings Hamiltonian

$$\hat{H} = \underbrace{\hbar\omega_r \hat{a}^\dagger \hat{a}}_{\hat{H}_r} + \underbrace{\frac{\hbar\omega_a}{2}\hat{\sigma}_z}_{\hat{H}_a} + \underbrace{\hbar g(\hat{a}^\dagger\hat{\sigma}_- + \hat{\sigma}_+\hat{a})}_{\hat{H}_{int}}, \tag{2.27}$$

consisting of the free field H_r, the atomic H_a and the interaction H_{int} terms. The coupling to mode n then is simply given by

$$g := g_{01} \approx \frac{2e}{\hbar}\beta\sqrt{\frac{\hbar\omega_0 n}{C_r}}\left(\frac{E_J}{8E_C}\right)^{1/4}. \tag{2.28}$$

From equation 2.26 we see that the coupling increases for higher mode numbers namely $g \approx \sqrt{n}$. In fact knowledge about E_J is not required for the calculation as it can be expressed by using the relation

$$n\omega_0 = (\sqrt{8E_J E_C} - E_C)/\hbar. \tag{2.29}$$

The fist experimental implementations of this Hamiltonian where achieved by demonstrating the strong coupling of a single photon to a cooper pair box [Wallraff04], the generation of single photons [Houck07] or the first realization of a cavity bus architecture enabling the exchange of information between two distinct qubits [Majer07].

The coupling of multiple two-level systems to a single mode is described by the Tavis-Cummings Hamiltonian [Tavis68]

$$\hat{\mathcal{H}}_{\mathrm{TC}} = \hbar\omega_{\mathrm{r}}\hat{a}^\dagger\hat{a} + \sum_j \left(\frac{\hbar}{2}\omega_j\hat{\sigma}_j^z + \hbar g_j(\hat{a}^\dagger\hat{\sigma}_j^- + \hat{\sigma}_j^+\hat{a})\right). \tag{2.30}$$

This Hamiltonian comprises the nonlinear scaling of the coupling constant with respect to the number of qubits, which is also discussed and experimentally studied in [Fink10a]. For most of the experiments presented in this thesis the transmon's third level $|3\rangle$ is not exploited for any of the preparations nor gates, still it is of relevance for some of the read-out and calibration techniques.

2.3.2 Effective transmon network

So far it is not yet discussed how the parameter β is obtained from the geometry of the qubit, which consists of four basic structures: the ground plane, the resonator, island and reservoir (see figure 2.8(a)). To resolve this issue it is required to find the relation between the real transmon network, shown in figure 2.8b, and the already introduced real capacitance network as shown in figure 2.8c. The parameter β is given by

$$\beta := \frac{C_g}{C_\Sigma} \tag{2.31}$$

where $C_\Sigma = C_g + C_B + C_J$. The effective C_Σ is the sum of four capacitances in parallel $C_{\Sigma,e} = C_g + C_B' + C_{23} + C_J$ with C_J being the capacitance of the Josephson junction and C_J the capacitance of the transmon's shunt capacitor. The sum $C_0 = C_g + C_B'$ is obtained by replacing C_{23} and C_J by a voltage source V and calculating the total capacitance C_0 with V_g being removed. Employing Kirchhoff's rules [Burkhard12] this results in the linear set of equations:

$$V = V_{24} + V_{34},$$
$$V = V_{12} + V_{13},$$
$$V = V_{12} + V_{14} + V_{34},$$
$$0 = -Q_{12} - Q_{14} + Q_{13},$$
$$0 = Q_{14} - Q_{24} + Q_{34}.$$

We solve this equations for $\{V, V_{12}, V_{13}, V_{24}, V_{34}\}$ and use that $Q_{ij} = V_{ij}C_{ij}$. The total charge is given by

$$Q = Q_{12} + Q_{24} = Q_{13} + Q_{34} = \frac{1}{2}(Q_{12} + Q_{24} + Q_{13} + Q_{34}).$$

We then use the fact that C_{14}, the capacitance between the millimeter-sized resonator and ground, is large compared to all other involved capacitances and we arrive at

$$C_0 = \frac{Q}{V} = \frac{(C_{12} + C_{24})(C_{13} + C_{34})}{C_{12} + C_{13} + C_{24} + C_{34}},$$

such that C_Σ is finally given by

$$C_\Sigma = \frac{(C_{12} + C_{24})(C_{13} + C_{34})}{C_{12} + C_{13} + C_{24} + C_{34}} + C_{23} + C_J. \tag{2.32}$$

and the splitting parameter $\beta = \frac{V_{23}}{V_g} = \frac{C_g}{C_\Sigma}$ comes down to [Burkhard12, Steffen13a]

$$\beta = \frac{C_{12}C_{34} - C_{13}C_{24}}{(C_{12} + C_{24})(C_{13} + C_{34}) + (C_{12} + C_{13} + C_{24} + C_{34})(C_{23} + C_J)}. \tag{2.33}$$

2.3.3 Limitations of T_1 due to capacitive gate line coupling

In practice the qubit and the resonator are mutually coupled as the qubit state depends on the resonator voltage and vice-versa. However the qubit might couple in a similar way to its charge gate line. Even if no intentional voltage is applied on this lines their vacuum noise does have significant influence on the qubit decoherence. It is possible to estimate a limit for the qubit relaxation time given a certain charge line design. We therefore perform a similar calculation as for the resonator coupling, but substitute the resonator voltage with the charge line voltage. According to Fermi's Golden Rule, the relaxation rate for small gate voltage fluctuations is then given by

$$\Gamma_1 = \frac{1}{\hbar^2} \left| \left\langle 0 \left| \frac{\partial H}{\partial V_g} \right| 1 \right\rangle \right|^2 S_V(\omega) \tag{2.34}$$

where

$$S_V(\omega) = 2\hbar\omega Z \tag{2.35}$$

is the voltage noise spectral density at the qubit transition frequency in the low temperature limit [Schoelkopf02, Clerk10]. Like that the final expression for the qubit relaxation is given by

$$\Gamma_1 = \frac{4\hbar\omega Z e^2}{\hbar^2} \sqrt{\frac{E_J}{2E_C}} \beta_{CL}^2 \tag{2.36}$$

where β_{CL} is the splitting parameter associated to the charge line. Another way of expressing this relation is

$$1/T_1 = \Gamma_1 = \frac{4g_{CL}^2}{\omega}. \tag{2.37}$$

Here, g_{CL} is now the coupling of the qubit to the charge line, calculated using equation 2.24 where V_{rms} was replaced by $2\hbar\omega^2 Z$. The obtained expression matches well to the expected expression for the decay into a one-dimensional transmission line [Astafiev10].

2.3.4 Design aspects of a low g sample

The coupling rates can be varied by simply adjusting the parameter β. It can be seen from equation 2.33 that the symmetry of the transmon design

plays an important role. In fact even if the transmon is placed close to the resonator on an antinode of its field, zero coupling can be obtained if island and reservoir have the same capacitance to both resonator and ground. If we want to design low g transmon qubits we thus use the symmetry of the design as our key knob to obtain a certain small coupling rate. Therefore we change the distance *c* indicated in figure 2.8a. All capacitances in equation 2.33 are calculated by finite element electrostatic simulations in *Ansoft Maxwell*. The resulting coupling *g* of the transmon qubit to the first harmonic mode of the cavity as a function of *c* is shown in figure 2.9a. Indeed the obtained coupling rates are orders of magnitude lower than the typical coupling rates of strong coupling circuit QED, which in contrast can be obtained by a preferably asymmetric transmon design. As discussed, another important characteristic of the transmon is the charging energy, which is dominated by the capacitance between island and reservoir. We can tune E_c by changing the geometric parameter *a* (see figure 2.8a) without significantly changing the symmetry and thus leaving *g* untouched. How specific settings of *a* result in the simulated value for E_c is shown in figure 2.9b. Last but not least we have to take into account the qubit coupling to the charge gate line. This value is aimed to be low in comparison to typical expected intrinsic relaxation rates but still needs to be large enough to allow short microwave pulses without dissipating too much microwave power into the cryogenic system. The gate line coupling can be changed by the geometric parameter *r* and the simulated results are shown in figure 2.9c.

2.4 Fabrication of superconducting devices

The fabrication of the circuit QED building blocks discussed in this chapter requires the ability to create micro- and nano-sized structures under clean conditions. Therefore the superconducting circuits used in our experiments are fabricated in the *FIRST* cleanroom facility for advanced micro- and nanotechnology at ETH Zurich. The large structures, such as the resonator and the qubit's dedicated gatelines, are fabricated using photolithography. For this purpose we use a commercially Nb sputtered 2-inch sapphire wafer coated with a thin layer of photosensitive resist, e.g. Polymethylmethacrylat (PMMA). It is aligned with an externally ordered mask and exposed with UV light. After development the niobium is etched using a reactive

ion etcher *RIE 76* from *Oxford Instruments.* A typical wafer comprises
up to 40 individual chips, which are separated using a dicing saw after a
special dicing protection has been spinned to protect the waver from small
sapphire debris. Both the initial photoresist and the protection layer are
removed using subsequent baths of Dimethylsulfoxid (DMSO), Aceton and
Isopropanol. Finally the chip is cleaned by an oxygen plasma. To fabricate
the qubits into their intended gap (see figure 2.1) electron beam lithogra-
phy is required as the resolution of our used UV photolithographic device
is insufficient to write structures such as the Josephson junction, which
are on the order of 100 nm. This technique uses electrons accelerated to
30 kV with a small enough de-Broglie wavelength, such that diffraction is
not the dominant limitation. Beam instability and insufficient collimation
limits the resolution to about 20 nm. The used resist is a bi-layer resist,
where the bottom layer is P(MMA-MAA) pure and the top layer PMMA
950k pure 2:1 in Ethyl lactate. After exposure the development is done
using Methylisobutylketon (MIBK) in Isopropanol (1:3). To expose the
junction and in parallel the large transmon shunt capacitor we use a dou-
ble angle shadow evaporation technique inside a *Plassys MEB 500*, which
is a thin film physical vapor deposition system using electron beam evap-
oration of metals. After the Aluminum is evaporated the lift-off is done
either using Aceton or N-Methyl-2-pyrrolidon (NMP). The chip is then
glued and mounted into a printed circuit board. The transmission lines
on the microchip and those on the PCB are connected via Aluminum wire
bonds, placed manually onto the sample using a *Westbond 747677E* wire-
bonder. A more detailed discussion of the fabrication methods applied to
the circuit QED samples used for our experiments can be found in [Stef-
fen13a, Fink10a].

2.5 The Lindblad master equation

A versatile theoretical tool, which was used extensively throughout the
work of this thesis, in particular to describe the dynamics and steady state
solutions of the coupled system, is the von-Neumann equation, which is the
quantum mechanical analogue to the Lioville equation in classical statistical
mechanics. It reads

$$\dot{\rho}(t) = -i[\mathcal{H}_0, \rho(t)] \tag{2.38}$$

and is used to describe the time evolution of the full quantum state of the system expressed by the density operator $\rho = \sum p_k \left| \Psi_k \right\rangle \left\langle \Psi_k \right|$, where p_k is the probability for measuring the pure state $\left| \Psi_k \right\rangle$ inside a mixture. Normalization requires $Tr(\rho) = 1$. Generally $Tr(\rho^2) \leq 1$, which only gives equality if ρ is describing a pure state. H_0 is the Hamilton operator of the system and in this thesis either represented by the Jaynes-Cummings or Tavis-Cummings Hamiltonian. The expectation value for the measurement of a general observable A is calculated by

$$\langle A \rangle = \mathrm{Tr}(\rho A) \tag{2.39}$$

A more precise description of the dissipative dynamics of the quantum mechanical system is provided by the Lindblad equation, which takes care of the decoherence processes that go along with the dynamics. The evolution is generally non-unitary and non-reversible because part of the information is lost. In fact the Lindblad equation, which is also often simply referred to as master equation, is the most general type of Markovian master equations and allows to both include the qubit's relaxation and its dephasing rates. It is written as

$$\dot{\rho}(t) = -\frac{i}{\hbar}[\mathcal{H}_0, \rho] \tag{2.40}$$

$$+ \frac{\kappa}{2}(2a\rho a^\dagger - a^\dagger a \rho - \rho a^\dagger a) \tag{2.41}$$

$$+ \sum_i^N \frac{\gamma_1}{2}(2\sigma_-^i \rho \sigma_+^i - \sigma_+^i \sigma_-^i \rho - \rho \sigma_+^i \sigma_-^i) \tag{2.42}$$

$$+ \frac{\gamma_\varphi}{2}(\sigma_z^i \rho \sigma_z^i - \rho) \tag{2.43}$$

for N qubits coupled to a single mode of the cavity. For a single qubit and under certain assumptions this equation can be solved analytically. Nevertheless for the calculation of the collective dynamics numerical methods were employed.
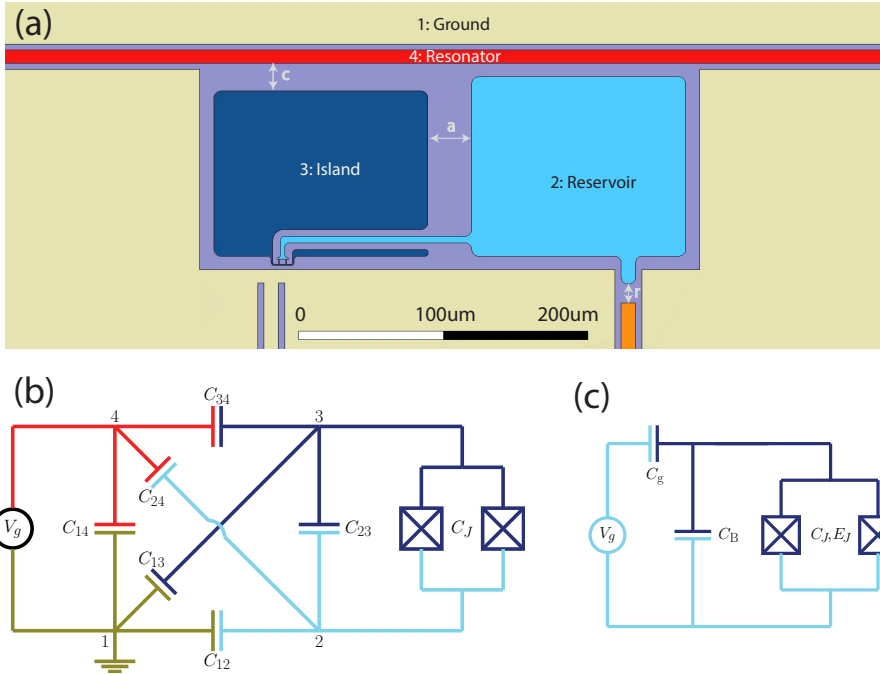
Figure 2.8: (a) Model of a transmon qubit coupled to a resonator as used for finite element electrostatic simulations in *Ansoft Maxwell*. The design aspects of this low g qubit are discussed in this chapter. (b) Full capacitance network of the transmon coupled to CPW resonator. (Image courtesy [Koch07])(c) Effective transmon network.
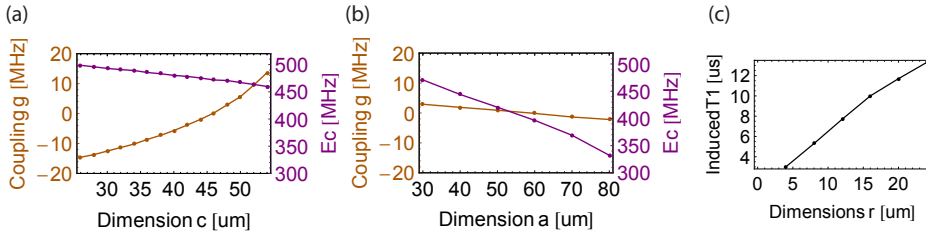
Figure 2.9: (a/b) Dependence of the coupling g and the charging energy E_C on the two dimensions c and a indicated in figure 2.8(a). (Note that the coupling constant gets negative once β in 2.33 takes a negative value.) (c) Charge line induced T1 as a function of the geometric dimension c.

3

Measurement setup and principles

The quantum mechanical properties of qubits can only be revealed if they are well isolated from their environment. However in order to carry out experiments some degree of environmental coupling needs to be introduced to the system if any information is to be extracted from it. A key challenge therefore is to maintain the ability for state preparation and read out and at the same time keep environmental influences such as high frequency noise, magnetic noise and electric noise at a minimum, which affect the coherence performance of the quantum system.

The energy of a single photon with a typical frequency of 7 GHz expressed in temperature is $T = h\nu/k_B = 335\,\text{mK}$. Allowing the qubit to be in the ground state requires the ambient temperature to be well below this limit. Dilution refrigerators are typically operated at a base temperature of about $20\,\text{mK}$, which would correspond to $p = 5 \cdot 10^{-8}$ of the total population being in the excited state.

As our experiments are performed at the single photon level, a very important aspect of the setup is the signal amplification. Even though most of the used microwave equipment can be purchased commercially, its application is more aimed on wireless transmission or radar applications, which involves signals in the mW range, orders of magnitude higher than what is dealt with in our experiments, typically about $10^{-18}\,\text{W}$.

In order to sample the microwave signal inside a GHz frequency range it is required to down convert it to a frequency range, which can be digitized. The same is true for the generation of microwave signals as for example used

for state preparation. The typical bandwidth of our arbitrary waveform generators is limited to $1\,$GHz, meaning that their signal needs to be up-converted. A basic aspect of the used microwave-engineering practices is analog and digital filtering of the signals to only the frequency range, which contains the information related to the experiment.

3.1 Cryogenic setup

3.1.1 Dilution refrigerator

The cryostat used for the presented experiments in this thesis is a *Triton200* dilution refrigerator from *Oxford Instruments*. Without any thermal load the base temperature of this system is specified to be $10\,$mK. The cryostat uses two different cooling techniques. The $4\,$K stage is cooled by a pulse tube cooler, which is based on a closed-loop refrigerant expansion cycle of pure helium ^{4}He. The compressed refrigerant is periodically pumped through two cold heads and thus removes part of the heat during each cycle. To achieve mK temperatures a second cooling mechanism is used, which is based on a mixture o ^{3}He$/^4$He. In the mixing chamber a ^{3}He-rich liquid helium phase floats on top of a ^{3}He-poor liquid helium phase. The endothermic process of ^{3}He evaporating from the concentrated phase through the phase boundary into the dilute phase consumes energy. This energy is thermally provided by the base plate, which as a consequence will cool down. A more detailed discussion of the working principles of cryostats can be found in [Pobell06, Enss05, White02]. The refrigerator consist of several different stages, which are operated at different temperatures, their name accordingly $50\,$K, $4\,$K, $900\,$mK (or Still plate), $100\,$mK, $20\,$mK (or base plate) (compare figure 3.1).

3.1.2 Aspects of cryogenic cabling

A typical circuit QED experiment requires microwave and DC cabling: Charge gate lines to manipulate the qubit state, flux gate lines for fast tuning of the qubit transition frequency, resonator input lines for the injection of coherent radiation, resonator output lines for signal detection and DC bias lines to apply static magnetic fields using miniature coils. Each refrigerator stage provides a certain cooling power, defined as energy that
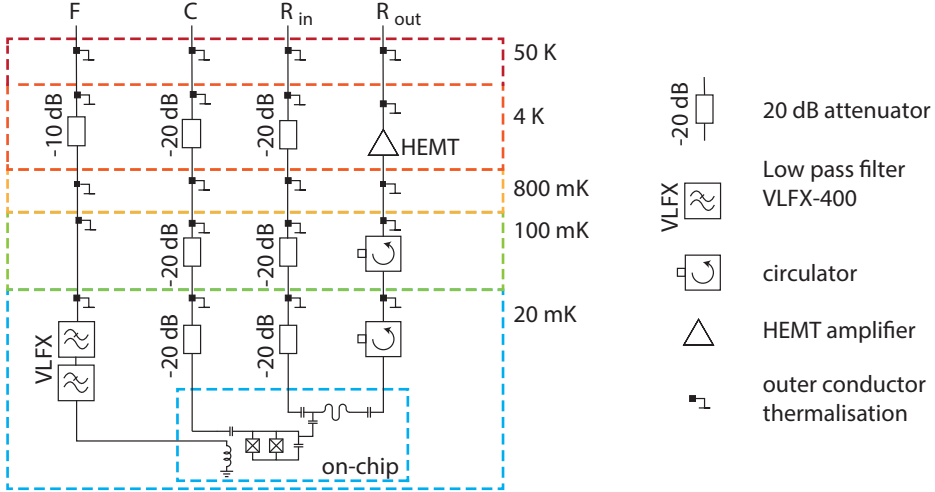
Figure 3.1: Schematic of the cryogenic microwave wiring: Resonator in- and output lines (R_{in}, R_{out}), qubit charge- (C) and flux- (F) bias line.

can be dissipated per unit time while maintaining a specific temperature. The 4K stage for example provides a cooling power of 300 mW and the base plate is specified with 200 μW at 100 mK. This puts essential constraints on the microwave and DC wiring of the fridge. A typical wiring diagram is shown in figure 3.1. Each cable wired from room temperature to base plate is causing a thermal load. For normal conducting metals there is strong relation between the electrical and thermal conductivity. The first is normally requested to be high whereas the second needs to be preferably low in cryogenic applications. The rate of heat flow per unit area resulting from a temperature gradient between a cable of cross section A and length L is given by

$$\dot{Q} = \frac{A}{L} \int_{T1}^{T2} \lambda(T) dT \tag{3.1}$$

where λ is the thermal conductivity of the material used for the cable, typically copper or stainless steel. Precise values can be found in [White02]. The electric damping is typically specified as attenuation per unit length, which at a frequency of 7 GHz for a *Microcoax TP45* copper cable is -1.7 dB/m and for a *Microcoax SSSS* stainless steal cable is -10.8 dB/m. To

keep the refrigerator in thermal equilibrium it is requested that the heat flows from a number of cables N arriving at a certain temperature stage is much smaller than the cooling power P_c, i.e. $\sum \dot{Q}_i \ll P_c$. The microwave cables wired into our fridge are semi-rigid, which means they are a coaxial form using a solid copper outer sheath. While the outer conductor of the cable is naturally thermalized at the temperature stage it is attached to, the inner conductor is preferably thermalized by using attenuators, which comes at the price of a lower transmittance. This issue becomes especially important for the resonator's output line and we therefore decided to use superconducting niobium-titanium cables [Pobell06].

Nevertheless even if the chip itself is sufficiently cold, the resonator (or the qubit) itself might still be thermally populated by thermal noise, that origins from higher temperature stages of the cryostat and propagates via the coupled gate lines. The noise power spectrum from a thermal noise at temperature T is equivalent to the 1D black body radiation spectrum and given by

$$S(\omega) = \frac{\hbar\omega}{\exp^{\frac{\hbar\omega}{k_B T}} - 1}. \tag{3.2}$$

The final noise at the end of the gate line is given by the sum of the thermal noise at each stage, attenuated by the attenuators between that temperature and the end of the line. For a good estimate we may neglect the heat gradient inside the cable and simply assume it to be of uniform temperature corresponding to the warmest attenuator it is attached to. This is a good assumption as the cable itself does not need to thermalize with the black body radiation it is carrying. This is true in particular, when the cables have low loss. The total noise spectral density at the end of a line, which has N attenuator attached to N temperature stages is then given by

$$S_{total}(\omega) = \sum_{i<j}^{N} A_i \cdot S_j(\omega), \tag{3.3}$$

with j=1 referring to the coldest temperature stage. This theoretical framework allows to predict the noise power that is seen by the qubit and the resonator. In the latter case the spectral density can be related to the expected mean number of thermal photons by

$$\bar{n} = \int T(\omega) S_{total}(\omega) d\omega \tag{3.4}$$

For a resonator input line as drawn in figure 3.1 the mean number of thermal photons due to the thermal radiation inside the cable is $\bar{n}$=0.0002 at 7 GHz. In addition the thermal conductivity of this specific cable introduces a heat load of $7.8 \ 10^{-8}$ W onto the base plate. Last but not least an appropriate wiring will take into account the thermal expansion of the cables that happens every time the cryogenic system is warmed up or cooled down. To reduce the stiffness of the cables it is advisable to introduce a number of small bends between every two positions the cable is attached at.

3.2 RF frequency data acquisition

The readout of quantum states and the observation of its dynamics requires the time resolved measurement of single photons within a frequency range of about 4-10 GHz. To get standard data acquisition techniques respond to such small signals requires to amplify the signal over 12 orders of magnitude. Once amplified the obtained signal is typically dominated by the thermal amplifier noise added by the amplification chain if no parametric amplifiers are used. To obtain sufficient signal to noise ratios the signal needs to be averaged over 10^5 - 10^7 instances of the same experiment such that any uncorrelated thermal noise is averaged out. The small bandwidth of the resonator allows to down-convert the high frequency signal ω_{RF} to an intermediate frequency of $\omega_{\mathrm{IF}}/2\pi$=25 MHz by using a down-conversion board as shown in figure 3.2, which is used to converts frequencies in the GHz range to typically 25 MHz. The main component of this board is an IQ-mixer. This device accomplishes a multiplication of the high frequency signal with a local oscillator frequency of $\omega_{\mathrm{IF}} = \omega_{\mathrm{RF}} - \omega_{\mathrm{LO}}$ leading to frequency components at the desired 25 MHz. Before the signal enters the mixer it is filtered and amplified by low noise amplifiers. After down-conversion the signal is once more amplified by +30 dBm and low-pass filtered with an anti-aliasing filter with a cut-off at 50 MHz. An analogue to digital converter then digitizes the signal with a sampling rate of 0.1 GS/s, which then is recorded by the attached field programmable gate array (FPGA) *Virtex 4*. In contrast to standard microprocessors used in home computers an FPGA allows for highly parallel processing and thus is perfectly suited for fast and real-time digital signal analysis. The complex amplitude $S(t) = I(t) + iQ(t)$ of the

31

(a)

(b)
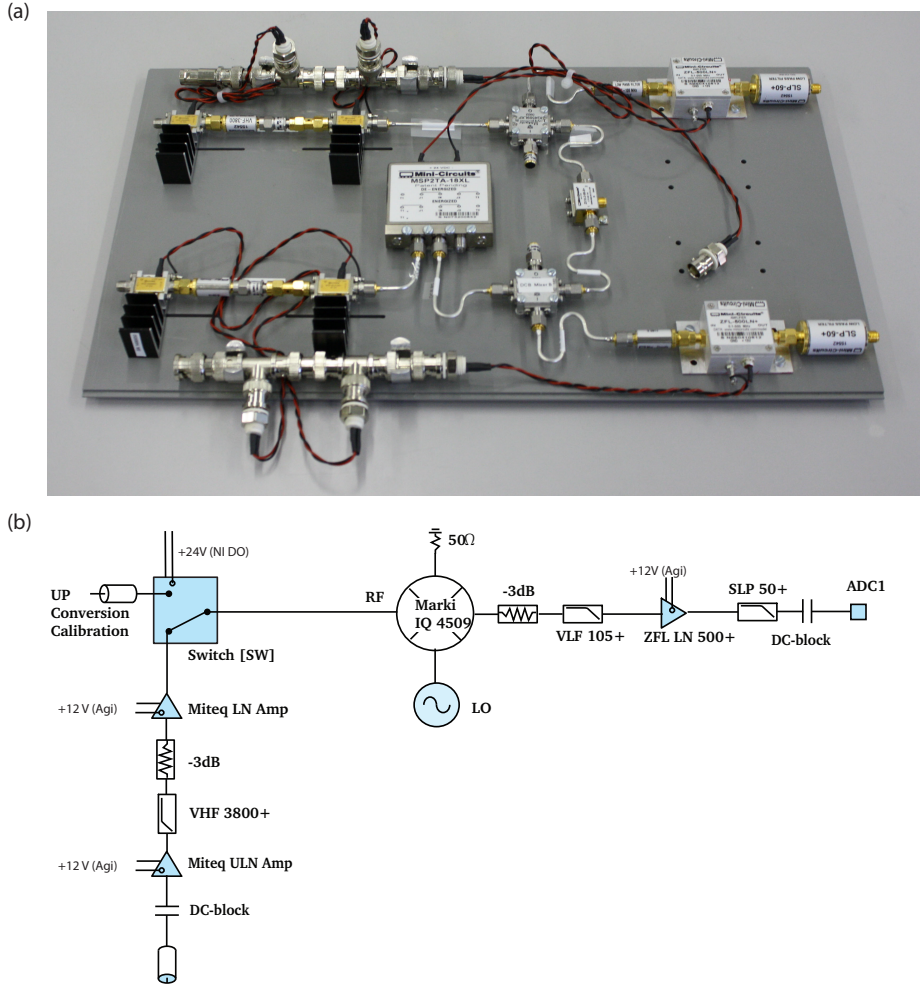
Figure 3.2: (a) Picture of the down-conversion board with two amplification and mixing lines. (b) Details of the microwave wiring and the used components for the lower of the two lines.

itinerant microwave radiation is obtained by digital down-conversion of the signal to DC by multiplying the detected signal $A(t)\cos(\omega_{\text{IF}} + \phi(t))$ with a sine and a cosine

$$I(t) = A(t)\cos(\omega_{\text{IF}} + \phi(t))\cos(\omega_{\text{IF}}t) \qquad (3.5)$$

$$I(t) = A(t)\cos(\omega_{\text{IF}} + \phi(t))\sin(\omega_{\text{IF}}t). \qquad (3.6)$$

This converts the signal from ω_{IF} to DC and $2\omega_{\text{IF}}$. As we are only interested in the DC component the upper sideband can be removed with a digital low pass filter with any bandwidth smaller than ω_{IF}.

3.3 State readout

3.3.1 Read out in the dispersive limit

If a detuned qubit is coupled to a cavity, its bare frequency is shifted depending on whether the qubit is in its ground or excited state. This dispersive shift can be understood in the dispersive limit of the Jaynes-Cummings Hamiltonian. It provides versatile tool to read out quantum states of single or multiple qubits. If the qubit is far detuned from the resonator, that is $|\Delta| = |\omega_q - \omega_r| \gg g$, the qubit and the resonator do not exchange energy. Nevertheless they still influence each other by photon mediated virtual interactions, leading to a rescaling of their bare energies. The Jaynes-Cummings Hamiltonian (equation 2.27) can be approximated using time dependent perturbation theory by expansion into powers of g/Δ. This yields [Haroche92, Gerry05]

$$H \approx \hbar(\omega_r + \chi\sigma_z)(a^\dagger a + \frac{1}{2}) + \frac{\hbar\omega_a}{2}\sigma_z \qquad (3.7)$$

The induced level shift χ for a two level system is given by g^2/Δ. However the multi-level structure of the transmon in combination with its large coupling leads to an even higher shift given by [Koch07]

$$\chi \approx -\frac{g^2 E_C/\hbar}{\Delta(\Delta - E_C\hbar)}. \qquad (3.8)$$

In general both the qubit and the resonator eigenfrequencies are renormalized, which in the two level approximation leads to the new resonator
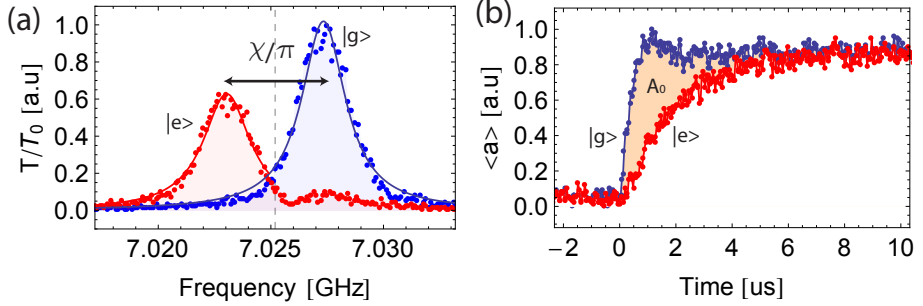
Figure 3.3: (a) Pulsed transmission spectroscopy of the resonator with the qubit either prepared in the ground or excited state. (b) Measured time traces for two different initial qubit states.

frequency $\omega_r = \bar{\omega}_r \pm \chi$ (the sign depends on the qubit state) and the new atomic transition frequency of $\omega_a = \bar{\omega}_a + 2\chi$. The induced shift for the atomic frequency of 4χ per cavity photon is referred to as AC-stark shift. $\bar{\omega}_r$ and $\bar{\omega}_a$ denote the bare eigenfrequencies of the two uncoupled subsystems. The two different states of the cavity can be recorded by using time resolved spectroscopy as shown in figure 3.3a. Here the signal is integrated after the qubit is either flipped to the excited state or left in the ground state. The qubit detuning for this measurement was $\Delta/2\pi = (\omega_a - \omega_r)/2\pi = (6.135\text{-}7.027)\,\text{GHz} = 892\,\text{MHz}$, the coupling was $g/2\pi{=}55\,\text{MHz}$ and the charging energy was $E_C/h = 360\,\text{MHz}$, which would result in $\chi/2\pi = 23\,\text{MHz}$, consistent with the measured $\chi/2\pi$ of $21\,\text{MHz}$. For a dispersive quantum non-demolition (QND) measurement the dispersive shift of the resonator can also be detected in the time domain [Wallraff05, Bianchetti09]. Starting at a time $t = 0$ a continuous coherent microwave signal ω_m is applied to the resonator. The dispersive Hamiltonian (Eq. 3.7) can be supplemented by a drive of frequency ω_m and time dependent amplitude $\epsilon_m(t)$. Expressed in a frame rotating at the measurement frequency it reads

$$H_{\mathrm{m}} = \frac{1}{2}\hbar\omega_a\sigma_z + (\hbar\omega_r - \hbar\omega_m + \hbar\chi\sigma_z)a^\dagger a + \hbar\epsilon_m(t)(a^\dagger + a). \qquad (3.9)$$

The complex valued signal measured with the previously discussed detection scheme (Sec. 3.2) is then given by [Bianchetti10]

$$S(t) = \sqrt{Z\hbar\omega_m\kappa}\langle a(t)\rangle, \tag{3.10}$$

which is proportional to the time evolution of the intracavity field. Z is the characteristic impedance of the system. Similar to the transmission spectrum (figure 3.3(a)), the dynamics of this signal depends on whether the system is in the $|g\rangle$ or the $|e\rangle$ state. The two corresponding timetraces are shown in figure 3.3(b). The area enclosed by the ground and excited state response A_0 can be compared to the one enclosed by the ground state and any unknown quantum state A'. It can be shown by employing the optical Bloch equations, that the population $P_e = (\langle\sigma_z\rangle + 1)/2$ for all possible values of $\langle\sigma_z\rangle$ is simply given by the ratio A'/A_0 [Wallraff05]. In more detail the expectation value of our repeated population measurement can also be described by an observable $\hat{\mathcal{M}}$ such that $\langle\hat{\mathcal{M}}\rangle = Tr(\rho\hat{M})$ where

$$\langle\hat{\mathcal{M}}\rangle = \alpha_0 |0\rangle\langle 0| + \alpha_1 |1\rangle\langle 1|. \tag{3.11}$$

α_0 and α_1 are the integrated timetraces of a ground and excited state.

In combination with single qubit rotations $\hat{U}_k$, the expectation value of $\hat{\mathcal{M}}$ is

$$\langle\hat{\mathcal{M}}\rangle = Tr(\hat{U}_k^\dagger M \hat{U}_k \rho). \tag{3.12}$$

Performing this type of measurement along three different rotation angles, in practice chosen to be orthogonal, allows to infer the full information of a single qubit quantum state.

The technique described can also be generalized to the joint read out of multiple qubits [Filipp09, Leek09, DiCarlo09]. For example in the case of two qubits coupled to a resonator the measurement operator reads

$$\langle\hat{\mathcal{M}}_\in\rangle = \alpha_{00} |00\rangle\langle 00| + \alpha_{01} |01\rangle\langle 01| + \alpha_{10} |10\rangle\langle 10| + \alpha_{11} |11\rangle\langle 11|, \tag{3.13}$$

which is equivalent to

$$\langle\hat{\mathcal{M}}_\in\rangle = \beta_{00}\hat{I} + \beta 01\hat{I}\otimes\hat{\sigma}_z + \beta 10\hat{\sigma}_z\otimes\hat{I} + \beta 11\hat{\sigma}_z\otimes\hat{\sigma}_z \tag{3.14}$$

Each β is calibrated by measuring the averaged transmission signal for each corresponding computational basis state. A single averaged measurement trace of the transmitted signal then gives information about the joint qubit state.
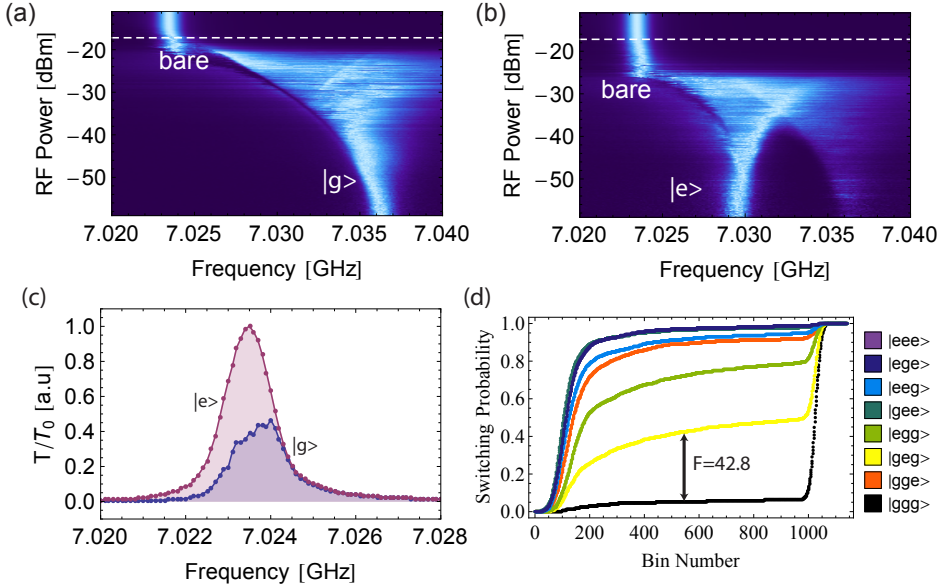
Figure 3.4: (a/b) Pulsed transmission spectroscopy of the for different powers of the coherent tone once with the qubit prepared in either $|g\rangle$ (a) or $|e\rangle$ (b). The measured signal was integrated for 800 ns after the end of the qubit manipulation. (c) Pulsed transmission spectroscopy for a power of -17.2 dBm. The signal is normalized to the $|e\rangle$ response. (d) Switching probabilities for all three qubit basis states. The overall fidelity F is given by 42.8 %.

3.3.2 High Power Read Out

In addition to the joint dispersive readout of the QND type another read out scheme was used for the tomographic state reconstructions presented in this thesis. It was shown that the nonlinearity of the Jaynes-Cummings energy ladder can be used to obtain single shot readout of up to three qubits [Reed10, DiCarlo10, Boissonneault10, Bishop10]. A detailed description of the technique can also be found in [Bianchetti10]. The idea is as follows. For high enough photon numbers $n \gg n_{crit}$ we expect the qubit-cavity coupled system to act classical and the cavity maximum transmittance is found at the bare cavity frequency. If the probe field is injected at time

$t = 0$, after the qubit has been prepared in either $|g\rangle$ or $|e\rangle$, the power at which the cavity starts acting purely classical depends on the initially prepared state. In figure 3.4(a/b) we have integrated the transmittance from $t = 0$ to $t = 800$ ns and plotted it versus injected power and frequency. As can be seen in figure 3.4(c) for a input power of -17.2 dBm (this number depends on the specific cabling configuration and does not necessarily contain meaningful information) the cavity has switched to a bright bare state only if the qubit was prepared in the excited state. However if the qubit is prepared in the ground state, the cavity is in some bifurcation regime and shows a distorted shape. This allows to measure the qubit state with a very high power, which effectively improves the signal to noise ratio. The scheme can be generalized to multiple qubits, as long as for all involved computational basis states the signal can be sufficiently discriminated from the ground state response. The switching probabilities are shown in figure 3.4(d). The overall fidelity of the multi-qubit read-out can be defined by maximal separation between the probability-curve for the state one is trying to detect and the least distinguishable state in this case the $|geg\rangle$ state. This means that the overall fidelity is limited by the single shot fidelity of that specific qubit, even though the other two single shot fidelities are significantly higher, namely 85.5 for $|gge\rangle$ and 72.9 for $|egg\rangle$. To increase the detection efficiency of multi-qubit quantum states is has therefore proven helpful to map all states to be detected to the $|ggg\rangle$ state and then measuring [DiCarlo10].

3.3.3 Fluorescence read out and parametric amplification

The readout in the bad cavity limit $\kappa \gg g \gg \gamma$ requires a different method. The standard dispersive read-out is based on state dependent frequency shifts of the resonator, where the shift χ is larger than the resonator's bandwidth κ. To resolve a small shift of a much broader resonator therefore would set unreasonable demands for the signal to noise. As the superradiance experiments, presented in chapter 7, rely on the direct measurement of emitted photons we have decided to use this method also to measure the qubit population as explained in more detail below.

Single qubit rotations can be applied while the qubit is at a frequency ω_0, off-resonant from the cavity. Once the qubit is tuned in resonance $\omega_0 = \omega_r$ it will decay via the resonator into the detection line. As basically
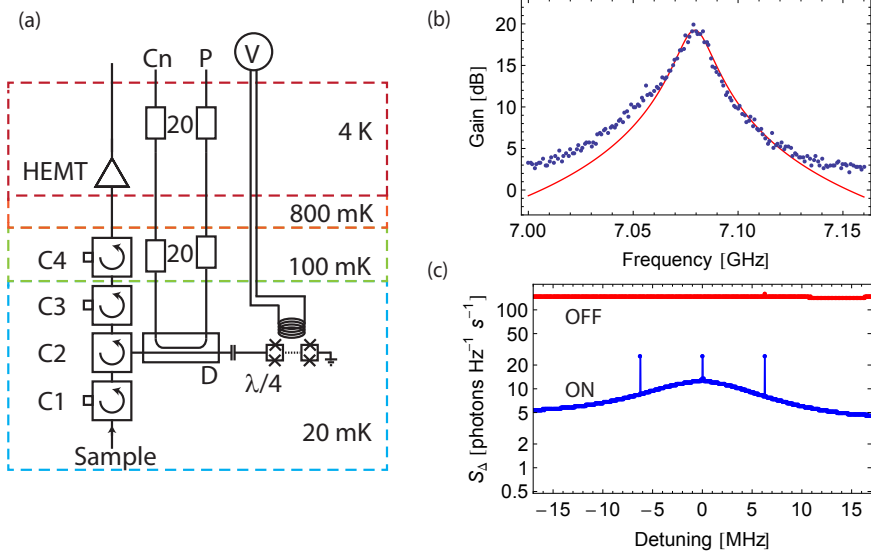
Figure 3.5: (a) Schematic of cryogenic circuitry of the Josephson parametric amplifier with C1-C4:circulators, D: directional coupler, Cn: Compensation, P: Pump. (b) Experimental gain curve of the parametric amplifier (dots) and Lorentzian fit (solid line) once tuned to the resonator frequency. (c) Measured power spectral density S_Δ relative to the pump frequency for the parametric amplifier pump turned on (blue) and off (red). The spectra are scaled such that the coherent peak at $6.25\,\text{MHz}$ corresponds to the number of photons emitted per Hz and per second from the resonator.

no more coherent exchange of excitation takes place between the qubit and the cavity in the bad cavity regime, a general qubit state $\alpha\,|g\rangle + \beta\,|e\rangle$ is formed into a purely photonic state $\alpha\,|0\rangle + \beta\,|1\rangle$. This mapping is justified because in the bad cavity limit the resonator mode can be adiabatically eliminated and thus treated as a simple decay channel [Delanty11]. Nevertheless this method requires the detection of fractions of single photons on average and a parametric amplifier is needed to increase the signal to noise ratio. A detailed discussion about parametric amplifiers can be found in [Eichler13, Eichler14]. The basic principle of such a device is to exploit the

nonlinearity of a $\lambda/4$ resonator shunted to ground via an array of SQUIDs. The inductance of each SQUID depends nonlinearly on the current flowing through it. The amplification is achieved by pumping the amplifier at a frequency and with a power such that the phase of the reflected signal depends sensitively on the power. Any additional small signal at the input will induce a large change in the reflected signal. As the critical current of the SQUIDS depends on the magnetic flux penetrating their loop, it is possible to match the amplification band to the frequency of the signal to be amplified. The integration of the parametric amplifier into the setup is shown in figure 3.5(a). The constant drive, referred to as pump tone, is injected via a directional coupler. The signal to be amplified is passing two circulators and then is directed to the parametric amplifier's input via the strongly coupled port of the directional coupler also used for injecting the pump. Once the signal is amplified and reflected it is guided to the standard signal output line by passing the second circulator again. The reflected pump signal is suppressed by applying a cancelation tone to the directional coupler, which cancels the reflected pump signal by destructive interference once its phase and amplitude is well set by a room-temperature displacer [Eichler13, Heinzle12, Steffen13a]. The flux tuning of the SQUID array is realized applying a current to the miniature superconducting coil mounted at the backside of the chip. To operate the amplifier reliably, careful calibration is needed [Eichler13, Heinzle12, Govenius12]. The amplifier's performance can be quantified by its gain-bandwidth product as shown in figure 3.5(b), which for the presented data was 160 MHz. This value is expected to be constant, meaning amplification can be achieved either by maintaining a high gain or a high bandwidth. For the read-out of the qubit state with the methods used for this thesis a high bandwidth is secondary and amplification is mainly required to improve the signal to noise ratio, otherwise limited by the HEMT amplifier. It is therefore instructive to characterize the system noise temperature as shown in figure 3.5(c). This measurement is based on populating the cavity with a well-known average photon number $\bar{n}$ by injecting a coherent tone in the resonator input line, once with the amplifier's pump turned on or off. The coherent output power is given by $P = \hbar\omega_{res}\bar{n}\kappa$. A well-known average photon number can only be prepared if one initially performs a single-photon calibration discussed in chapter 4.3. The measured power spectral density S_Δ is then scaled such that the height of the coherent peak relative to the noise offset
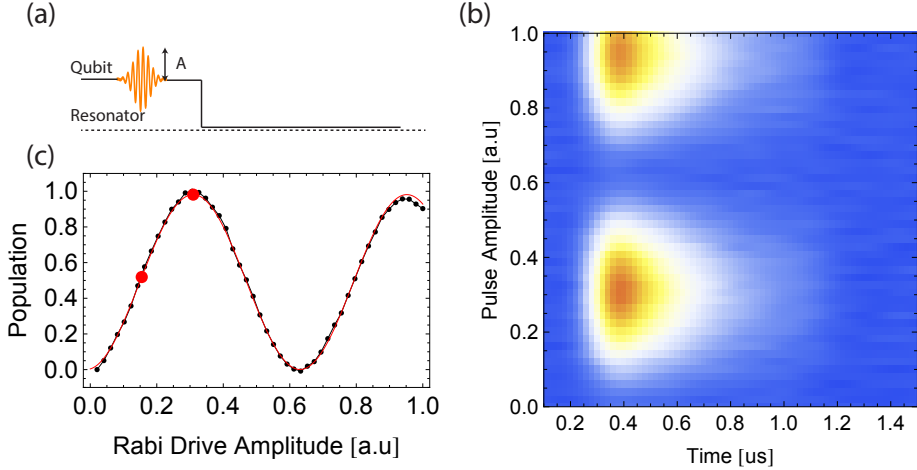
Figure 3.6: (a) The intracavity field is prepared by a single qubit rotation while the qubit is far off-resonant with the resonator and resides at its bias frequency. Once the single qubit state is prepared the qubit is tuned on resonance, such that its excitation can decay via the cavity into our detection line. (b) Timetrace of a heterodyne $\langle S^\dagger S \rangle$ measurement. (c) Outcome of the fluorescence state mapping. The qubit population, inferred from the time integrated photon number measurement of figure b, is shown for a qubit preparation where Rabi pulses with linear increasing amplitude were used.

is equal to $\bar{n}\delta f$, where $\delta f = 100\,\mathrm{MHz}/2048 \sim 49\,\mathrm{kHz}$ is the bin size of the specific power spectral density measurement. We then can interpret the power spectral density as number of photons emitted from the cavity per Hz and per second. The extracted system noise, in a frequency range close to the coherent tone, was determined to be $N_{\mathrm{system}} + 1 \approx 6$ photons, which gives an offset of 5 photons from the quantum limit, due to attenuation in the cables and impedance mismatches.

To measure the intracavity photon number we extract $\langle a^\dagger a \rangle$, which is done in real-time on the FPGA by squaring individual time-traces before averaging them [Eichler12, Bozyigit11].

In fact the heterodyne setup is used to extract the complex amplitude $S(t)$

as discussed in chapter 3.2. The recorded signal consists of the experimental signal plus thermal noise and can be written as

$$S(t) = a + h^\dagger \tag{3.15}$$

To extract the photon number, $S^\dagger S$ is calculated in real time on the FPGA and then averaged over $\sim 10^6$ instances of the same experiment. We then get

$$\langle S^\dagger S \rangle = \langle (a^\dagger + h)(a + h^\dagger) \rangle \tag{3.16}$$

$$= \langle a^\dagger a \rangle + \langle a^\dagger h^\dagger \rangle + \langle ha \rangle + \langle hh^\dagger \rangle \tag{3.17}$$

$$= \langle a^\dagger a \rangle + \langle hh^\dagger \rangle \,, \tag{3.18}$$

as our experimental signal is uncorrelated with the noise and averages out. If we then record the constant noise floor $\langle hh^\dagger \rangle$ in an OFF-measurement, that is where no experimental signal is present, and subtract it from our ON-measurements, we have direct access to the photon number in the cavity assuming the thermal background of the resonator is constant within the time of the two successive measurements. A power measurement is shown in figure 3.6(b) where the qubit was prepared by Rabi-pulses, linear increased in amplitude (see 3.6(a)), and then tuned into resonance with the cavity. The signal was amplified by a parametric amplifier and a HEMT amplifier. Figure 3.6(c) shows the time-integrated and renormalized signal, which indicates that the presented fluorescence read-out indeed gives direct information about the qubit population and in addition with single qubit rotations, would allow to fully characterize its state.

$$4$$

Spectroscopic Measurements

4.1 Theoretical description of transmittance measurements

Once a sample is mounted in the cryostat, most parameters can be extracted by well established spectroscopic measurements [Thompson92, Wallraff04, Schuster07, Fink10a]. However for the data presented in this thesis, a useful interpretation required a theoretical framework, which can be applied both in the strong coupling as well as in the bad cavity limit as presented below.

Spectroscopy is based on measuring the transmittance T of some coherent probe tone with variable frequency ω and incident amplitude $\mathcal{E}(t)$ or power $P_0 = |\mathcal{E}_0(t)e^{-i\omega t}|^2$ respectively. The resonator frequency is ω_r and the qubit frequency is ω_a. The probe frequency can be expressed in terms of the detuning $\delta\omega = \omega_p - \omega_r$. Most relevant parameters such as the coupling strength emerge clearly once the qubit is exactly on resonance with the resonator and we therefore use a rotating frame $\omega_r = \omega_a = 0$. We start off with the master equation 2.43 and the interaction Hamiltonian H_{int} (see equation 2.27) for a single two-level system coupled to a single mode in the presence of a constant probe tone with amplitude $\mathcal{E}(t)$:

$$\hat{\mathcal{H}}_{\text{JC}} = \hat{H}_{int} = \hbar g(\hat{a}^\dagger \hat{\sigma}^- + \hat{\sigma}^+ \hat{a}) + \mathcal{E}(t)\left(a^\dagger e^{-it\omega} + ae^{it\omega}\right). \qquad (4.1)$$

The dynamics of an observable A is then determined by $\langle \dot{A} \rangle = Tr[A\dot{\rho}]$,

which for the field and atomic operators leads to [Scully97]

$$\langle \dot{a} \rangle \quad = \quad -i\omega_r \langle a \rangle - ig \langle \sigma_- \rangle - \frac{\kappa}{2} \langle a \rangle + \mathcal{E} e^{-i\omega_p t} \qquad (4.2)$$

$$\langle \dot{\sigma_-} \rangle \quad = \quad -i\omega_q \langle \sigma_- \rangle + ig \langle a \rangle - (\frac{\gamma_1}{2} + \gamma_\varphi) \langle \sigma_- \rangle \qquad (4.3)$$

where we used the weak drive limit, i.e .the approximation $\langle \sigma_z a \rangle \sim \langle a \rangle$. As we are looking for the steady state solution, the field number operators do not depend on time and we can use the ansatz $\langle a \rangle = a_0 e^{i\omega t}$, which leads to the set of two coupled linear equations:

$$-ia_0\omega \quad = \quad -\frac{a_0\kappa}{2} - ia_0\omega_r - ia_0 - ig\sigma_0 \qquad (4.4)$$

$$-i\sigma_0\omega \quad = \quad -i\sigma_0\omega_a + iga_0\sigma_0 - \sigma_0 \left(\gamma_\varphi + \frac{\gamma_1}{2} \right), \qquad (4.5)$$

which can be solved to give

$$T(\delta\omega) = T_0 \left| \frac{\lambda + \frac{1}{2}i \left(\frac{\kappa}{2} - \Gamma_2 \right)}{\frac{1}{2}i \left(\Gamma_2 + \frac{\kappa}{2} \right) + \delta\omega + \lambda} - \frac{-\lambda + \frac{1}{2}i \left(\frac{\kappa}{2} - \Gamma_2 \right)}{\frac{1}{2}i \left(\Gamma_2 + \frac{\kappa}{2} \right) + \delta\omega - \lambda} \right|^2 \qquad (4.6)$$

where we have defined $\lambda = \sqrt{g^2 - \frac{1}{4} \left(-\frac{\gamma_1}{2} - \gamma_\varphi + \frac{\kappa}{2} \right)^2}$ and $\Gamma_2 = \frac{\gamma_1}{2} + \gamma_\varphi$. We can now approximate this general expression for the specific parameter limits we are interested in.

4.1.1 Strong Coupling Limit

In the strong coupling limit, $g \gg \kappa, \gamma_1, \gamma_\varphi$, we get

$$T(\delta\omega) = T_0 \left| \frac{g + \frac{1}{2}i \left(\frac{\kappa}{2} - \Gamma_2 \right)}{\frac{1}{2}i \left(\Gamma_2 + \frac{\kappa}{2} \right) + \delta\omega + g} - \frac{-g + \frac{1}{2}i \left(\frac{\kappa}{2} - \Gamma_2 \right)}{\frac{1}{2}i \left(\Gamma_2 + \frac{\kappa}{2} \right) + \delta\omega - g} \right|^2 \qquad (4.7)$$

with the normalization

$$T_0 = \frac{(2\Gamma_2 + \kappa)^2}{(\kappa - 2\Gamma_2)^2 + 16g^2} \qquad (4.8)$$

Because the relevant variation in T occur at $\delta\omega \approx \pm g$, we can further simplify to

$$T(\delta\omega) = \frac{\left(\Gamma_2 + \frac{\kappa}{2} \right)^2}{\left(\Gamma_2 + \frac{\kappa}{2} \right)^2 + (\delta\omega + g)^2} + \frac{\left(\Gamma_2 + \frac{\kappa}{2} \right)^2}{\left(\Gamma_2 + \frac{\kappa}{2} \right)^2 + (\delta\omega - g)^2}, \qquad (4.9)$$
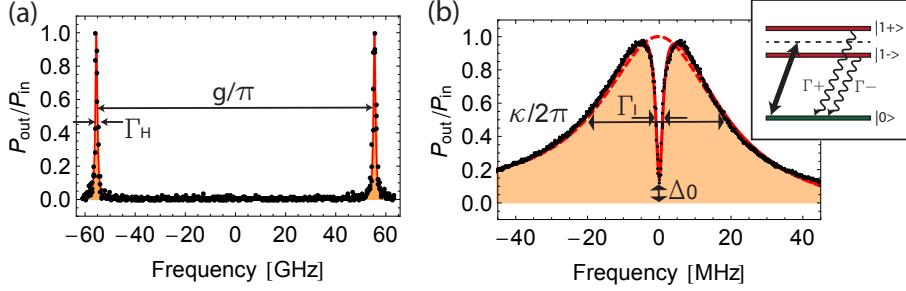
Figure 4.1: Transmission spectroscopy with the qubit tuned on the resonator frequency ω_r in the (a) strong coupling limit leading to two well separated polariton peaks and (b) in the bad cavity limit where the qubit leads to a narrow dip inside the broad resonator peak.

which represents two Lorentzian peaks with a width of $\Gamma_H = \Gamma_2 + \kappa/2$ and a separation of $2g$. A fit of this function to the data is shown in figure 4.1(a). Here $\kappa/2\pi$ has been fixed to 474 kHz as extracted from data with detuned qubits. The coupling $g/2\pi$ is 55.5 MHz and the polariton linewidth is Γ_H=0.91 MHz. The individual determination of γ_1 to γ_φ requires time resolved measurements as discussed in chapter 5.2.

4.1.2 Bad Cavity Limit

In the bad cavity limit, $\kappa \gg g \gg \gamma_1, \gamma_\varphi$ equation 4.6 can be approximated as

$$T(\delta\omega) = \left| \frac{\kappa/2}{\delta\omega + i\frac{\kappa}{2}} - \frac{2g^2/\kappa}{\delta\omega + i\left(\Gamma_2 + \frac{g^2}{\frac{\kappa}{2} - \Gamma_2}\right)} \right|^2, \tag{4.10}$$

which can be interpreted as a narrow Lorentzian *subtracted* from a broad Lorentzian. A fit of this function to the data is shown in figure 4.1. The width of the broad Lorentzian peak is set by the cavity decay rate $\kappa/2\pi$ while the narrow Lorentzian dip has a width of $\Gamma_I = 2\Gamma_2 + 4g^2/(\kappa - 2\Gamma_2)$. The minimum transmission Δ_0 on resonance ($\delta\omega = 0$) is given by

$$\Delta_0 = \Gamma_2/(\Gamma_\kappa + \Gamma_2) \tag{4.11}$$
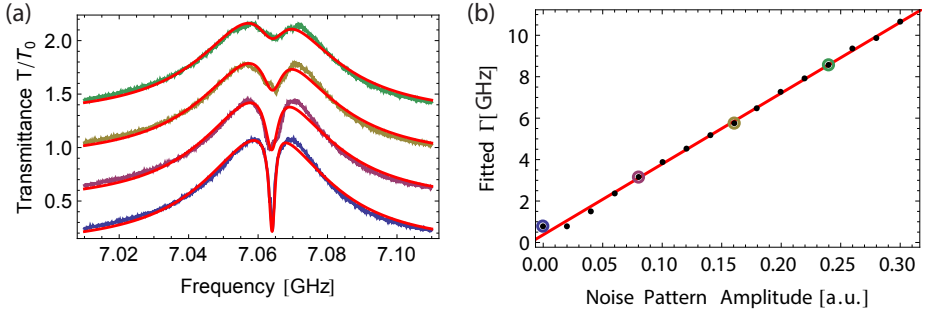
Figure 4.2: (a) Transmission spectroscopy in the bad cavity limit in the presence of noise introduced via the qubit's flux gate line. (b) The extracted decoherence parameter is plotted versus applied noise amplitude (black dots) and shows a linear dependence as indicated by the fit (red solid line). The circles mark the corresponding responses shown in figure (a). For a better visibility an offset has been introduced in T/T_0.

where $\Gamma_\kappa = 4g^2/\kappa$ is defined as the Purcell induced decay rate on resonance in the bad cavity limit. Physically, the distinct shape of the measured spectrum is understood in terms of atom enhanced absorption [Rice88], which is closely related to electromagnetically induced transparency [Fleischhauer05] or cavity induced transparency [Rice96]. Intuitively, the coherent scattering of the probe field detuned by the same frequency but with opposite sign from the excited state doublet ($|1+\rangle, |1-\rangle$) formed by the long-lived qubit resonantly coupled to the bad cavity (Fig. 4.1(b, inset)) leads to the dip in the spectrum due to destructive interference [Fleischhauer05]. It is worth noting that the spectrum can also be fully explained by the linear response of a driven resonator mode in the presence of dispersion and absorption [Zhu90] and does not necessarily require a quantum mechanical treatment. If the condition $g \gg \gamma_1, \gamma_\varphi$ is met, the transition at the center resonance (equation 4.11) should drop to zero. The finite offset of equation 4.11 tells us about the amount of decoherence still influencing the measurements. We can study the dependence of this offset on the decoherence parameters by artificially introducing noise onto the system by using the qubit's flux gate line. To model realistic uncorrelated environmental disturbances, the noise

was synthesized by an arbitrary waveform generator and numerically created conforming to an Ornstein-Uhlenbeck process [Uhlenbeck30], which is a stationary, gaussian and Markovian noise process. The spectral bandwidth of the noise was chosen to be 30 MHz and its amplitude was linearly increased. The transmission spectrum for various noise amplitudes is shown in figure 4.2(a). With increasing noise amplitude the spectrum's narrow dip is broadened and reduced in amplitude and vanishes for even higher powers. Fitting the resulting decoherence parameter Γ_2 with our model of equation 4.10 shows a linear dependence on the noise amplitude, as can be seen in figure 4.2(b).

4.2 Flux dependence

The transmission spectrums can also be generalized to include a finite detuning between the cavity and the qubit. This lifts the symmetry of the spectrum and introduces the qubit frequency as an additional parameter of the system. Without going into details it can be shown, that the splitting in the strong coupling limit, in the case of a qubit-cavity detuning $\Delta = \omega_a - \omega_r$ is given by $\Omega(\Delta) = \sqrt{g^2 + \Delta^2}$, which is minimized for $\Delta = 0$. The bad cavity spectrum still consists of a broad peak and a narrow dip, where the position of the dip is now shifted to the detuned qubit frequency. Experimental data for both limits is shown in figure 4.3. Here the spectrum was taken for several voltages applied to the largest of the three superconducting miniature coils mounted below the chip. A detailed study of the near resonant spectrum for all qubits at multiple crossings with the resonator allows to extract the full transmon energy spectrum by fitting the data to $\nu(V) = \sqrt{8E_C E_J |\cos(\pi(V - V_0)c)|} - E_C$ (compare equation 2.5), where c is the linear coupling constant of the coil defined as $c = \Delta\phi/\Delta V$. Figure 4.3(c) shows a fit to the data taken from the sample used for the experiments described in chapter 7. Generally we fixed E_C to the design value as the electrostatic simulation gives a very reliable value with an uncertainty in the order of about 5 percent. The extracted maximum E_J for the two qubits then are $E_{J,max}/\hbar = (23.05, 19.13)\,\text{GHz}$ corresponding to a maximum transition frequency of $(8.19, 7.42)\,\text{GHz}$. If we would like to individually control N qubits we need to repeat this measurement for the N different required coils. The obtained linear system of equations involves
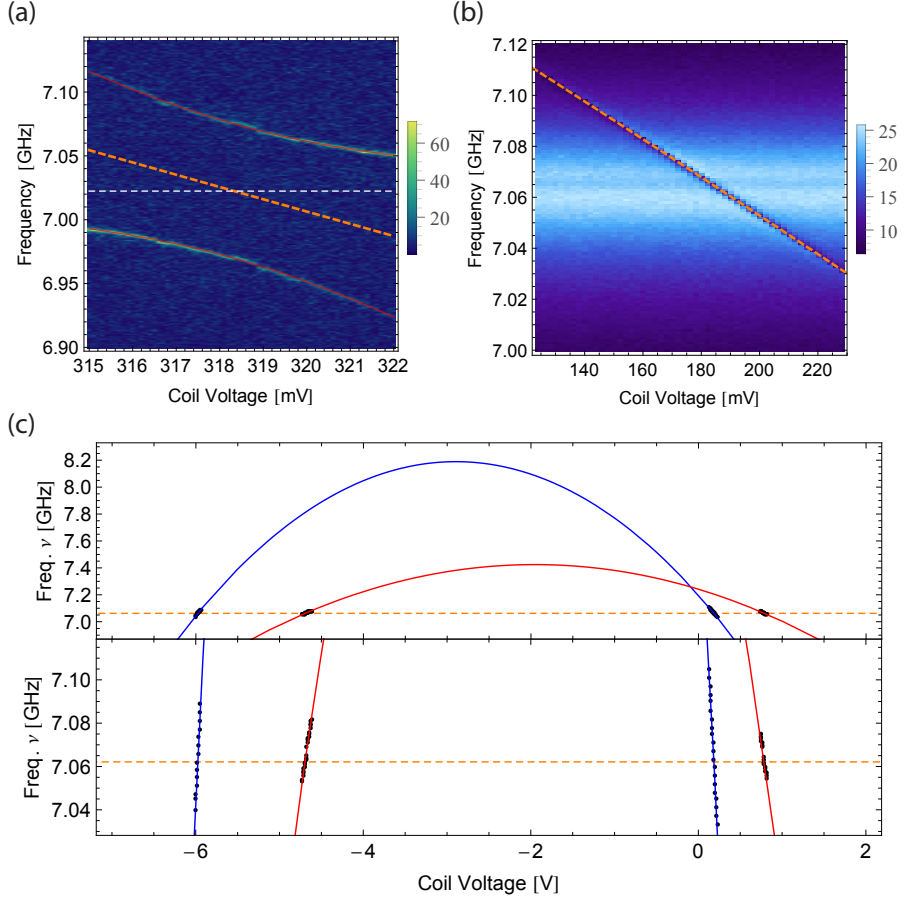
Figure 4.3: Experimentally obtained transmission spectroscopy for different qubit-resonator detunings set by sweeping the coil voltage for (a) the strong coupling limit and (b) for the bad cavity limit. The color bar is given in units of μV. (c) Extracted flux dependence from fitting the near resonant data points at four different crossings of two qubits through the resonator. The shown data was taken in the bad cavity limit.

$N \times N$ different coupling strengths and its solution can be represented by a coil matrix [Bianchetti10, Fink10a]. In contrast to the bad cavity limit the dispersive shift in the strong coupling regime allows to extract the qubit transition frequency also if the qubit is far detuned from resonance. Here qubit spectroscopy can be used, which has found various application in the field of circuit QED and is described in more detail in [Schuster07, Fink10a]. The dispersive qubit spectroscopy is based an injecting a second microwave tone ν_{spec}, which is combined with the resonant resonator microwave tone at ν_r. Whenever ν_{spec} is swept into resonance with a qubit transition the resonator experiences a dispersive shift leading to a decrease of the transmittance of the measurement signal at ν_r [Bianchetti10].

4.3 Photon number calibration

To put a figure of merit to the detection efficiency and to judge how well our used detection scheme works on a single photon level, noise power spectra (see figure 3.5) have proven to be a useful tool, if they are recorded once with a well known number of intracavity photons and once with the cavity in the vacuum state [Eichler11, Eichler12]. However this requires that the cavity can be either prepared in a Fock state or into a well-defined coherent state. If we infer the detection efficiency from the first method, we can't discriminate insufficient detection efficiency from limitations in the preparation of the Fock state. The latter method therefore is more reliable, provided that we know how the intracavity photon number relates to the power of a coherently injected microwave tone. This relation can be obtained by a photon number calibration. Both in the strong coupling as well as in the bad cavity limit, the mean number of cavity photons can be extracted from spectroscopic measurements if they are recorded on dependence of the coherent microwave power [Fink10b].

4.3.1 Strong coupling

In the strong coupling limit the photon number calibration can be done by making use of the number dependent dispersive shift of the qubit also known as AC stark effect [Schuster05], which is also discussed in chapter 2.3. Therefore dispersive qubit spectroscopy is performed in the presence of a strong drive, such that $2\chi \ll \Omega_{Rabi}$ and the qubit line is broadened,
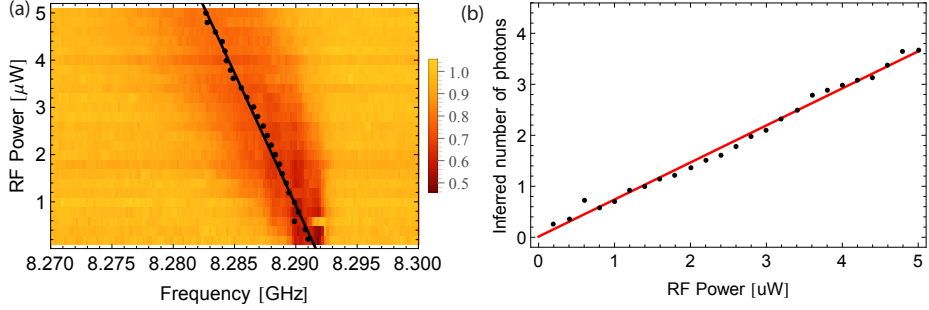
Figure 4.4: (a) Photon number calibration in the strong coupling limit by qubit spectroscopy for linear increasing measurement power. The data was normalized on the incident amplitude. The fit results of the center frequency for the broadened and shifted peak are indicated by the black points.(b) Relation of the number of cavity photon number to the applied cavity input power (black points) as inferred from a the linear fit (red line).

such that individual photon number split qubit lines can not be resolved anymore. In addition to the broadening the qubit line is shifted as can be seen in figure 4.4(a). As this shift is linear with the number of cavity photons, namely $\nu_{ge}(0) + 2\chi\bar{n}$ we have a direct access to $\bar{n}$ as a function of applied drive power Ω_{Rabi}. This calibration relies on a prior determination of the coupling constant g (see equation 3.8). From the data shown in figure 4.4(b) we can conclude that a mean number of one photon, $\bar{n}=1$ corresponds to a microwave power of $1.36\,\mu\text{W}$ = -28.7 dBm at the RF generator output.

4.3.2 Bad cavity

In the bad cavity limit the presented AC Stark shift is not the method of choice for the same reason qubit spectroscopy is hard to realize, because $\chi \ll \kappa$. Nevertheless for the coupled system we expect a nonlinear behavior of the cavity's photon population with respect to the applied drive power if $\bar{n} \ll n_{crit}$. For a purely classical, i.e. uncoupled system, the photon number is expected to vary linearly with the coherent drive tone's power (see figure 4.5(b)). Indeed the nonlinear response becomes apparent in the resonant

spectrum as shown in figure 4.5(a). Here an increase in drive power leads to a broadening of the dip and to a decrease of its depth with respect to the broad Lorentzian peak dominated by κ. We measure the transmission amplitude $\langle a \rangle$ at the center of the dip as a function of coherent power, to which the signal than is normalized (see figure 4.5(c)). The observed data has an initial offset given by equation 4.11, respectively to its square root as we measure transmission amplitude instead of transmission power. It then asymptotically approaches the classical linear response. The initial offset and the power at which our signal is within a certain range relative to the classical value, here indicated as δ, leads to two parameters, which can be compared with a master equation simulation to finally obtain the photon number calibration. For the master equation we use the expression as discussed in chapter 2.5 and include system parameters independently obtained from transmission spectroscopy. For our numerical simulation we include four photonic levels and vary the drive amplitude $\mathcal{E}(t)$ in the nonlinear region of the response, i.e. up to a mean photon number of ≈ 0.1. Using this method we estimate a mean number of one photon $\bar{n} = 1$ to correspond to a power of $24.6\,\mathrm{mW}$ or $13.9\,\mathrm{dBm}$ set at the output port of our generator.
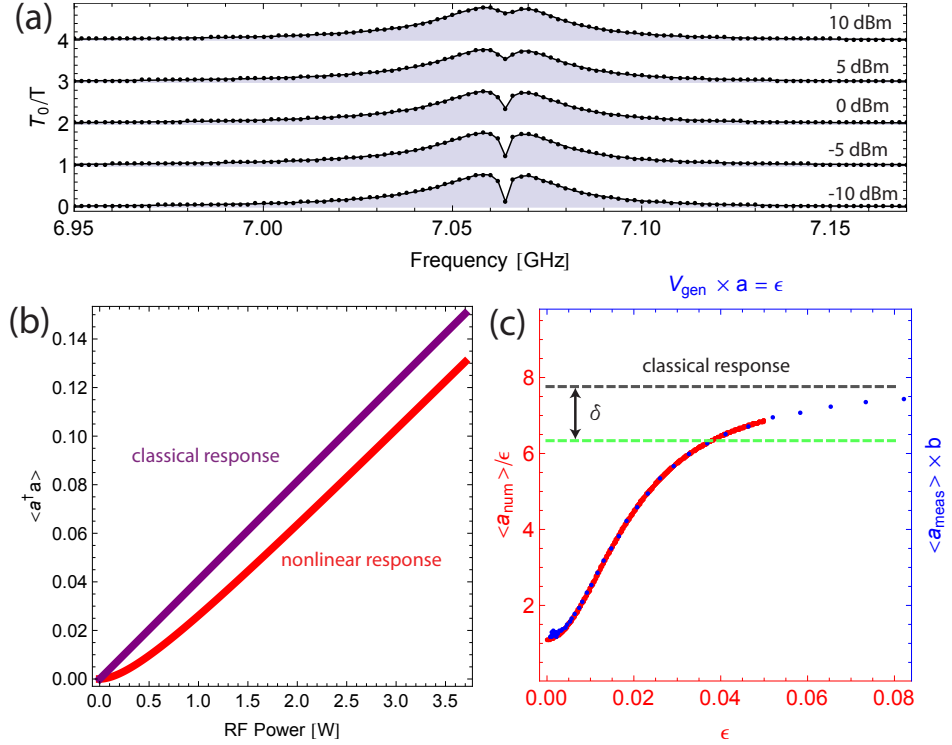
Figure 4.5: (a) Transmission spectroscopy in the bad cavity limit for various coherent drive powers. For clarity the data is offset. (b) Comparison between the classical (purple) and quantum response (red) for the probe frequency at ω_p=7.061 GHz. The coupling of the qubit leads to a nonlinear behavior, which can be used for the photon number calibration. (c) Measured transmission amplitude $\langle a \rangle$ at ω_p=7.061 GHz normalized to the amplitude of the drive. The experimental data (blue points) is scaled along the x-and y axes by the fit parameters a and b to match the master equation simulation (red). For a purely classical system the response would be flat (dark red line). The discrepancy δ between classical and measured response for a given coherent power allows to infer the mean cavity photon number $\bar{n}$.

5

Single Qubit Manipulation and Dynamics

Once it comes down to resolve the time evolution of states or to exploit their dynamics for the implementation of gates, individual control of the qubit plays a crucial role. This involves both the ability to prepare arbitrary single qubit states $|\Psi\rangle = \alpha |0\rangle + \beta |1\rangle$ but also to change the qubit transition frequency on a timescale $t \ll g$ to tune it into resonance with either the resonator or another qubit. Therefore the fidelity of single and multi-qubit gates depends strongly on the quality of the applied pulses. In this chapter I introduce the microwave setup used for this purpose and a possible method for flux pulse optimization. I discuss the basic experiments, which are subject to the time evolution of a single qubit coupled to a single mode of the electromagnetic field. It is shown how the data can be used to extract the key coherence parameters of the system, not fully accessible using spectroscopic methods.

5.1 State preparation

The qubit state is controlled by a coherent microwave signal with frequency ω_d near the qubit transition frequency ω_q. The state of the qubit depends on the length of the pulse, its amplitude $\mathcal{E}(t)$, its phase ϕ and the microwave frequency ω_d. In a frame rotating at the drive frequency ω_d the effective

Hamiltonian for the qubit can be written as ($\hbar = 1$)

$$H_{\text{drive}} = \frac{\Delta_{\text{q}}}{2}\hat{\sigma}_z + \frac{\Omega_R(t)}{2}\left(\cos(\varphi)\hat{\sigma}_x + \sin(\varphi)\hat{\sigma}_y\right) \tag{5.1}$$

with $\Delta_q = \omega_q - \omega_d$ the detuning of the qubit transition frequency from the drive and $\Omega_R(t) \propto \mathcal{E}(t)$ the Rabi frequency. $\sigma_x, \sigma_y, \sigma_z$ are the Pauli spin-operators. For a fixed detuning Δ_q and constant amplitude Ω_R the Hamiltonian is time independent and the general solution of the Schrödinger equation $i\hbar\frac{\partial}{\partial t}\Psi = H\Psi$ is given by $\Psi(t) = \Psi(0)e^{-iHt}$. If we set our initial state to be the ground state $\Psi(0) = |0\rangle$ and look at the resulting state for a resonant drive pulse of length τ, the evolution under equation 5.1 leads to

$$\Psi(\tau) = \alpha|0\rangle + \beta|1\rangle \tag{5.2}$$

with $\alpha = ie^{-i\varphi/2}\cos\frac{\Omega_R t}{2}$ and $\beta = e^{i\varphi/2}\sin\frac{\Omega_R t}{2}$, meaning that any arbitrary state on the Bloch-sphere can be prepared. Rotations around the x-axis are generated by $\hat{\sigma}_x$ and the y-axis rotation is accomplished by $\hat{\sigma}_y$. By changing the phase ϕ of the qubit drive, rotations around arbitrary axes lying on the equator of the Bloch-sphere are realized. A finite detuning $\Delta_q \neq 0$ induces rotations around the z-axis of the Bloch-sphere.

The population of the qubit is given by the probability of finding the qubit in the upper state, which is given by $|\beta|^2$ of equation 5.2, namely

$$P(\tau) = \cos^2\frac{\Omega_R\tau}{2}. \tag{5.3}$$

The upper and lower state population therefore is exchanged at a rate of Ω_R. The final state depends on the product $\Omega_R\tau$ also known as pulse area, implying that rotations can be controlled either by varying the amplitude or the duration of the pulse. Moreover pulses do not need to be square shaped, as long as the integrated area underneath is chosen in accordance to the desired rotation. (Indeed due to the sharp edges it is likely bad if square pulses are used.) The experimental reconstruction of the qubit population versus applied drive power was already shown in figure 3.6. Here a gaussian shaped pulse with a standard deviation of 10 ns truncated to an overall duration of 40 ns was applied [Steffen03]. The data was fitted using equation 5.3 and well reproduces the sinusoidal dependence. The Rabi measurement is used to extract the amplitude for $\pi/2$- and π-pulses,
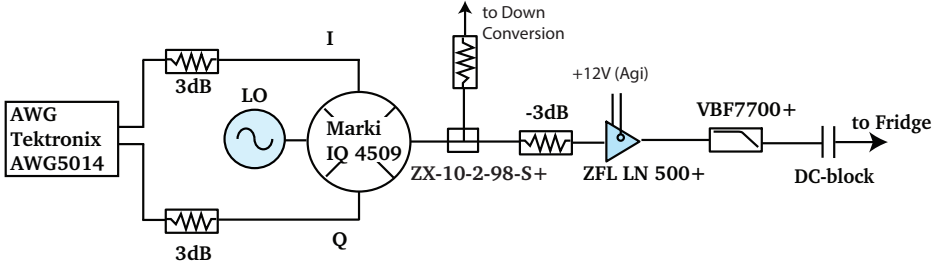
Figure 5.1: Schematic drawing of an up-conversion board used for qubit manipulation. The signal is split and either goes into the cryostat or directly to the down-conversion for mixer calibration.

needed to bring the qubit from the ground state either into a fully symmetric superposition state or fully into the excited level. In general, for Rabi experiments [Rabi37, Vion03] the used drive pulses are chosen to be short with respect to the qubit's decoherence times γ_1 and γ_φ as part of the qubit's population is already lost while the qubit is driven to the excited state. Using the optical-Bloch equations [Bianchetti10] one can show that in the limit of large driving fields ($\Omega_R \gg \gamma_1, \gamma_\varphi$) the population is described by

$$P(\Omega_R) \cong \frac{1}{2} - \frac{1}{2}e^{-\frac{\tau}{4}(3\gamma_1 + 2\gamma_\varphi)}\cos(\Omega_R\tau). \tag{5.4}$$

Even though full qubit state control can be obtained by using just simple square pulses, in practice it is more beneficial to use truncated gaussian shaped pulses, as they have small fourier components at frequencies close to the anharmonicity α of the qubit. Nevertheless the width 2σ of the gaussian pulses is chosen to be short to overcome decoherence as mentioned above. As a consequence, once the pulse bandwidth $B = 1/2\pi\sigma$ is on the order of α, a temporary population of the transmon state $|2\rangle$ might become a problem. Therefore, to maintain our ability to use short pulses, we use so-called DRAG pulses [Motzoi09, Gambetta11a], which have been implemented by optimum pulse control and are designed to reduce the leakage into non-computational states.

In practice it is hard to generate arbitrarily shaped pulses in the GHz frequency range, as our commercial arbitrary waveform generators (AWGs)
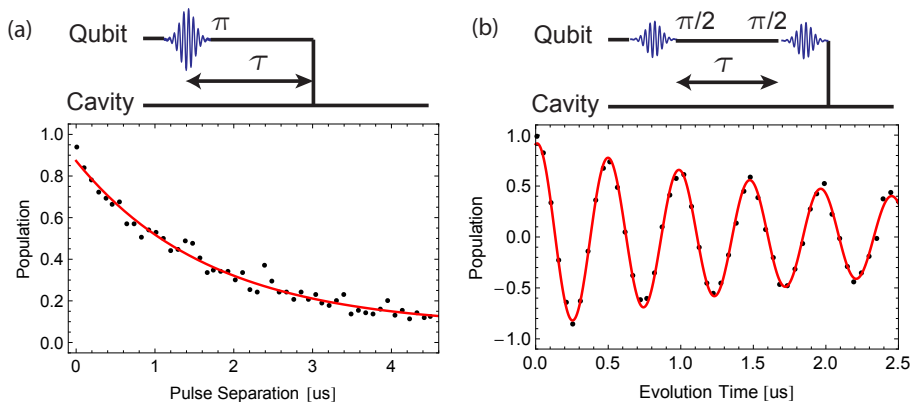
Figure 5.2: Time resolved measurements performed in the bad cavity limit to extract the qubit's relaxation Γ_1=1.7 µs (a) and dephasing constants Γ_2=2.7 µs(b). The respective pulse schemes are also shown.

are limited to a sampling rate of a few GHz. Therefore typically up-conversion techniques are used where a low frequency signal of typically 100 MHz is generated with desired shape and phase and then multiplied with a high frequency microwave signal of a local oscillator by using an IQ-mixer [Schmidlin09, Baur12a]. The hardware implementation of such an up-conversion board is shown in figure 5.1.

The drive tone can be applied to the qubit either via the resonator or by a qubit dedicated charge gate line, allowing to address a single qubit without affecting other qubits that may have a close-by transition frequency. A typical charge gate line was shown in figure 2.1 and represents a CPW transmission lines capacitively coupled to the qubit.

5.2 Extraction of decoherence parameters

The techniques discussed so far allow to perform the basic experiments, which are needed to extract the main decoherence parameters of the system, namely the qubit energy relaxation γ_1 and the qubit pure dephasing γ_φ at the static bias frequency of the qubit. Those parameters are a key benchmark of any quantum information device and their optimization has

dramatic input on the scalability of quantum systems and for further pursuing the ultimate goal of quantum information, which is the realization of efficient quantum simulation and computing devices. The energy relaxation γ_1 can be extracted from a T_1 measurement, where the qubit is initially prepared in a fully excited state $|1\rangle$ and then measured after a time t. The resulting population $P(t)$ can easily be calculated by the master equation 2.43 and reads

$$P(t) = e^{-t\gamma_1}. \tag{5.5}$$

The pulse sequence and experimental data for a bad cavity sample is shown in figure 5.2(a). By fitting equation 5.5 we extract $T_1 = 1/\gamma_1 = 1.7\,\mu s$ which is likely limited by microwave loss at surfaces and interfaces and might be resolved by using different fabrication techniques [Chang13, Ristè13, Barends14].

The pure dephasing γ_φ can be obtained from a Ramsey type measurement [Ramsey50], which is mainly composed of two $\pi/2$ pulses, separated by a free evolution time of length t. The population of the qubit can be calculated analytically again by using the von-Neumann equation and is given by [Bianchetti10]

$$P(t) = \frac{1}{2} + \frac{1}{2}(cos(\Delta_q t) + e^{-t/T_2}) \tag{5.6}$$

As can be seen the population oscillates as a function of the free evolution time t and at a frequency corresponding to the detuning Δ_q. At the same time the dephasing γ_φ leads to a damping and $T_2 = (\gamma_1/2 + \gamma_\varphi)^{-1}$ is the timescale at which the off-diagonal elements of the qubit's density matrix vanish. The Ramsey measurement therefore allows to extract the pure dephasing, given a T_1 measurement was executed before. In addition it can be used to determine the qubit transition frequency with higher accuracy than obtained from spectroscopic measurements. To better distinguish the oscillation frequency due to a finite Δ_q from a decay and to facilitate the fitting, the initial detuning Δ_q is set to about $2\,MHz$. Figure 5.2(a) shows a Ramsey experiment performed in the bad cavity limit. The extracted qubit detuning is Δ_q=2.05 MHz and the T_2 time is 2.9 μs. The dephasing of the qubit may arise due to charge noise, flux noise or critical current noise [Vion02, Nakamura02, Koch07, Pashkin09] and their suppression requires careful shielding and filtering of possible noise sources.

5.3 Flux Pulse Control

As discussed in chapter 2.1 the qubit transition frequency depends on the magnetic flux penetrating its SQUID loop. For the static bias of the qubits superconducting miniature coils are used. Their magnetic field can be changed on a timescale of milliseconds. However due to their large inductance and the low pass filtering of the bias voltage, they can't be used to tune the qubit frequency on the nanosecond timescale, as required for the experiments discussed in chapters 6 and 7. Therefore each qubit is equipped with an on-chip flux bias line [DiCarlo09] as can be seen in figure 2.1, realized by a CPW transmission line passing near-by the qubit SQUID loop. The aspects of various flux line designs are discussed in more detail in [Baur12a]. A careful design will take into account possible reflections of the current pulse and the capacitative coupling, which decreases the qubit coherence similar as for the charge gate line presented in chapter (2.3). The induced flux shift per applied voltage is determined by the mutual inductance between the qubit SQUID loop and the flux line and can be simulated by 3-D inductance extraction programs such as *FastHenry* [Steiger13, Ott11, Groszkowski11, Fourie11, Kamon94].

To generate the current pulses we use the same AWG model as for the Rabi Drive Pulses (*Tektronix* AWG5014) whose sampling rate is set to $1.0 \, \text{GS/s}$. The signal is further filtered at the cryostat's base plate (see figure 3.1). Ideally the pulses seen by the qubit should be a perfect square pulses. The quality of the experimental data critically relies on the ability to control the shape of the flux pulses. However in practice the pulse is already distorted by the AWG's output itself but also by the various cables and filters it passes through.

The first step towards a better control of the pulse is to infer the corrections that have to be applied to the pulse pattern on the AWG, by measuring the *warm* response of the setup [Bozyigit11] while the cryostat is open and all cables are exposed to room-temperature environment. Therefore a square pulse of length τ is loaded on the AWG and recorded after it passed the wiring to the last connector before the chip's PCB board inside the cryostat. The length τ is chosen larger than the longest pulse that is required for the experiment. The corrected pulse pattern f_{corr} can than be
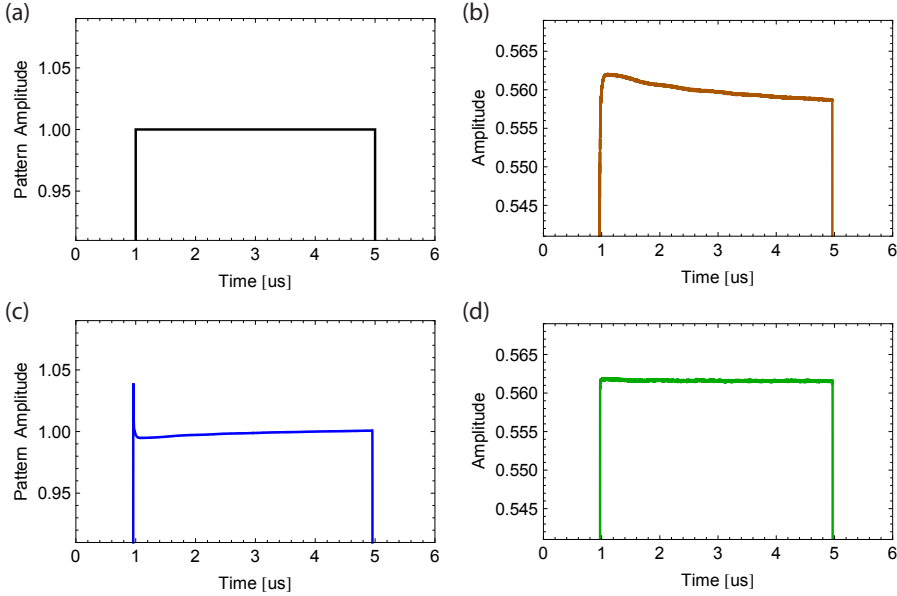
Figure 5.3: (a) Square pulse pattern as initially loaded into the AWG. (b) Measured response of the square pattern taken on a *LeCroy WavePro 7000A* oscilloscope. (c) Calculated corrected pulse pattern as loaded into the AWG. (d) Result of the correction measured on the oscilloscope.

calculated by

$$f_{corr} = FFT^{-1}\left[\left(\frac{FFT(f_{resp})}{FFT(f_{ideal})}\right)^{-1} FFT(f_{ideal})\right] \tag{5.7}$$

where f_{resp} is the measured pulse and f_{ideal} is the desired square pulse. This already allows to correct most of the imperfections concerning the rising edge of the pulse or long term drifts. The latter ones are mainly due to temperature drifts of the AWG's output amplifier. As those drifts do not become apparent for short pulses, it is advantageous to measure the response to a Heaviside step function instead of a Dirac delta function. The effect of the warm correction is shown in figure 5.3(d), where the optimized pulse pattern was used as shown in 5.3(c), which was calculated by measuring the response 5.3(b) with respect to a simple square pulse

59

5.3(a). Nevertheless the optimization does not include pulse distortion that is caused by impedance mismatches on the chip nor possible screening currents, which might flow on the superconducting Nb ground plane. Also the overall system response might change once the cabling is cooled down to low temperature.

Therefore the next optimization step is to measure the flux pulse as effectively seen by the qubit. Here we use a pulsed spectroscopy method implemented in a bad cavity limit. This method is expected to work in the strong coupling regime as well. The time resolved resonator transmission amplitude $\langle a(t) \rangle$ is measured for different probe frequencies ω_p of a coherent tone with constant amplitude and phase inside a frequency window $I_\omega = [\omega_r - \Delta < \omega_p < \omega_r + \Delta]$, where ω_r is the resonator's center frequency. Δ is typically chosen such that $\Delta \sim \kappa$. While the transmission $\langle a(t) \rangle$ is recorded, the optimized warm pulse is injected through the qubit flux gate line, such that the unexcited ground state qubit is tuned somewhere into the frequency window I_ω, which brings the system out of its equilibrium. The response of this perturbation depends on the precise shape of the flux pulse. However it also depends on the resonator linewidth κ, the qubit-resonator coupling rate g and the bias frequency of the qubit ω_0. Therefore the obtained response does not directly reflect the pulse shape because the perturbation still involves some complicated dynamics of the system. A typical measured response, normalized to the response at $t = 0$, is shown in figure 5.4(a) for $g/2\pi=3.8\,\text{MHz}$, $\kappa/2\pi=43\,\text{MHz}$, $\omega_0/2\pi=8.2\,\text{GHz}$ and $\omega_r/2\pi=7.061\,\text{GHz}$. The dynamic response for a specific slice of frequency $\omega_p/2\pi=7.86\,\text{GHz}$ is shown in figure 5.4(b).

However, even though the flux pulse shape is not directly visible in the measurement, once the system parameters are known it is possible to calculate the expected ideal system response by using a simulation as shown in figure 5.4(c/d). The master equation used for the simulation is given by equation 2.43 and the Hamiltonian is of the standard Jaynes-Cummings type

$$\hat{H}(t) = \hbar\omega_r \hat{a}^\dagger \hat{a} + \frac{\hbar}{2}\omega_a(t)\hat{\sigma}_z + \hbar g(\hat{a}^\dagger \hat{\sigma}_- + \hat{\sigma}_+ \hat{a}) + \mathcal{E}(t)\left(a^\dagger e^{-it\omega} + ae^{it\omega}\right), \quad (5.8)$$

except that we have now included a constant drive with amplitude $\mathcal{E}(t)$ and a time dependent qubit transition frequency $\omega_a(t)$. This implies that we cannot restrict the calculation to the steady state case to obtain ana-
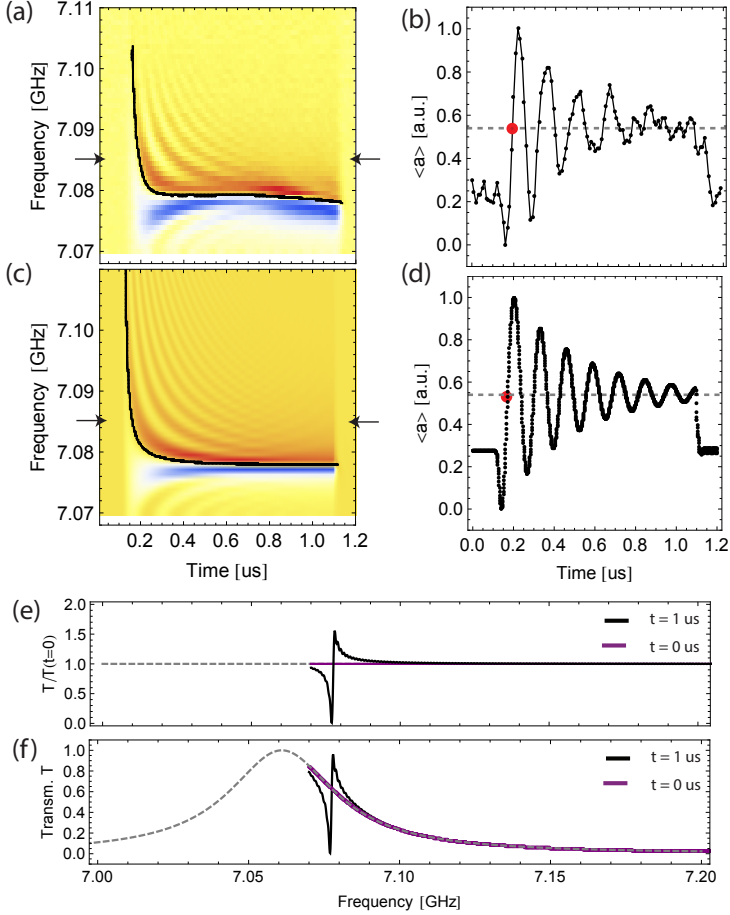
Figure 5.4: (a) Normalized measurement of the time resolved transmission amplitude $\langle a(t) \rangle$ while a ground state qubit is tuned into the spectroscopic region. (b) Cut for a frequency of $7.086\,\mathrm{GHz}$. The sudden presence of the qubit disturbs the steady state of the system and causes damped oscillations. (c/d) Numerical simulation of the response obtained from a master equation simulation. (e) Vertical cut of the transmission spectrum at times $0\,\mu\mathrm{s}$ and $1\,\mu\mathrm{s}$. If no qubit is present ($t = 0\,\mu\mathrm{s}$) the response is flat due to the normalization. (f) In the raw data (before normalization) the response will either reflect the uncoupled resonator at $t = 0\,\mu\mathrm{s}$ or include the characteristic dip caused by the qubit.

lytic results as done in chapter 4.1, implying the von Neumann differential equation has to be solved numerically.

By comparing the expected ideal system response to the measured one we are able to infer the corrections that will lead to an improved version of the effective flux pulse shape. For each frequency ω_p we therefore extract the point at which the dynamic response for the first time crosses a certain value, for example given by the steady state response to which the oscillation will have damped by the end of the flux pulse. The determination of this point in time is indicated in figure 5.4(a) and 5.4(b) by a red point for both the experimental and the numerical data. The damped response is shown in 5.4(e) where the close to steady state frequency slice $t = 1\,\mu\text{s}$ is normalized to a slice ($t = 0\,\mu\text{s}$) where no qubit is present. The two slices before normalization are shown in figure 5.4(f). Here the qubit is tuned to a frequency ω_1, which if $\omega_1 = \omega_r$ could well fit to the spectra explained in chapter 4.1 or in the case of $\omega_1 \neq \omega_r$ to a more general expression.

If the applied flux pulse was a perfect square pulse experiment and numerics should coincide. To better judge the difference the extracted points are renormalized on the frequency scale. Therefore we first translate the frequency ω into a flux $\phi(\omega)$ by using equation 2.7 and then set $\phi(\omega_0)\widehat{=}0$ and $\phi(\omega_1)\widehat{=}1$. The result is shown in figure 5.5(a). The noticeable mismatch indicates that the flux pulse shape as seen by the qubit is not ideal.

Finally we can use the difference to calculate a correction similar to what was done for the *warm* correction. In fact we may regard the observed trace as the real flux pulse shape additionally filtered to f_{JCD} by the Jaynes-Cummings dynamics of the system. We then calculate a correction by

$$f_{Corr} = FFT^{-1} \left[\left(\frac{FFT(f_{JCD}) * FFT(f_{Setup})}{FFT(f_{JCD}) * FFT(f_{Ideal})} \right)^{-1} FFT(f_{Applied}) \right]. \quad (5.9)$$

The advantage of this method is clearly seen as the system dynamics cancels out. The substitution of the system dynamics by a simple linear filter, is legitimate as long as the response is expected to have a purely classical origin, i.e. no quantum nonlinearities are considered. As long as the probe power is low, the resonator and the qubit act as two coupled harmonic oscillators and therefore this condition is well met. The calculated optimized pulse for the data of figure 5.5(a) is shown in figure 5.5(b).

This pulse still does not represent the final result of the optimization. In the bad cavity limit we are only able to experimentally observe the
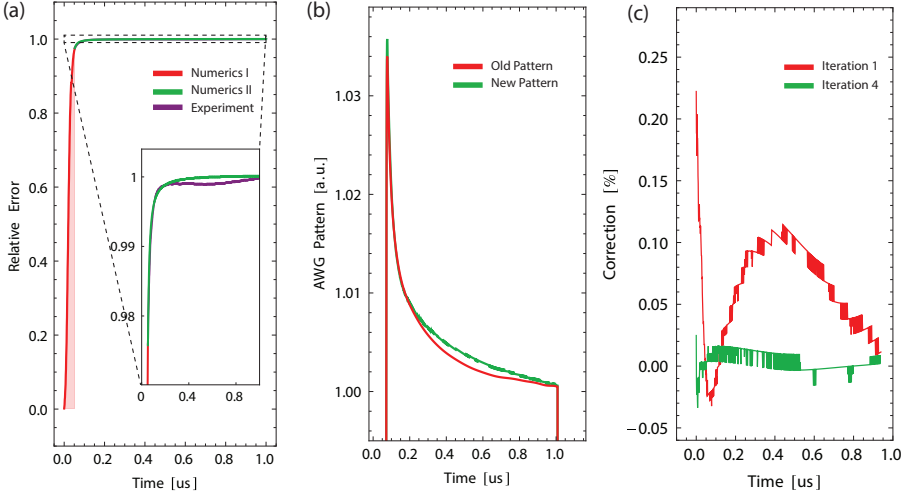
Figure 5.5: (a) Relative difference between the measured and the simulated response inferred from the fitted black line in figure 5.4. The red part shows the part of the trace for which no experimental data could be obtained. (b) Corrected pulse pattern (green) in comparison to the uncorrected one (red). Residual correction after the first and the fourth iteration of the optimization procedure. The sharp steps reflect the discretization of the frequency sweep and correspond to 100 kHz.

pulse response inside the frequency window I because the signal is strongly attenuated once ω_p is outside the resonator's bandwidth. Therefore we assume that the response outside this window coincides with the numerical response (see red line in figure 5.5(a)). The fact that the full response of the pulse is not accessible means that it is not possible to get a perfectly optimized pulse out of one dataset but a number of iterations are required. The reason why this strategy then in the end proved to be successful relies on the fact that any imperfection at the early part of the pulse leads also to a slight mismatch in the observable part of the pulse, provided it has already been freed from imperfections during previous iteration steps.

After four iterations the mismatch between experiment and numerics has been reduced by one order of magnitude with respect to the *warm* optimization procedure (see figure 5.5(b)). The presented method is limited

by the resolution of the probe frequency ω_p and by the bandwidth of the detection setup. For the presented case those values were 100 kHz and 10 ns. Therefore using a higher detection bandwidth would allow to optimize the pulse shape not only for pulses of a length $\sim$1 µs but also for pulses in the order of 100 ns.

As mentioned before, the method is also expected to work in the strong coupling regime, even without the need of iterating the measurement. The same measurement can be used and the dispersive shift would be recorded while the qubit is pulsed to some intermediate frequency between its bias point and the resonator.

5.4 Dynamic Qubit-resonator interaction

5.4.1 Coherent exchange of excitations: Strong coupling limit

The ability to prepare or analyze the state of our qubit allows us to study how specific states evolve while interacting with a single mode of the resonator once in or close to resonance. This atom-field interaction became already apparent in spectroscopy-like measurement, but directly resolving the dynamics will give the quantum nature of this fascinating interplay between matter and light further prominence. A main feature of strong coupling cavity quantum electrodynamics is the exchange of excitation between the qubit and the cavity, which is either revealed by sideband oscillations, first observed in circuit QED by [Chiorescu04] or by *vacuum Rabi oscillations* in the resonant case [Hofheinz08]. This oscillations are the time domain equivalent to the vacuum Rabi splitting occurring in the frequency domain measurements of chapter 4. If the system is first prepared in the separable state $|0\rangle \otimes |e\rangle$, meaning the resonator is initially empty and the qubit is excited, then as soon as the Jaynes-Cummings interaction is turned on, the excitation of the two systems coherently oscillates with the vacuum Rabi oscillation frequency $\Omega_R = \sqrt{(2g)^2 + \Delta^2}$, where $\Delta = \omega_a - \omega_r$ is the detuning between qubit and resonator. As long as the coupling g dominates over the dissipative terms κ and γ_1 the population of the cavity P_a respectively the qubit P_r for the resonant case $\Delta = 0$ can be simplified to

$$P_a(t) = \cos^2(\Omega_R t) \tag{5.10}$$
$$P_a(t) = \sin^2(\Omega_R t). \tag{5.11}$$
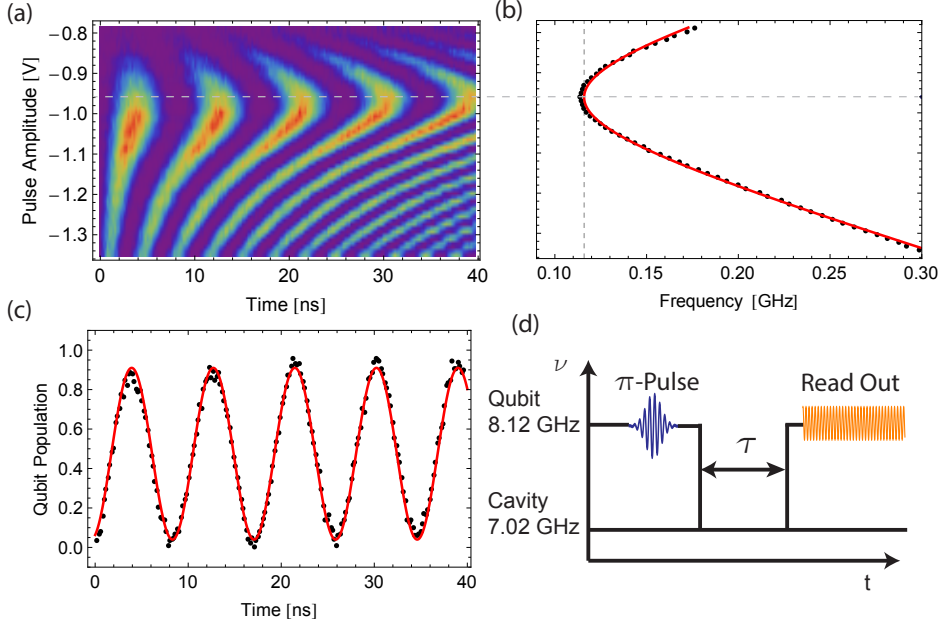
Figure 5.6: (a) Vacuum Rabi oscillation for different qubit-resonator detuning. (b) Fit (red) of the extracted oscillation frequency (black) to a square root function. (c) Qubit population for zero qubit-resonator detuning (black) and fit to a sinusoidal function (red). (d) Experimental pulse scheme used to obtain the data.

The initial state preparation takes place in a regime where the cavity and the qubit do not hybridize, $\Delta \gg g$. Just after the initialization the Jaynes-Cummings interaction is switched on for a time τ by tuning the qubit with a flux pulse in a regime where $\Delta \sim g$. Once the qubit is back at its bias frequency a dispersive read out can be performed by injection of a coherent read out tone (see figure 5.6(d)). The vacuum Rabi oscillation is shown in figure 5.6(a) versus detuning Δ, where the oscillation frequency was extracted by a fit to equation 5.11. As can be seen in figure 5.6(b) the oscillation frequencies agree well to a square root like dependence. The lowest frequency is obtained when the qubit and the resonator are on resonance, i.e. $\Delta = 0$ and it was extracted to be $g/2\pi=54.4\,\mathrm{MHz}$ (see figure

5.6(c)), which is compatible with the spectroscopically obtained value of $g/2\pi$=52.7 MHz. The slight tilt of the oscillation is due to finite risetimes of the flux pulse limited by the AWG and the filters that have been installed at the base plate of the cryostat.

5.4.2 Dissipative Resonant Dynamics

A more detailed treatment of the resonant interaction will also take care of dissipative terms. For the strong coupling limit the dynamics is mostly dominated by the coupling g. However in the bad cavity limit, where $\kappa \ll g$, dissipative terms play a prominent role. To better understand the crossover between those two regimes and to have analytic formulas at hand able to describe the resonant dynamics for various dissipative configurations, we have derived the time evolution of the operators σ_z and $a^\dagger a$ for the vacuum Rabi oscillation in the resonant limit. It is important to note that the initial state of this oscillation is normally $|0\rangle \otimes |e\rangle$, meaning that the system does not carry any phase information that might get lost during the evolution. We therefore only include the qubit dissipation γ_1 in the analytic treatment and disregard γ_φ. We once more use the von Neumann equation (2.43) to calculate H_{int} (equation 2.27) to find the state of the qubit and the resonator at time t assuming the initial condition $|0\rangle \otimes |e\rangle$. Whereas the qubit population is given by a lengthy expression [**?**] it is possible to find a compact formula for the resonator population

$$P_{res} = \frac{8g^2 e^{-\frac{1}{2}t(\gamma_1+\kappa)}\left(1 - \cosh\left(\frac{1}{2}t\sqrt{(\kappa-\gamma_1)^2 - 16g^2}\right)\right)}{16g^2 - (\gamma_1 - \kappa)^2}. \qquad (5.12)$$

The resonator population is plotted in the strong and the bad cavity limit in figure 5.7, where g and κ where fixed to the spectroscopic value and only γ_1, a time offset and a scaling factor where used as free fit parameters. Both data sets were taken without parametric amplifier. The fact, that the pulse sequence used to extract the cavity population in the strong coupling limit requires to repeat the experiment for each different setting of τ prohibited us to measure the oscillation for times, long enough to see the influence of any of the dissipative terms κ or γ_1. However the crossover from a coherent oscillation to an overdamped interaction is clearly visible. Even though the cavity dissipation κ clearly influences the dynamics. Also here the influence
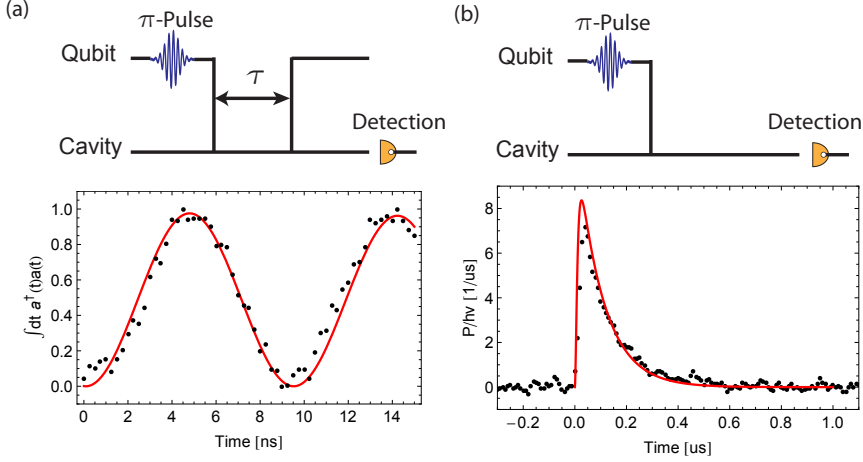
Figure 5.7: (a) Cavity population during a resonant vacuum Rabi oscillation in the strong coupling limit. The interaction was switched on for a time τ and the area underneath the emitted signal was integrated and renormalized. (b) Emitted power for a resonant interaction in the bad cavity limit. The emitted data was directly recorded by a single preparation in a time-resolved measurement.

of γ_1 is hardly visible as $g \gg \gamma_1$ and the dynamics is mostly influenced by κ and g.

In addition to the general expression of equation 5.12 we can further approximate the analytic solution in the two regimes. In the strong coupling regime, $g \gg \kappa, \gamma_1$, we get

$$\langle a^\dagger a \rangle (t) = \frac{8g^2 e^{-t(\gamma_1 + \kappa)/2} \left(1 - \cos \left(2gt \left(1 - \frac{(\kappa - \gamma_1)^2}{32g^2} \right) \right) \right)}{16g^2 - (\kappa - \gamma_1)^2} \tag{5.13}$$

and

$$\langle \sigma_z \rangle (t) = 2e^{-\frac{1}{2}t(\gamma_1 + \kappa)} \cos^2 \left(gt \left(1 - \frac{(\kappa - \gamma_1)^2}{32g^2} \right) \right) - 1, \tag{5.14}$$

which is the expression for an oscillation with frequency $2g$ damped with a rate of $(\kappa + \gamma_1)/2$. To obtain an expression for the bad cavity limit we

have to include further approximations by taking into account the fact, that terms $e^{-\kappa t}$ decay faster than all other exponential terms, such that for any time $t \gg 1/\kappa$ they can be omitted. In this limit we obtain an expression for the cavity population

$$\langle a^\dagger a \rangle (t) = \frac{4g^2 e^{t\left(-\gamma_1 - \frac{4g^2}{\kappa - \gamma_1}\right)}}{(\kappa - \gamma_1)^2 - 16g^2} \tag{5.15}$$

and the qubit population:

$$\langle \sigma_z \rangle (t) = \frac{2\left(8g^2 - (\kappa - \gamma_1)^2\right) e^{t\left(-\gamma_1 - \frac{4g^2}{\kappa - \gamma_1}\right)}}{16g^2 - (\gamma_1 - \kappa)^2} - 1. \tag{5.16}$$

The expressions show a purely exponential decay with the decay constant $\gamma_1 + (4g^2)/(\kappa - \gamma_1)$, which agrees width the linewidth of the narrow Lorentzian dip derived for the spectroscopic measurements (see section 4.1). This confirms that linewidths and decay constants constitute the same entity and only depended on whether measurements take place in the frequency or time domain. The purely exponential decay can also be derived by adiabatic elimination of the resonator's field mode [Delanty11], a more sophisticated method, which is useful when the collective dynamics of multiple emitters are treated (see chapter 7).

6
Collective Dynamics in the strong coupling limit

6.1 Collectively enhanced dynamics

Effects related to the interaction of light and matter can be investigated in many different physical systems. The description of this interaction can be simplified to the interplay of identical two-level systems and a single mode of an electromagnetic field. This theoretical abstraction is known as the Dicke- or Tavis-Cummings model [Dicke54, Tavis68]. In recent years it became feasible to investigate the complex interaction of light with multiple two-level systems as experiments approached a higher level of control over collections of individual quantum systems. The coupling strength (transition amplitude) of N two-level systems and a single mode increases as $\sqrt{N}$. Clear evidence of this nonlinear behavior was observed in spectroscopic measurement with few atoms [Bernardot92, Childs96, Thompson98, Münstermann00], large ensembles of atoms using cold gases [Brennecke07, Colombe07, Tuchman06], ion Coulomb crystals [Herskind09] and by using superconducting qubits coupled to a transmission line resonator [Fink09, Altomare10]. The investigation of these interactions has also gained additional momentum in the context of hybrid quantum systems, in which ensembles of microscopic systems, such as NV-centers are coupled to a single mode of a cavity [Kubo10, Wu10].

More insight into the dynamics of collective systems can be gained by time resolved measurements of energy exchange between its individual components. When multiple two-level systems are resonantly coupled to a single

mode, this process is called collective vacuum Rabi oscillations. The collective coupling strength *g* defines the frequency of these oscillations. Here, we restrict our investigation to the initial state in which the cavity is populated with exactly one photon [Mlynek12]. In this case the oscillation involves a single photon that is continuously absorbed and reemitted by all N two-level systems. In fact each two-level system absorbs the photon with equal probability 1/N. Our lack of knowledge about which two-level system actually absorbs the photon leads to entangled states which are known as W-states [Dür00]. The nonlinear enhancement of the coupling strength speeds up the generation of W-states when N is increased. In the context of quantum information processing such enhanced collective interaction rates may prove useful to generate multi-qubit entangled states on time scales $\propto 1/\sqrt{N}$. Alternatively, the generation of Dicke- and W-states has been explored in NMR [Teklemariam02], with photons [Eibl04], ions [Roos04] and superconducting circuits [Neeley10] using interactions not mediated by the resonant interaction with a cavity.

Here, using quantum state tomography, we demonstrate explicitly that the strong collective coupling mediated by the resonant interaction of *N* superconducting qubits with a single photon stored in a transmission line resonator generates W-type entangled states as predicted by the Dicke and Tavis-Cummings Hamiltonians [Dicke54, Tavis68]. This work builds on the prior spectroscopic [Fink09] and time resolved [Altomare10] observations of the $\sqrt{N}$ enhancement of the collective resonant interaction with the cavity. 3-qubit entangled states of the W- or GHZ-class have also been generated in superconducting circuits using sequential [DiCarlo10, Baur12b, Fedorov12] or collective schemes [Neeley10] based on physical interactions different from the one presented here.

In our time-domain studies of the collective oscillation we use full control over three transmon-type superconducting qubits [Koch07] coupled to a single electric field mode of a microwave resonator. The coupling of multiple two-level systems to a single mode is described by the Tavis-Cummings Hamiltonian [Tavis68] as discussed in 2.3.

6.2 Experimental setup

In our circuit QED implementation of the Hamiltonian $\hat{\mathcal{H}}_{\text{TC}}$ (see equation 2.30) we use the first harmonic mode of a coplanar transmission line resonator at $\omega_r/2\pi \simeq 7.023$ GHz with quality factor $Q \simeq 14800$. The resonator is used for the resonant exchange of a single excitation and for joint dispersive readout of the three qubits by measuring its transmission [Filipp09]. All qubits are located at antinodes of the first harmonic mode of the resonator. The frequency of each qubit is approximately given by $\hbar\omega_j(\Phi) \approx \sqrt{8E_C E_J(\phi)} - E_C$ where the Josephson energy depends periodically on the applied flux according to $E_J(\phi) = E_{Jmax}|\cos(\pi\phi/\phi_0)|$. The maximum Josephson energies $E_J(0)/\hbar$ for the three qubits are (26.8, 28.1, 25.7) GHz and their charging energies $E_C/\hbar$ are (459, 359, 358) MHz. The anharmonicity of the transmon energy levels depends on E_C and is chosen such that the validity of the two-level approximation is ensured while keeping the charge dispersion low. The maximum transition frequency of the qubits $\omega_j(0)/2\pi = (9.58, 8.65, 8.23)$ GHz is designed such that all three qubits can be tuned into resonance with the resonator at ω_r. In the steady state the qubits are flux biased at $\omega_j/2\pi \simeq (6.11, 4.97, 7.82)$ GHz using the quasistatic magnetic field generated by three superconducting miniature coils positioned underneath the chip, such that $|\Delta_j| \gg g_j$ with detuning $\Delta_j = \omega_j - \omega_r$. We measure qubit dephasing times $T_2 = (100, 140, 440)$ ns limited by flux noise far off the optimal bias point and qubit relaxation times $T_1 = (2.1, 1.8, 1.0)$ μs limited by unknown reasons other than the Purcell-effect. Tuning of the qubit transition frequencies on the nanosecond timescale is achieved by injecting current pulses into on-chip flux control lines. Both for the coils as well as for the flux gate lines we determined the full coupling matrix to compensate for cross-coupling at low frequencies. The coupling strengths g_j of the qubits (A,B,C) extracted from spectroscopic measurements are $(g_A, g_B, g_C)/\pi = (-105.4, 110.8, 111.6)$ MHz. The negative coupling constant of qubit A originates from the π-phase difference of the first harmonic mode between the center of the resonator and its coupling ports. By applying phase controlled truncated Gaussian DRAG pulses [Gambetta11b] through the on-chip charge bias lines each qubit can be prepared in an arbitrary superposition state $\psi = \alpha|g\rangle + \beta|e\rangle$. For the joint read-out all qubits are dispersively coupled to the resonator and its measured frequency-shift depends on the state of each individual qubit as
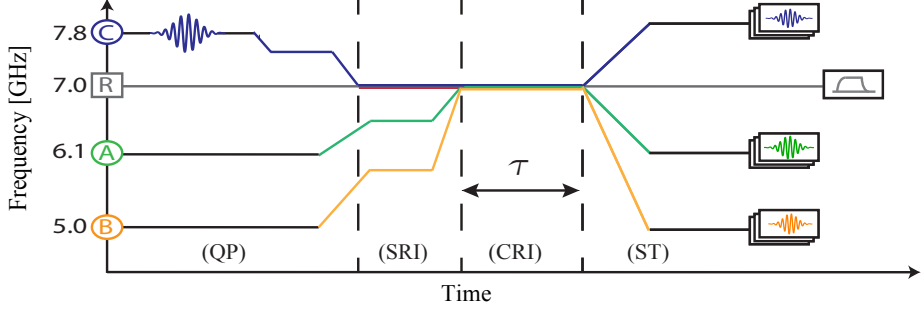
Figure 6.1: Pulse sequence for the single and collective vacuum Rabi oscillation (QP=Qubit Preparation, Buf=Buffer Level for Flux Pulses, SRI=Single Resonant Interaction, CRI=Collective Resonant Interaction, ST=State Tomography). Qubits not taking part in the collective interaction remain at their bias frequency (dashed green/blue). The duration τ of the collective interaction is varied.

$Tr(\hat{M}\rho)$, where $\hat{M}$ is the measurement operator and ρ is the density matrix to be determined [Filipp09] (see also section 3.3). To extract the 64 unknown elements of the density matrix we have applied 64 linearly independent measurement operators on the state to be characterized. These independent operators are constructed by applying a set of single qubit rotations, namely $\{Id, \ \sigma_x, \ \sigma_y, \ \sigma_z\}$ to the operator $\hat{M}$. To extract the population only, the number of linearly independent operators reduces to 8. The pulse sequence we have implemented to observe the single and collective vacuum Rabi oscillation is depicted in Fig. 6.1.

6.3 Observation of enhanced coherent collective dynamics

First, a π-pulse is applied to a single qubit far detuned from the resonator, such that the system can be described by a product state $|e\rangle \otimes |0\rangle$. Then the qubit is tuned into resonance with the resonator using a flux pulse of variable duration τ. To reduce the overshoot the qubit is first tuned to an intermediate buffer frequency. On resonance the energy eigenstates of

this system with $n = 1$ excitations and N qubits are $|n = 1, N = 1\pm\rangle = 1/\sqrt{2}(|g, 1\rangle \pm |e, 0\rangle)$ and the initial excited qubit state undergoes vacuum Rabi oscillations between $|g, 1\rangle$ and $|e, 0\rangle$. The frequency of the oscillations is given by $\Omega = 2\sqrt{g^2 + \Delta^2}$ with $\Omega_0 = 2g$ for $\Delta = 0$ (see section 5.4). The amplitude of the vacuum Rabi oscillation is maximal on resonance where the excitation is fully exchanged. After the resonant flux pulse of length τ the qubit is detuned from the resonator again and the energy exchange process is stopped.

In addition to performing a dispersive readout of the qubit population we determine the resonator population by measuring the average photon number, as given by the time integrated power $\langle \hat{a}^\dagger \hat{a} \rangle$ at the output of the cavity once the oscillation is stopped [Bozyigit11]. The qubit population is observed to oscillate with a frequency of 112.0 MHz, out of phase with the photon field oscillating at 111.2 MHz [Fig. 6.2(b, left)] and in good agreement with the spectroscopically obtained value.

We extended the procedure described above as shown in Fig. 6.2(a) to two and three qubits. An initial single photon Fock state is prepared by transferring the full excitation of the first qubit to the resonator by adjusting the interaction time between the qubit and the resonator to $\tau_0 = \pi/2g$. Then the second and third qubit are tuned into resonance and the resonant collective interaction proceeds for time τ. All qubit populations, obtained by tomographic state reconstruction for each interaction time τ, are observed to oscillate simultaneously out of phase with the cavity photon number. When the number N of qubits taking part in the resonant interaction is increased, the frequency of the oscillations is observed to scale with $\sqrt{N}$ and the amplitude of the individual qubit population decreases to 1/N fulfilling the normalization condition. The tripartite states between which the oscillations occur are $|g, g, 1\rangle$ and $1/\sqrt{2}(|g, e, 0\rangle - |e, g, 0\rangle)$ and equivalently $|g, g, g, 1\rangle$ and $1/\sqrt{3}(|g, g, e, 0\rangle + |g, e, g, 0\rangle - |e, g, g, 0\rangle)$ for the fourpartite state, where we have denoted the states in a binary order as $|C, B, A, Cavity\rangle$. The opposite phase of the $|e, g, g, 0\rangle$ state originates from the fact that qubit A has a negative coupling constant. The qubit populations measured after the collective vacuum oscillations are shown in Fig. 6.2(b/c, left column). The collective oscillation transfers energy back and forth between the qubits and the resonator, such that the population in the cavity is correlated with the population of the qubit $|ggg\rangle$ state. Hence it is instructive to measure the photonic part of the state as done
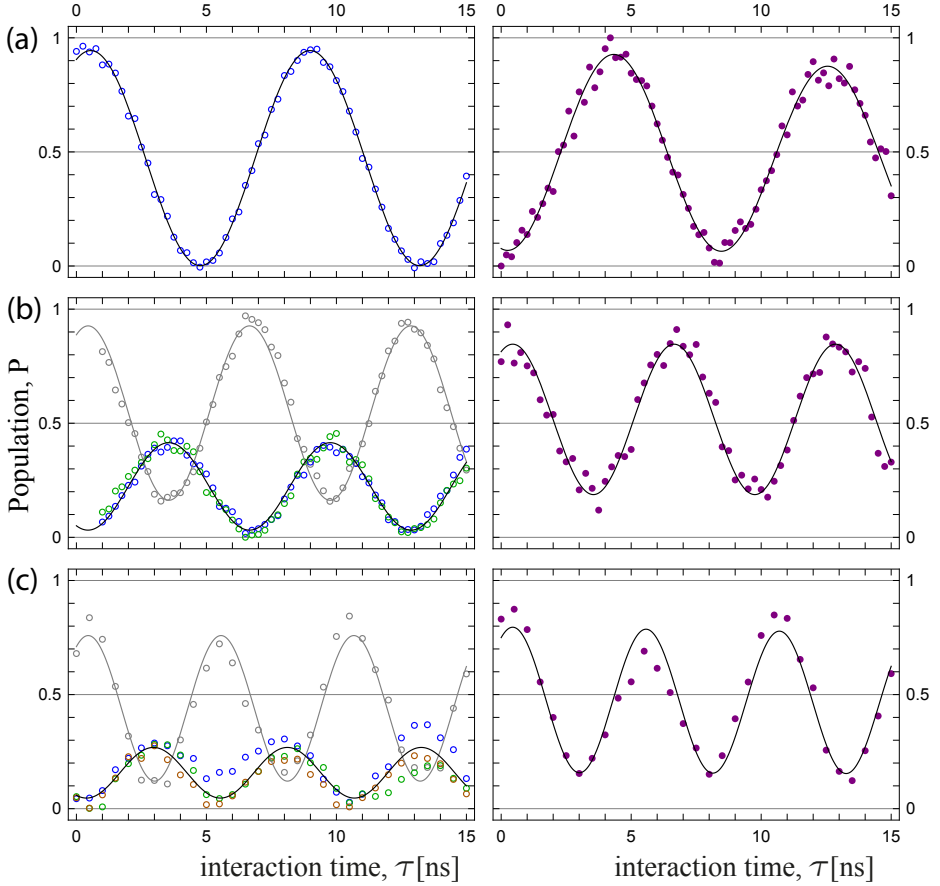
Figure 6.2: Oscillations for N=1 (a), N=2 (b) and N=3 (c). The population is shown for the excited states of qubit A (blue), B (green), C (orange), the $|ggg\rangle$ state (gray) and the resonator (violet).

before for the single qubit vacuum Rabi oscillations [Fig. 6.2(b/c, right column)]. The oscillation frequencies for the resonator population for N=2 and N=3 are 161.8 MHz $= 1.05 \cdot \sqrt{2} \, \bar{g}/2\pi$ and 195.2 MHz $= 1.03 \cdot \sqrt{3} \, \bar{g}/2\pi$, with $\bar{g}$ being the root mean square [López07] of the three spectroscopically obtained coupling constants. These oscillation frequencies clearly demon-

strate the $\sqrt{N}$-nonlinearity of the Tavis-Cummings Hamiltonian in time resolved measurements as illustrated in figure 6.5(b). While the collective qubit oscillations are in good agreement with the expected dynamics, we observe a decrease in visibility with increasing N for both the qubit and resonator populations. We attribute this effect to an imperfect control of the flux pulse amplitudes as no additional cold pulse optimization was performed as for example outlined in section 5.3. Although we have extracted a flux pulse cross coupling matrix at low frequencies, its accuracy is not sufficient to fully compensate the flux cross talk also at high frequencies and to exactly tune all qubits into resonance with the resonator simultaneously.

6.4 Demonstration of W-type entanglement of Dicke-States

During the collective oscillations a W-state is created at time $\tau_W = \pi/(2\overline{g}\sqrt{N})$, i.e. when the cavity state factorizes $|0\rangle \otimes 1/\sqrt{3}(|g,g,e\rangle + |g,e,g\rangle - |e,g,g\rangle)$. We measured the three qubit density matrix at this time by applying full quantum state tomography [Filipp09]. Figure 6.4 shows (a) the real part of the density matrix and (b) the corresponding Pauli sets.

The collective interaction time needed to create this three qubit entangled state was only $\tau_W = 2.9\,\mathrm{ns}$, while the overall sequence duration from the start of the excitation pulse to the end of the flux pulses was $24.4\,\mathrm{ns}$ as limited by technical constraints.

As needed the dynamic phase that is picked up during the time when the qubits are detuned can be corrected by applying single qubit phase gates or by adjusting the phases of the tomography pulses. Here the coherent entries of the density matrix have been numerically rotated to correspond to the phases in the expected state.

We have also characterized the measured state fidelity defined as $\langle\rho_t|\,\rho\,|\rho_t\rangle$ with respect to the density matrix rotated into the appropriate basis. We use a maximum likelihood method which assumes that the measurement outcomes are subject to Gaussian noise. To find the most probable physical quantum state consistent with the obtained result the problem is mapped to a least square minimization by an appropriate change of the operator basis [Smolin12]. Using this method the number of steps needed to perform the maximum likelihood algorithm scales as $O(d^4)$, where d is the
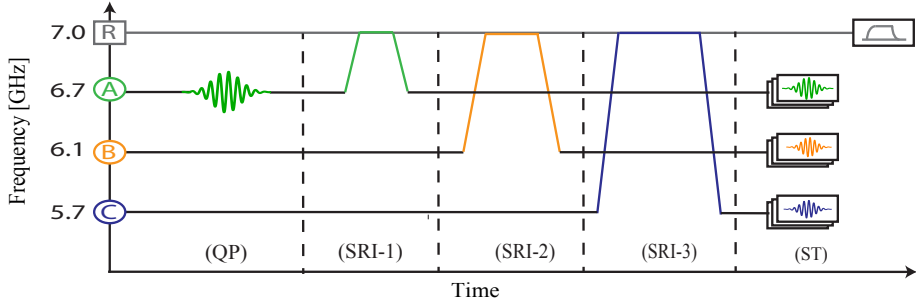
Figure 6.3: Sequential generation of a W-state. One Qubit is prepared in its excited state (QP). All qubits are tuned one after another on resonance until the initial excitation is equally shared (SRI 1-3). Once all qubits are tuned back to their bias frequency state tomography is performed (ST).

dimension of the quantum state. The resulting fidelity is $78\,\%$ with respect to the density matrix $\rho_t = |\Psi_W\rangle\langle\Psi_W|$ of the ideal state $\Psi_W = 1/\sqrt{3}(|g,g,e\rangle + |g,e,g\rangle - |e,g,g\rangle)$, limited predominantly by flux cross talk as discussed before in the context of time resolved measurements. In addition, via convex roof extension we have found the three-tangle to be close to zero (0.06), verifying that the prepared state belongs to the W-class rather then to the GHZ-class [Cao10]. Using the entanglement witness operator $\hat{M} = 2/3\,Id - |W\rangle\langle W|$ we find that $Tr(\hat{M}\rho) = 2/3 - \mathcal{F} = -0.12 < 0$ allows to discriminate our tripartite entangled pure state against any bipartite entangled states [Gühne09]. We note that, in the time resolved measurements the total measurement time per data point is determined by the $2.5\,10^5$ averages per population measurement at a repetition rate of $50\,\text{kHz}$. At the same rate each state preparation and subsequent measurement was repeated $6.5\,10^5$ times to obtain the density matrix and 10^7 times to obtain the cavity population.

To experimentally verify that the fidelity of a W-state generated by the collective interaction with a cavity mode in this device is not limited by coherence we have also prepared a W-state using a novel sequential method. In this approach we distribute a single excitation equally between the three qubits using resonant interaction (see figure 6.3). First, we excite qubit C and tune it into resonance with the resonator for time

Figure 6.4: (Color online) Real part of the density matrix of the W-state. (a) Obtained for the collective approach as shown in Fig. 6.2. (c) Generated by the sequential approach. (b/d) Pauli set for the collective/sequential approach.

$\tau_1 = \arcsin\left(\sqrt{2/3}\right)/g_C$. During this interaction, 2/3 of the excitation is transferred to the resonator. Next we tune qubit B into resonance for
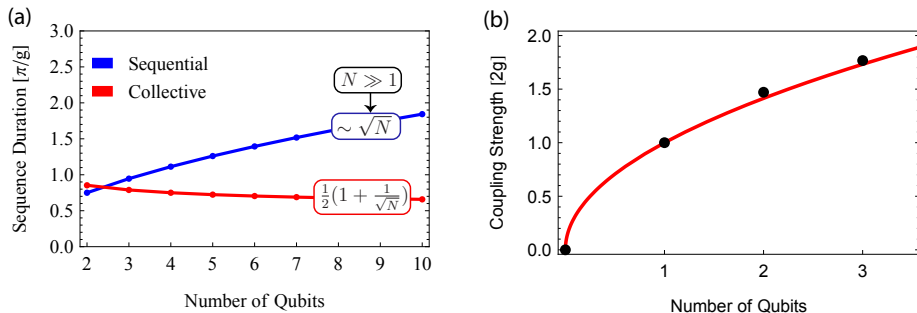
Figure 6.5: (a) Sequence duration for the W-state generation in dependence of the number of qubits. The collective approach (blue) is compared to a sequential one (red).(b) Experimentally obtained coupling strengths (black points) fitted by a square root dependence (red solid line).

a time $\tau_2 = \arcsin(\sqrt{1/2})/g_B$, transferring half of the resonator excitation to qubit B. Finally we let qubit A pick up the remaining third of the energy from the resonator by bringing it into resonance for a time $\tau_3 = \arcsin(1)/g_A$. The overall sequence duration from the start of the excitation pulse to the end of the flux pulses is 26.7 ns, much longer than τ_W but similar to the total pulse sequence length used for the collective resonant interaction. Using a joint high-power readout (see section 3.3) for tomography we obtain a density matrix of the W-state with much higher fidelity 91%, shown in figure 6.4(c/d). As expected the preparation time for the sequential method is longer than for the collective approach, because the latter method exploits the $\sqrt{N}$-enhancement. The dependence of the W-state's preparation time in dependence of the number of qubits is compared for the two approaches in figure 6.5. The fact that the higher fidelity was obtained by a procedure where no simultaneous flux pulses are applied to multiple qubits affirms that the main limitation of the collective generation is due to residual flux crosstalk, which could be eliminated in future experiments, rather than decoherence. Moreover we estimated the influence of dissipation and dephasing in absence of all systematic errors to obtain a theoretical upper limit of 93% for the sequential and 97% for the collective state preparation.

In summary, in a cavity QED experiment, we have studied the collective interaction of up to three superconducting qubits with a single photon stored in a microwave resonator. We have explicitly reconstructed the density matrix of the multi-qubit entangled state of the Dicke- or W-type with fidelities considerably higher than 2/3. We have also resolved the temporal dynamics of the population in the time domain characterized by the $\sqrt{N}$-scaling of the collective vacuum Rabi oscillation frequency in both the qubit and the photon states.

<div style="text-align: right">

7

</div>

Collective dynamics in the lossy cavity limit

7.1 Review of superradiance experiments

Since 1954, enhanced superradiant decay has been observed in many different physical systems [Skribanowitz73, Gross76, Raimond82, Scheibner07, Rohlsberger10]. The obtained results are consistent with Dicke's prediction that the emitted power of large ensembles depends on the square of the density of the emitters rather than showing a linear dependence (see figure 7.1). However, for large numbers of atoms or atom-like systems a direct observation of superradiance may be hindered by numerous impeding effects, such as nonlinear propagation and diffraction which occur in dense ensembles [Gross82].

Striving to realize ideal conditions for its observation, a number of experiments were designed to explore the microscopic regime of superradiance by employing a small number of two-level emitters [DeVoe96, Eschner01, Filipp11, vanLoo13]. In particular experiments involving two trapped ions were able to show that their collective decay rate varied by a few percent depending on their separation [DeVoe96, Eschner01]. These experiments presented clear evidence of an enhanced decay, but were unable to resolve the dynamics by directly measuring the intensity of the emitted radiation as a function of time. Although the ions could be driven directly into either sub- or superradiant states, arbitrary initial states could not be directly prepared. In addition, the observed superradiant decay did not dominate over other decay mechanisms, because of the too large distance R between
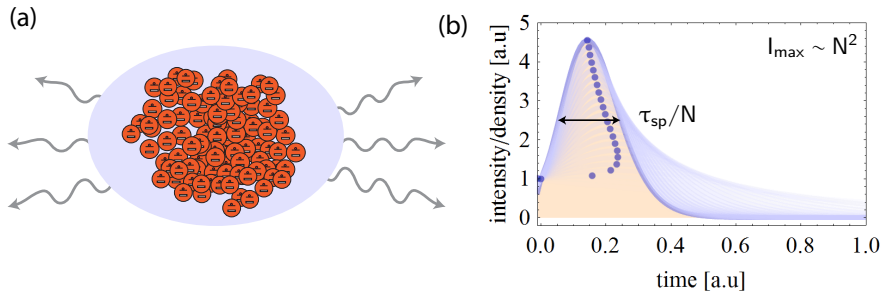
Figure 7.1: (a) Regime of large ensemble superradiance. The population of N emitters confined inside a volume V (light blue area) of the system is fully inverted.(b) Time dependence of the decay. The number of emitters is varied from $N = 1$ to $N = 22$.

the emitters exceeding the wavelength λ of the emitted radiation.

In the quickly developing field of circuit quantum electrodynamics, in which artificial atoms realized as superconducting qubits are coupled to microwave photons [Schoelkopf08], the condition $R \sim \lambda$ or even $\ll \lambda$ is realized. Moreover experiments take advantage of the fact that emitters can be localized in a one-dimensional (1D) architecture instead of in three dimensions (3D). In particular, for 1D superconducting transmission lines single microwave photons can propagate with small loss in forward or backward direction while strong interactions can be maintained over larger distances [vanLoo13, Lalumière13]. As a consequence, in circuit QED experiments, super- and subradiant states have been selectively prepared in the strong coupling regime of cavity QED [Filipp11] as well as in 1D free space [vanLoo13]. The yet largely unexplored bad (or fast) cavity limit [Haroche06], where the cavity decay rate κ is much larger than the coupling strength g and the rates for non-radiative atomic decay Γ_{nr} and pure dephasing Γ^* ($\kappa \gg g \gg \Gamma_{\mathrm{nr}}, \Gamma^*$) extends between those two regimes.

7.2 Experimental setup and characterization

We have investigated superradiance of a pair of emitters in the bad cavity limit of circuit QED [Mlynek14] as also discussed theoretically in [Bonifa-
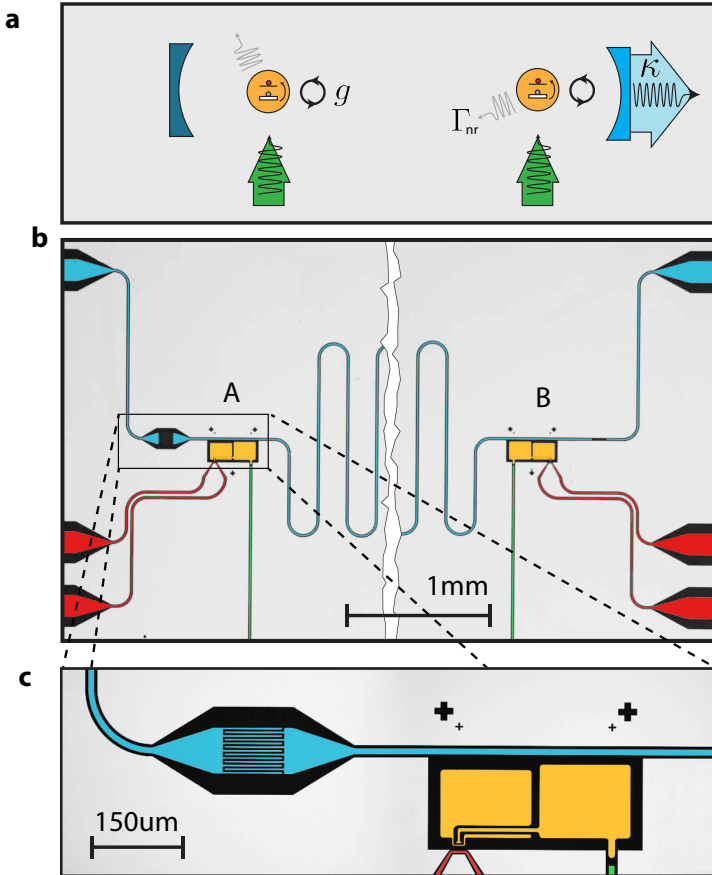
Figure 7.2: Schematic and Sample. **a**, Optical equivalent of the setup. Two two-level systems (yellow) are coupled with identical rate g and intrinsic decoherence rate Γ_{nr} to a cavity mode with photon decay rate κ (blue). The two-level systems are excited by radiation applied orthogonal to the cavity mode (green). **b,c**, Optical microscope false color image of the sample with two qubits (A,B) (yellow) capacitively coupled to an asymmetric waveguide resonator (blue). Each qubit is equipped with a local charge gate (green) and a flux bias line (red) to create initial states and tune transition frequencies independently.

cio71, Lehmberg70, Delanty11] (Fig. 7.2) with two transmon qubits coupled to a single coplanar waveguide resonator with parameters $\Gamma_1/2\pi(A, B) \approx$ (0.09 MHz, 0.12 MHz), $\Gamma^*/2\pi(A, B) \approx$ (0.008 MHz, 0.076 MHz), $g/2\pi(A, B)$ $\approx$ (3.5 MHz, 3.7 MHz), and $\kappa/2\pi \approx 43$ MHz. Here, the measured Γ_1 is the sum of the negligible small radiative Purcell decay rate at the bias frequency $\Gamma_\kappa(\omega_{A,0}, \omega_{B,0})/2\pi$ = (0.0004, 0.005) MHz into the cavity mode at the detuning $\Delta/2\pi$ = (1140, 340) MHz between the qubit and the cavity and the dominating non-radiative decay rate $\Gamma_{\mathrm{nr}} \sim \Gamma_1$, which we chose to include all other decay channels.

The sample was fabricated in two-dimensional geometry using standard techniques. The resonator is weakly coupled to an input and overcoupled to an output line resulting in large decay rate. A smaller than typical coupling rate g was realized by creating a qubit geometry in which island and reservoir couple almost identically to the resonator (see section 2.3). The qubits were positioned at field maxima of the first harmonic mode of the resonator.

The qubit coherence properties at their idle positions $\omega_{A,0}$ and $\omega_{B,0}$ have been extracted as $1/\Gamma_1(A, B)$=(1.7 μs, 1.3 μs) and $1/\Gamma_2(A, B)$=(2.9 μs, 1.2 μs) by standard Rabi and Ramsey pulse sequences. The final state was evaluated by measuring the qubit fluorescence when tuning it into resonance with the cavity (see section 3.3).

For a further characterization of the system properties we have measured the average transmittance of the cavity with the transition frequency ω_A of qubit A tuned to the center frequency of the resonator $\omega_r/2\pi \approx 7.064$ GHz while the second qubit B is kept off-resonant at $\omega_{B,0} \approx 7.41$ GHz. The measured transmission spectrum is plotted *vs.* the frequency ω_p of a weak external probe field as shown for this sample in figure 4.1 of section 4.1.

7.3 Time dependent dynamics

In a next step, we have explored the Purcell-enhanced spontaneous decay of the individual qubits. For this purpose the qubits were prepared in their excited state $|e\rangle$ by applying a π-pulse through a separate gate line (green in Fig. 7.2) and tuned into resonance with the cavity by applying a magnetic field pulse using a dedicated flux line (red in Fig. 7.2).

The pulse scheme used for individual control and read out of the qubits is

similar to the one used for observing collective dynamics in strong coupling circuit QED (see figure 6.1). In their idle position, both qubits are tuned to their maximum transition frequencies of $\omega_{A,0} \approx 8.20\,\text{GHz}$ and $\omega_{B,0} \approx 7.40\,\text{GHz}$ by using miniature superconducting coils mounted on the backside of the chip which allow for individual flux biasing of the qubit SQUID loops. Single-qubit operations are realized using 12 ns long resonant microwave pulses. Qubit transition frequencies were tuned on ns timescales by injecting current pulses into the flux gate line (Fig. 7.2).

To measure the field we used a heterodyne setup which measures the complex amplitude $S(t) = a + h^\dagger$, consisting of the experimental signal plus amplifier noise dominated by a high-electron-mobility transistor amplifier used to amplify the signal by 30 dB at 4 K. Additional amplification is done at room temperature by 60 dB. The microwave signal is then mixed down to 25 MHz, again amplified by 30 dB, digitized using an analogue to digital converter at a time resolution of 10 ns and finally processed in real time with field programmable gate array (FPGA) electronics, which also digitally converts the signal down to DC and uses a 4 points square filter to get rid of frequency components at more than 25 MHz. To extract the photon number the FPGA calculates $S^\dagger S$ in real time and then averages over multiple instances of the same experiment leading to $\langle S^\dagger S \rangle = \langle a^\dagger a \rangle + \langle h h^\dagger \rangle$ assuming that the noise and the signal are uncorrelated. The noise floor is determined from an off-measurement where no photons are generated and can be numerically subtracted (see also section 3.3).

In the limit $\kappa \gg g \gg \Gamma_{\text{nr}}$, the single excited qubit shows exponential decay of the detected power P (Fig. 7.3a) with a rate of $\Gamma_\kappa = \kappa g^2/|\frac{\kappa}{2} + i\Delta_r|^2$ [Delanty11, Heinzen87, Carmichael08]. To slow down the qubit decay with respect to the bandwidth of our acquisition system we have performed the measurements at a small qubit/cavity detuning of $\Delta_r/2\pi = (\omega_{A/B} - \omega_r)/2\pi = 25\,\text{MHz}$. The time dependence of the individual qubit decays are very similar with differences limited only by a small spread in individual coupling rates g. By numerically fitting the master equation simulation to the individual decays we may extract the non-radiative decay rates once the qubits are tuned into resonance, given by $\Gamma_{\text{nr}}(\Delta = 25\,\text{MHz.})/2\pi = (0.040, 0.042)\,\text{MHz}$. This rates are small to the radiative decay rates of $\Gamma_\kappa(\Delta = 25\,\text{MHz.})/2\pi = (0.48, 0.54)\,\text{MHz}$. The deviation of the power $\Delta P(t) = P_0\,e^{-\Gamma_\kappa^{\text{A,B}}t} - \bar{P}(t)$ emitted from the individual emitters

from their mean $\bar{P}$ is plotted versus t in the upper panel of Fig. 7.3a. The normalization is given by $P_0 = \hbar\omega\Gamma_\kappa$. These data sets serve as a reference for comparison with the superradiant decay of two qubits. When both qubits are prepared in the state $|ee\rangle$ and tuned synchronously into resonance with the resonator we observe the characteristic collective superradiant decay of the two-qubit ensemble [Gross82, Delanty11]. First we note that the emitted power level is approximately twice as large as in the single qubit case (Fig. 7.3b) with an enhancement of the power level relative to the single qubit case at early times and a reduction at later times, which is also displayed in the upper panel of Fig. 7.3b. In addition we note that the two-qubit collective decay begins at a rate smaller but then speeds up to values larger than the single qubit decay rate. Both features are qualitatively expected for small ensemble superradiance and are also in quantitative agreement with a master equation simulation taking into account the measured qubit relaxation and dephasing rates (blue line) and an analytic approximation $\Delta P(t) = 2P_0\, \mathrm{e}^{-2\bar{\Gamma}_\kappa t}(1 + 2\bar{\Gamma}_\kappa t) - 2\bar{P}(t)$ (black line) [Gross82]. Intuitively, the decay process starting out at a small rate and speeding up can be understood as due to the qubits dipoles with initially undefined phase synchronizing during the decay through their interaction, which gives rise to correlations. The correlations are naturally linked to the presence of entanglement, as the only allowed decay channel for the $|ee\rangle$ state is to cascade down to $|gg\rangle$ via the entangled bright state $|B\rangle = |ge\rangle + |eg\rangle$ (see figure 7.4a). The transition matrix element from $|B\rangle$ to $|gg\rangle$ is twice enhanced compared to a simple one qubit decay from $|ge\rangle$ to $|gg\rangle$ (see figure 7.4b). However both $|B\rangle$ and $|ge\rangle$ contain the same number of excitations. It is therefore apparent that the superradiant decay cannot follow a purely exponential dependence as the decay rate is not always proportional to the number of excitations, i.e. $dN/dt \not\propto N$ This intuitive argument can also be verified experimentally by initially preparing the two qubits in superposition states $(|g\rangle + \exp^{i\varphi_{A,B}}|e\rangle)/\sqrt{2}$ with well defined phases. If the relative phase of the dipoles $\Delta\varphi = \varphi_A - \varphi_B$ is adjusted to 0, initially, the superradiant decay occurs at a single enhanced rate much earlier (Fig. 7.3c), as the initial state, written in the coupled basis, already contains a $|B\rangle$ state part and thus is provided with correlations right away. Also in this case the observed decay dynamics are in good agreement with theory $\Delta P(t) = P_0\, \mathrm{e}^{-2\bar{\Gamma}_\kappa t}(\frac{3}{2} + \bar{\Gamma}_\kappa t) - \bar{P}(t)$ (black lines) and master equation
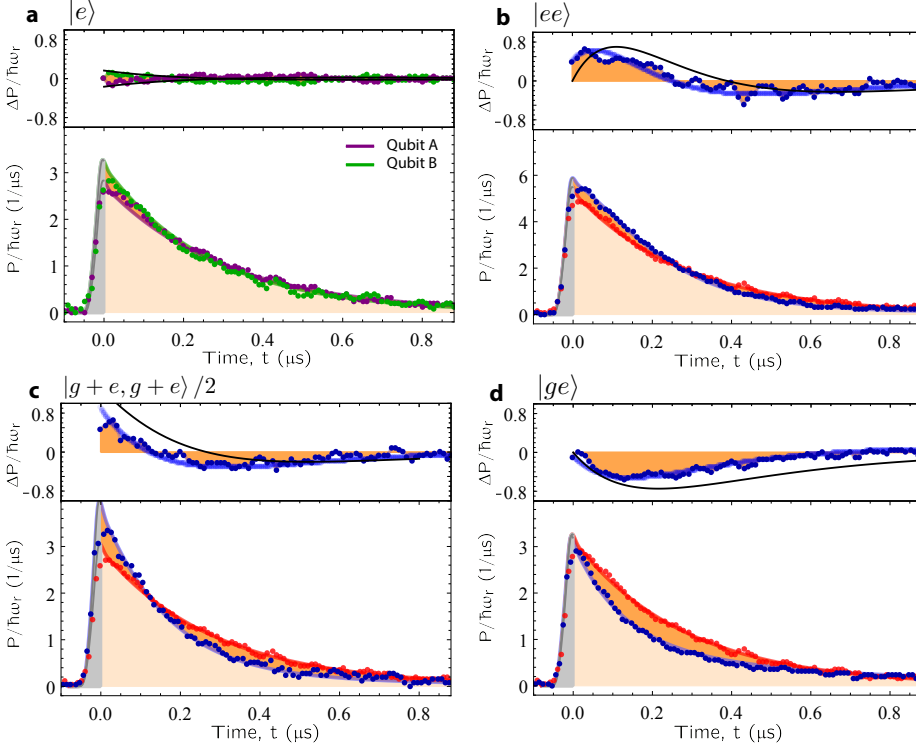
Figure 7.3: Spontaneous emission and two-qubit superradiance for the indicated initial states. In each panel the time dependence of the emitted power P for a given initial state (bottom) and the deviation from the average single qubit power ΔP (top) is shown. Data (dots) is compared to a simple rate equation model (solid black lines) and full master equation simulations (solid blue lines), see text for details. **a**, Individual decay of qubit A (purple) or B (green) prepared in state $|e\rangle$. Collective decay for initial states **b** $|ee\rangle$, **c** $(|g\rangle + |e\rangle)(|g\rangle + |e\rangle)/2$, and **d** $|ge\rangle$. The orange area indicates the difference of the collective two-qubit decay with respect to the mean individual decay (dashed red line). For time $t < 0$ (greyed-out area), the emission dynamics is governed by the initial field build-up, which is not considered in the upper parts of each panel. All data was normalized by the the same constant, extracted by matching the emitted energy of the mean individual decay to what is expected from the master equation. The theoretical curves then are scaled by s to include variations in our detection efficiency, where in (b) s=0.9, in (c) s=0.94 and in (d) s=1.07. The reference curve of the mean individual decay was scaled accordingly.

(a)

(b)
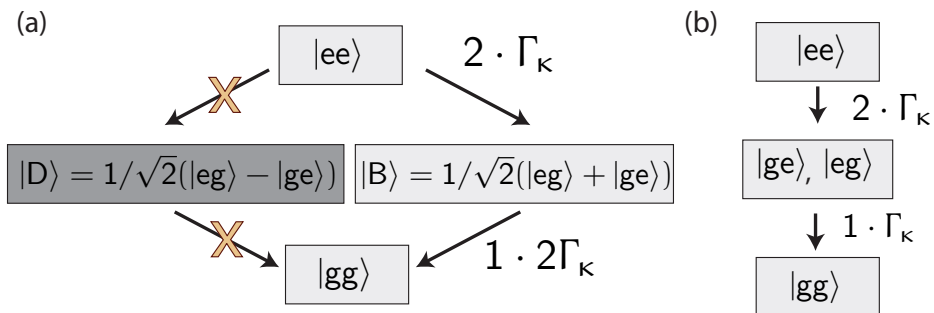
Figure 7.4: Two qubit level scheme and decay channels. (a) Eigenstates in the coupled basis. All allowed transitions happen via the bright state. The dark state does not couple to the cavities field mode.(b) Eigenstates in the uncoupled basis. The transition rates are always proportional to the number of excitations in the system.

simulations (blue lines).

Notably, the physical system investigated here also allows for the experimental investigation of a situation which Dicke has denoted as single atom superradiance in his initial Gedankenexperiment, an effect surprising at the time, in which a single emitter in the excited state $|e\rangle$ decays at an enhanced rate in the presence of a second emitter, even when that second emitter is in its ground state $|g\rangle$ (Fig. 7.3d). Here the initial state $|ge\rangle$ can be decomposed into a superposition $(|B\rangle + |D\rangle)/\sqrt{2}$ of a bright $|B\rangle = (|ge\rangle + |eg\rangle)/\sqrt{2}$ and a dark state $|D\rangle = (|ge\rangle - |eg\rangle)/\sqrt{2}$. Half of the initial excitation remains trapped in $|D\rangle$ while the other half decays at twice the rate from the state $|B\rangle$, as pointed out by Dicke in his original argument [Dicke54]. Again the measured data is in agreement with solutions of simple coupled rate equations, namely $\Delta P(t) = P_0 \, e^{-2\bar{\Gamma}_\kappa t} - \bar{P}(t)$ (Fig. 7.3, black lines) [Gross82].

7.4 Reconstruction of field correlations

To further characterize the superradiant decay of the two-qubit ensemble, we have fully reconstructed the single mode density matrix of the emitted field using a statistical analysis of the measured quadrature ampli-

a $|g+e, g+e\rangle/2$ **b** $|g+e, g-e\rangle/2$
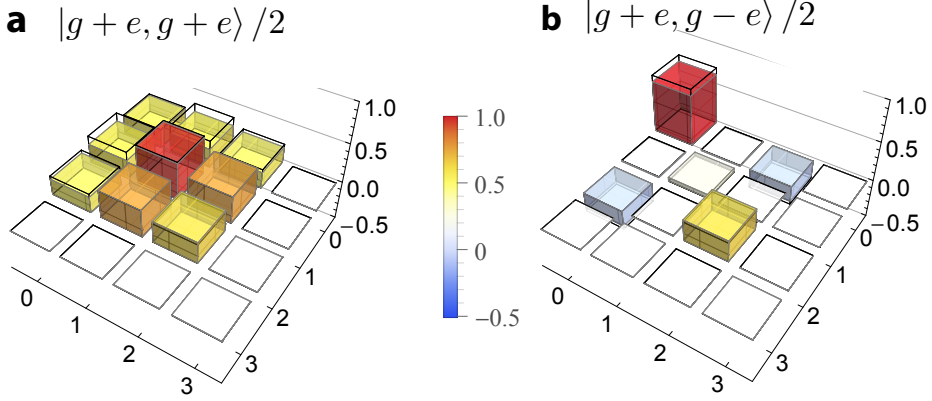
Figure 7.5: Real part of the measured density matrix ρ (colored bars) compared to expected values ρ_+ and ρ_- (wire frames) for initial qubit states **a** $(|g\rangle + |e\rangle)(|g\rangle + |e\rangle)/2$ and **b** $(|g\rangle + |e\rangle)(|g\rangle - |e\rangle)/2$. The imaginary part was measured to be $0 \pm \sigma = 0 \pm 0.012$ for (a) and 0 ± 0.037 for (b)

tudes [Eichler12]. The tomographic measurements were performed using the techniques discussed in Ref. [Eichler12] making use of a parametric amplifier [Eichler14] operated in the phase preserving mode to reduce the required integration time. Any initial pure and separable two qubit state brought into resonance with the cavity can be expressed in the coupled atomic basis states as $\alpha |gg\rangle + \delta |D\rangle + \beta |B\rangle + \gamma |ee\rangle$. The resulting photonic state is in general a mixed state obtained by tracing over $|D\rangle$ and reads $\delta^2 |0\rangle \langle 0| + (1 - \delta^2) |\Psi_B\rangle \langle \Psi_B|$ with $\Psi_B = (1 - \delta^2)^{-1/2} (\alpha |0\rangle + \beta |1\rangle + \gamma |2\rangle)$. We have reconstructed the density matrix of such output states for both qubits initially in the state $(|g\rangle + |e\rangle)/\sqrt{2}$ (Fig. 7.5a). The reconstructed density matrix clearly shows that the emitted field consists of a zero, one, or two photon Fock states and features pronounced coherences between those states (colored bars) in good agreement with the expected output state $\rho_+ = (1/2 |0\rangle + 1/\sqrt{2} |1\rangle + 1/2 |2\rangle)(1/2 \langle 2| + 1/\sqrt{2} \langle 1| + 1/2 \langle 2|)$ (wireframe). The state fidelity of the measured state ρ with respect to ρ_+ is $F = (Tr\sqrt{\sqrt{\rho_+}\rho\sqrt{\rho_+}})^2 = 0.94$.

Initially preparing the two qubits in equal superposition states $(|g\rangle + |e\rangle)/\sqrt{2} \otimes (|g\rangle - |e\rangle)/\sqrt{2}$ out of phase by π, either zero or two photons

are emitted, displaying a coherent component as well, while the probability for measuring a single photon vanishes (Fig. 7.5b), compatible with the expected mixed state of the form $\rho_- = 1/2 \, |0\rangle \, \langle 0| + 1/4(|0\rangle - |2\rangle)(\langle 2| - \langle 0|)$ with a fidelity of F=0.94.

8

Outlook

The work presented in this thesis discussed the collective dynamics of multiple two-level emitters coupled to a single mode of an electromagnetic field. Experiments were carried out both in the strong and in the weak coupling limit of cavity QED.

Most experiments with a strong motivation towards quantum information processing were realized in the first of the two mentioned regimes, as the strong coupling rates allow the fast and efficient generation of highly entangled states, as was also demonstrated in this thesis.

The bad cavity regime in contrast was previously almost unexamined in the field of circuit QED. Here a variety of interesting experiments are still outstanding which promise to contribute to a deeper understanding of basic quantum optical effects. In the context of superradiance, the multi-level structure of the transmon allows to include higher levels into the observation of collective decays, giving rise to multi-color superradiance [Hayn11]. Also the observation of superradiant phase transitions, so far demonstrated by coupling a Bose-Einstein condensate to a single mode of an open optical cavity [Baumann10], could be extended to include multiple levels and thus built a useful test bed for more complicated multi-level Dicke type Hamiltonians [Hayn11].

Superradiance is an effect which up to now was only related to two-level systems. Nevertheless it is expected that also harmonic systems should show similar signatures indicating a collective decay. So far it was very difficult to engineer a common reservoir interaction for an ensemble of harmonic

oscillators. The on-chip integration of multiple microwave transmission line resonators is certainly within reach of current circuit QED fabrication techniques and would allow for the first experimental study of harmonic oscillator superradiance [Delanty12]. In this context the recording of two-time correlation functions would be of special interest and would well meet the abilities to analyze the statistical properties of emitted microwave photons with techniques that have been developed in the past [Eichler12].

Furthermore the control over small superradiating ensembles may prove essential for experiments exploring entanglement by dissipation [Schneider02, Härkönen09, González-Tudela13, Lin13, Shankar13]. Here the coupling of the qubits to a common electromagnetic environment, represented by the lossy cavity, is the key resource for the entanglement generation. A main advantage of this attempt is that entanglement is arising in the steady state of the system once the qubits are coherently and simultaneously driven. Therefore high fidelities can be achieved without requiring precise control over microwave and flux pulses.

Another novel entanglement-generating protocol that could possibly be implemented in the bad cavity regime is measurement-induced entanglement [Julsgaard12]. Here the required coherent correlations between multiple qubits are established as a consequence of the outcome of a measurement process, which is either given by a quantum-non-demolition measurement or as a result of a single quantum jump. The feasibility of such a protocol has already been demonstrated by time-resolved, continuous parity measurements of two superconducting qubits. In the same instance it was shown that the inclusion of feedback techniques may transform entanglement generation from probabilistic to fully deterministic [Ristè13].

The reliable transfer of unknown quantum states is a key requirement for large quantum networks [Kimble08]. The realization of the complete teleportation protocol was successfully demonstrated recently [Steffen13b]. In addition to the *conventional* teleportation algorithms, superradiance, especially in the context of reservoir-induced entanglement, might be a promising tool to further pursue this direction [Chen05].

Bibliography

[Altomare10]   F. Altomare, J. I. Park, K. Cicak, M. A. Sillanpää, M. S. Allman, D. Li, A. Sirois, J. A. Strong, W. J. D., and R. W. Simmonds. "Tripartite interactions between two phase qubits and a resonant cavity." *Nat. Phys.*, **6**, 777 – 781 (2010). Cited on pages 69 and 70.

[Astafiev10]   O. Astafiev, A. M. Zagoskin, A. A. Abdumalikov Jr., Y. A. Pashkin, T. Yamamoto, K. Inomata, Y. Nakamura, and J. S. Tsai. "Resonance fluorescence of a single artificial atom." *Science*, **327**, 840–843 (2010). Cited on page 20.

[Awschalom13]   D. D. Awschalom, L. C. Bassett, A. S. Dzurak, E. L. Hu, and J. R. Petta. "Quantum spintronics: Engineering and manipulating atom-like spins in semiconductors." *Science*, **339**, 1174–1179 (2013). Cited on page 3.

[Barends14]   R. Barends, J. Kelly, A. Megrant, A. Veitia, D. Sank, E. Jeffrey, T. C. White, J. Mutus, A. G. Fowler, B. Campbell, Y. Chen, Z. Chen, B. Chiaro, A. Dunsworth, C. Neill, P. OʼMalley, P. Roushan, A. Vainsencher, J. Wenner, A. N. Korotkov, A. N. Cleland, and J. M. Martinis. "Superconducting quantum circuits at the surface code threshold for fault tolerance." *Nature*, **508**, 500–503 (2014). Cited on page 57.

[Baumann10]   K. Baumann, G. Guerlin, F. Brennecke, and T. Esslinger. "The Dicke quantum phase transition in a superfluid gas coupled to an optical cavity." *Nature*, **464**, 1301 (2010). Cited on page 91.

[Baur12a]   M. Baur. *Realizing quantum gates and algorithms with three superconducting qubits.* Ph.D. thesis, ETH Zurich (2012). Cited on pages 56 and 58.

[Baur12b]   M. Baur, A. Fedorov, L. Steffen, S. Filipp, M. P. da Silva, and A. Wallraff. "Benchmarking a quantum teleportation protocol in su-

perconducting circuits using tomography and an entanglement witness." *Phys. Rev. Lett.*, **108**, 040502 (2012). Cited on page 70.

[Bernardot92] F. Bernardot, P. Nussenzveig, M. Brune, J. M. Raimond, and S. Haroche. "Vacuum Rabi splitting observed on a microscopic atomic sample in a microwave cavity." *Europhys. Lett.*, **17**, 33–38 (1992). Cited on page 69.

[Bernien13] H. Bernien, B. Hensen, W. Pfaff, G. Koolstra, M. S. Blok, L. Robledo, T. H. Taminiau, M. Markham, D. J. Twitchen, L. Childress, and R. Hanson. "Heralded entanglement between solid-state qubits separated by three metres." *Nature*, **497**, 86–90 (2013). Cited on page 3.

[Bianchetti09] R. Bianchetti, S. Filipp, M. Baur, J. M. Fink, M. Göppl, P. J. Leek, L. Steffen, A. Blais, and A. Wallraff. "Dynamics of dispersive single-qubit readout in circuit quantum electrodynamics." *Phys. Rev. A*, **80**, 043840 (2009). Cited on page 34.

[Bianchetti10] R. Bianchetti. *Control and readout of a superconducting artificial atom.* Ph.D. thesis, ETH Zurich (2010). Cited on pages 35, 36, 49, 55 and 57.

[Bishop10] L. S. Bishop, E. Ginossar, and S. M. Girvin. "Response of the strongly driven jaynes-cummings oscillator." *Phys. Rev. Lett.*, **105**, 100505 (2010). Cited on page 36.

[Boissonneault10] M. Boissonneault, J. M. Gambetta, and A. Blais. "Improved superconducting qubit readout by qubit-induced nonlinearities." *Phys. Rev. Lett.*, **105**, 100504–4 (2010). Cited on page 36.

[Bonifacio71] R. Bonifacio, P. Schwendimann, and F. Haake. "Quantum statistical theory of superradiance. i." *Physical Review A*, **4**, 302–313 (1971). Cited on page 84.

[Bouchiat98] V. Bouchiat, D. Vion, P. Joyez, D. Esteve, and M. H. Devoret. "Quantum coherence with a single Cooper pair." *Phys. Scr.*, **T76**, 165–170 (1998). Cited on page 8.

[Bozyigit11] D. Bozyigit, C. Lang, L. Steffen, J. M. Fink, C. Eichler, M. Baur, R. Bianchetti, P. J. Leek, S. Filipp, A. Wallraff, M. P. da Silva, and A. Blais. "Correlation measurements of individual microwave photons emitted from a symmetric cavity." *J. Phys.: Conf. Ser.*, **264**, 012024–8 (2011). Cited on pages 40, 58 and 73.

[Brennecke07] F. Brennecke, T. Donner, S. Ritter, T. Bourdel, M. Kohl, and T. Esslinger. "Cavity QED with a Bose-Einstein condensate." *Nature*, **450**, 268–271 (2007). Cited on page 69.

[Burkhard12] S. Burkhard. *Optimization of transmon design for longer coherence time.* Master's thesis, ETH Zurich (2012). Cited on page 19.

[Cao10] K. Cao, Z.-W. Zhou, G.-C. Guo, and L. He. "Efficient numerical method to calculate the three-tangle of mixed states." *Phys. Rev. A*, **81**, 034302– (2010). Cited on page 76.

[Carmichael08] H. J. Carmichael. *Statistical Methods in Quantum Optics 2: Non-Classical Fields.* Springer-Verlag, Berlin (2008). Cited on page 85.

[Chang13] J. B. Chang, M. R. Vissers, A. D. Corcoles, M. Sandberg, J. Gao, D. W. Abraham, J. M. Chow, J. M. Gambetta, M. B. Rothwell, G. A. Keefe, M. Steffen, and D. P. Pappas. "Improved superconducting qubit coherence using titanium nitride." *Appl. Phys. Lett.*, **103**, 012602 (2013). Cited on page 57.

[Chen05] Y.-N. Chen, C. Li, D.-S. Chuu, and T. Brandes. "Proposal for teleportation of charge qubits via super-radiance." *New J. Phys.*, **7**, 172–181 (2005). Cited on page 92.

[Childs96] J. J. Childs, K. An, M. S. Otteson, R. R. Dasari, and M. S. Feld. "Normal-mode line shapes for atoms in standing-wave optical resonators." *Phys. Rev. Lett.*, **77**, 2901– (1996). Cited on page 69.

[Chiorescu04] I. Chiorescu, P. Bertet, K. Semba, Y. Nakamura, C. J. P. M. Harmans, and J. E. Mooij. "Coherent dynamics of a flux qubit coupled to a harmonic oscillator." *Nature, **431**, 159–162 (2004).* Cited on page 64.

[Clarke06] J. Clarke and A. Braginsky. *The SQUID Handbook.* Wiley-VCH (2006). Cited on page 5.

[Clarke08] J. Clarke and F. K. Wilhelm. "Superconducting quantum bits." *Nature, **453**, 1031–1042 (2008).* Cited on pages 3 and 5.

[Clerk10] A. A. Clerk, F. Marquardt, and J. G. E. Harris. "Quantum measurement of phonon shot noise." *Phys. Rev. Lett.*, **104**, 213603 (2010). Cited on page 20.

[Colombe07] Y. Colombe, T. Steinmetz, G. Dubois, F. Linke, D. Hunger, and J. Reichel. "Strong atom-field coupling for Bose-Einstein condensates in an optical cavity on a chip." *Nature, **450**, 272–276 (2007).* Cited on page 69.

[Delanty11] M. Delanty, S. Rebic, and J. Twamley. "Superradiance and phase multistability in circuit quantum electrodynamics." *New J. Phys.*, **13**, 053032 (2011). Cited on pages 38, 68, 84, 85 and 86.

[Delanty12] M. Delanty, S. Rebić, and J. Twamley. "Novel collective effects in integrated photonics." *The European Physical Journal D*, **66**, 1–7 (2012). Cited on page 92.

[DeVoe96] R. G. DeVoe and R. G. Brewer. "Observation of superradiant and subradiant spontaneous emission of two trapped ions." *Phys. Rev. Lett.*, **76**, 2049–2052 (1996). Cited on page 81.

[Devoret97] M. H. Devoret. "Quantum fluctuations in electrical circuits." In S. Reynaud, E. Giacobino, and J. Zinn-Justin editors, "Quantum Fluctuations: Les Houches Session LXIII," 351–386. Elsevier (1997). Cited on page 6.

[Devoret13]   M. Devoret and R. J. Schoelkopf. "Superconducting circuits for quantum information: An outlook." *Science*, **339**, 1169–1174 (2013). Cited on page 3.

[DiCarlo09]   L. DiCarlo, J. M. Chow, J. M. Gambetta, L. S. Bishop, B. R. Johnson, D. I. Schuster, J. Majer, A. Blais, L. Frunzio, S. M. Girvin, and R. J. Schoelkopf. "Demonstration of two-qubit algorithms with a superconducting quantum processor." *Nature*, **460**, 240–244 (2009). Cited on pages 35 and 58.

[DiCarlo10]   L. DiCarlo, M. D. Reed, L. Sun, B. R. Johnson, J. M. Chow, J. M. Gambetta, L. Frunzio, S. M. Girvin, M. H. Devoret, and R. J. Schoelkopf. "Preparation and measurement of three-qubit entanglement in a superconducting circuit." *Nature*, **467**, 574–578 (2010). Cited on pages 36, 37 and 70.

[Dicke54]   R. H. Dicke. "Coherence in spontaneous radiation processes." *Phys. Rev.*, **93**, 99–110 (1954). Cited on pages 69, 70 and 88.

[Duan10]   L.-M. Duan and C. Monroe. "Colloquium: Quantum networks with trapped ions." *Rev. Mod. Phys.*, **82**, 1209–1224 (2010). Cited on page 3.

[Dür00]   W. Dür, G. Vidal, and J. I. Cirac. "Three qubits can be entangled in two inequivalent ways." *Phys. Rev. A*, **62**, 062314 (2000). Cited on page 70.

[Eibl04]   M. Eibl, N. Kiesel, M. Bourennane, C. Kurtsiefer, and H. Weinfurter. "Experimental realization of a three-qubit entangled *w* state." *Phys. Rev. Lett.*, **92**, 077901 (2004). Cited on page 70.

[Eichler11]   C. Eichler, D. Bozyigit, C. Lang, L. Steffen, J. Fink, and A. Wallraff. "Experimental state tomography of itinerant single microwave photons." *Phys. Rev. Lett.*, **106**, 220503–4 (2011). Cited on page 49.

[Eichler12]   C. Eichler, D. Bozyigit, and A. Wallraff. "Characterizing quantum microwave radiation and its entanglement with superconducting qubits using linear detectors." *Phys. Rev. A*, **86**, 032106 (2012). Cited on pages 40, 49, 89 and 92.

[Eichler13]   C. Eichler. *Experimental Characterization of Quantum Microwave Radiation and its Entanglement with a Superconducting Qubit*. Ph.D. thesis, ETH Zurich (2013). Cited on pages 13, 38 and 39.

[Eichler14]   C. Eichler and A. Wallraff. "Controlling the dynamic range of a josephson parametric amplifier." *EPJ Quantum Technology*, **1**, 2 (2014). Cited on pages 38 and 89.

[Enss05]   C. Enss and S. Hunklinger. *Low-Temperature Physics*. Springer-Verlag Berlin Heidelberg (2005). Cited on page 28.

[Eschner01]   J. Eschner, C. Raab, F. Schmidt-Kaler, and R. Blatt. "Light interference from single atoms and their mirror images." *Nature*, **413**, 495–498 (2001). Cited on page 81.

[Fedorov12]   A. Fedorov, L. Steffen, M. Baur, M. P. da Silva, and A. Wallraff. "Implementation of a Toffoli gate with superconducting circuits." *Nature, 481*, 170–172 (2012). Cited on page 70.

[Filipp09]   S. Filipp, P. Maurer, P. J. Leek, M. Baur, R. Bianchetti, J. M. Fink, M. Göppl, L. Steffen, J. M. Gambetta, A. Blais, and A. Wallraff. "Two-qubit state tomography using a joint dispersive readout." *Phys. Rev. Lett., 102*, 200402 (2009). Cited on pages 35, 71, 72 and 75.

[Filipp11]   S. Filipp, M. Göppl, J. M. Fink, M. Baur, R. Bianchetti, L. Steffen, and A. Wallraff. "Multimode mediated qubit-qubit coupling and dark-state symmetries in circuit quantum electrodynamics." *Phys. Rev. A, 83*, 063827 (2011). Cited on pages 81 and 82.

[Fink09]   J. M. Fink, R. Bianchetti, M. Baur, M. Göppl, L. Steffen, S. Filipp, P. J. Leek, A. Blais, and A. Wallraff. "Dressed collective qubit states and the Tavis-Cummings model in circuit QED." *Phys. Rev. Lett., 103*, 083601–4 (2009). Cited on pages 69 and 70.

[Fink10a]   J. Fink. *Quantum nonlinearities in strong coupling circuit QED*. Ph.D. thesis, ETH Zurich (2010). Cited on pages 18, 22, 43 and 49.

[Fink10b]   J. M. Fink, L. Steffen, P. Studer, L. S. Bishop, M. Baur, R. Bianchetti, D. Bozyigit, C. Lang, S. Filipp, P. J. Leek, and A. Wallraff. "Quantum-to-classical transition in cavity quantum electrodynamics." *Phys. Rev. Lett., 105*, 163601 (2010). Cited on page 49.

[Fleischhauer05]   M. Fleischhauer, A. İmamoğlu, and J. P. Marangos. "Electromagnetically induced transparency: Optics in coherent media." *Rev. Mod. Phys., 77*, 633673 (2005). Cited on page 46.

[Fourie11]   C. J. Fourie, O. Wetzstein, T. Ortlepp, and J. Kunert. "Three-dimensional multi-terminal superconductive integrated circuit inductance extraction." *Superconductor Science and Technology*, 24, 125015 (2011). Cited on page 58.

[Gambetta11a]   J. M. Gambetta, A. A. Houck, and A. Blais. "Superconducting qubit with Purcell protection and tunable coupling." *Phys. Rev. Lett., 106*, 030502 (2011). Cited on page 55.

[Gambetta11b]   J. M. Gambetta, F. Motzoi, S. T. Merkel, and F. K. Wilhelm. "Analytic control methods for high-fidelity unitary operations in a weakly nonlinear oscillator." *Phys. Rev. A, 83*, 012308–13 (2011). Cited on page 71.

[Gerry05]   C. Gerry and P. L. Knight. *Introductory Quantum Optics*. Cambridge University Press (2005). Cited on page 33.

[González-Tudela13]   A. González-Tudela and D. Porras. "Mesoscopic entanglement induced by spontaneous emission in solid-state quantum optics." *Phys. Rev. Lett.*, 110, 080502 (2013). Cited on page 92.

Bibliography

[Göppl09]   M. Göppl. *Engineering Quantum Electronic Chips - Realization and Characterization of Circuit Quantum Electrodynamics Systems*. Ph.D. thesis, ETH Zurich (2009). Cited on pages 11, 12 and 13.

[Govenius12]   J. Govenius. *Single-Shot Qubit Readout in Circuit QED using Parametric Amplification*. Master's thesis, ETH Zurich (2012). Cited on page 39.

[Gross76]   M. Gross, C. Fabre, P. Pillet, and S. Haroche. "Observation of near-infrared dicke superradiance on cascading transitions in atomic sodium." *Phys. Rev. Lett.*, **36**, 1035–1038 (1976). Cited on page 81.

[Gross82]   M. Gross and S. Haroche. "Superradiance: An essay on the theory of collective spontaneous emission." *Physics Reports*, **93**, 301 – 396 (1982). Cited on pages 81, 86 and 88.

[Groszkowski11] P. Groszkowski, A. G. Fowler, F. Motzoi, and F. K. Wilhelm. "Tunable coupling between three qubits as a building block for a superconducting quantum computer." *Physical Review B*, **84**, 144516 (2011). Cited on page 58.

[Gühne09]   O. Gühne and G. Tóth. "Entanglement detection." *Physics Reports*, **474**, 1 – 75 (2009). Cited on page 76.

[Häffner08]   H. Häffner, C. F. Roos, and R. Blatt. "Quantum computing with trapped ions." *Physics Reports-review Section of Physics Letters*, **469**, 155–203 (2008). Cited on page 3.

[Hanson07]   R. Hanson, L. P. Kouwenhoven, J. R. Petta, S. Tarucha, and L. M. K. Vandersypen. "Spins in few-electron quantum dots." *Rev. Mod. Phys.*, **79**, 1217–1265 (2007). Cited on page 3.

[Härkönen09]   K. Härkönen, F. Plastina, and S. Maniscalco. "Dicke model and environment-induced entanglement in ion-cavity qed." *Phys. Rev. A*, **80**, 033841 (2009). Cited on page 92.

[Haroche92]   S. Haroche. *Fundamental Systems in Quantum Optics*, chapter Cavity quantum electrodynamics. Elsevier, New York (1992). Cited on page 33.

[Haroche06]   S. Haroche and J.-M. Raimond. *Exploring the Quantum: Atoms, Cavities, and Photons*. Oxford University Press, New York, USA (2006). Cited on page 82.

[Haroche13]   S. Haroche. "Nobel lecture: Controlling photons in a box and exploring the quantum to classical boundary." *Rev. Mod. Phys.*, **85**, 1083–1102 (2013). Cited on page 3.

[Hayn11]   M. Hayn, C. Emary, and T. Brandes. "Phase transitions and dark-state physics in two-color superradiance." *Phys. Rev. A*, **84**, 053856 (2011). Cited on page 91.

[Heinzen87]   D. J. Heinzen and M. S. Feld. "Vacuum radiative level shift and spontaneous-emission linewidth of an atom in an optical resonator." *Phys. Rev. Lett.*, **59**, 2623–2626 (1987). Cited on page 85.

[Heinzle12]   L. Heinzle. *Pump cancellation for a parametric amplifier.* Master's thesis, Laboratory of solid state physics, ETH Zurich (2012). Cited on page 39.

[Herskind09]   P. F. Herskind, A. Dantan, J. P. Marler, M. Albert, and M. Drewsen. "Realization of collective strong coupling with ion coulomb crystals in an optical cavity." *Nat. Phys.*, **5**, 494–498 (2009). Cited on page 69.

[Hofheinz08]   M. Hofheinz, E. M. Weig, M. Ansmann, R. C. Bialczak, E. Lucero, M. Neeley, A. D. O'Connell, H. Wang, J. M. Martinis, and A. N. Cleland. "Generation of Fock states in a superconducting quantum circuit." *Nature,* **454**, 310–314 (2008). Cited on page 64.

[Houck07]   A. Houck, D. Schuster, J. Gambetta, J. Schreier, B. Johnson, J. Chow, L. Frunzio, J. Majer, M. Devoret, S. Girvin, and R. Schoelkopf. "Generating single microwave photons in a circuit." *Nature,* **449**, 328–331 (2007). Cited on page 18.

[Julsgaard12] B. Julsgaard and K. Mølmer. "Measurement-induced two-qubit entanglement in a bad cavity: Fundamental and practical considerations." *Phys. Rev. A*, **85**, 032327 (2012). Cited on page 92.

[Kamon94]   M. Kamon, M. J. Tsuk, and J. K. White. "Fasthenry: A multipole-accelerated 3-d inductance extraction program." *Microwave Theory and Techniques, IEEE Transactions on*, **42**, 1750–1758 (1994). Cited on page 58.

[Kimble08]   H. J. Kimble. "The quantum internet." *Nature,* **453**, 1023–1030 (2008). Cited on page 92.

[Koch07]   J. Koch, T. M. Yu, J. Gambetta, A. A. Houck, D. I. Schuster, J. Majer, A. Blais, M. H. Devoret, S. M. Girvin, and R. J. Schoelkopf. "Charge-insensitive qubit design derived from the Cooper pair box." *Phys. Rev. A*, **76**, 042319 (2007). Cited on pages 8, 24, 33, 57 and 70.

[Kok07]   P. Kok, W. J. Munro, K. Nemoto, T. C. Ralph, J. P. Dowling, and G. J. Milburn. "Linear optical quantum computing with photonic qubits." *Rev. Mod. Phys.*, **79**, 135–174 (2007). Cited on page 3.

[Kubo10]   Y. Kubo, F. R. Ong, P. Bertet, D. Vion, V. Jacques, D. Zheng, A. Dréau, J.-F. Roch, A. Auffeves, F. Jelezko, J. Wrachtrup, M. F. Barthe, P. Bergonzo, and D. Esteve. "Strong coupling of a spin ensemble to a superconducting resonator." *Phys. Rev. Lett.*, **105**, 140502 (2010). Cited on page 69.

[Lalumière13] K. Lalumière, B. C. Sanders, A. F. van Loo, A. Fedorov, A. Wallraff, and A. Blais. "Input-output theory for waveguide qed with an ensemble of inhomogeneous atoms." *Phys. Rev. A*, **88**, 043806 (2013). Cited on page 82.

[Leek09]   P. J. Leek, S. Filipp, P. Maurer, M. Baur, R. Bianchetti, J. M. Fink, M. Göppl, L. Steffen, and A. Wallraff. "Using sideband transitions for two-qubit operations in superconducting circuits." *Phys. Rev. B*, **79**, 180511 (2009). Cited on page 35.

Bibliography

[Lehmberg70]   R. H. Lehmberg. "Radiation from an n-atom system. i. general formalism." *Phys. Rev. A*, **2**, 883–888 (1970). Cited on page 84.

[Lin13]   Y. Lin, J. P. Gaebler, F. Reiter, T. R. Tan, R. Bowler, A. S. Sorensen, D. Leibfried, and D. J. Wineland. "Dissipative production of a maximally entangled steady state of two quantum bits." *Nature*, **504**, 415–418 (2013). Cited on page 92.

[López07]   C. E. López, H. Christ, J. C. Retamal, and E. Solano. "Effective quantum dynamics of interacting systems with inhomogeneous coupling." *Phys. Rev. A*, **75**, 033818 (2007). Cited on page 74.

[Majer07]   J. Majer, J. M. Chow, J. M. Gambetta, J. Koch, B. R. Johnson, J. A. Schreier, L. Frunzio, D. I. Schuster, A. A. Houck, A. Wallraff, A. Blais, M. H. Devoret, S. M. Girvin, and R. J. Schoelkopf. "Coupling superconducting qubits via a cavity bus." *Nature*, **449**, 443–447 (2007). Cited on page 18.

[Mlynek12]   J. A. Mlynek, A. A. Abdumalikov, J. M. Fink, L. Steffen, M. Baur, C. Lang, A. F. van Loo, and A. Wallraff. "Demonstrating W-type entanglement of Dicke states in resonant cavity quantum electrodynamics." *Phys. Rev. A*, **86**, 053838 (2012). Cited on page 70.

[Mlynek14]   J. A. Mlynek, A. A. Abdumalikov Jr, C. Eichler, and A. Wallraff. "Observation of dicke superradiance for two artificial atoms in a cavity with high decay rate." *Nature Communications*, **6** (2014). Cited on page 82.

[Monroe13]   C. Monroe and J. Kim. "Scaling the ion trap quantum processor." *Science*, **339**, 1164 (2013). Cited on page 3.

[Motzoi09]   F. Motzoi, J. M. Gambetta, P. Rebentrost, and F. K. Wilhelm. "Simple pulses for elimination of leakage in weakly nonlinear qubits." *Phys. Rev. Lett.*, **103**, 110501 (2009). Cited on page 55.

[Münstermann00]   P. Münstermann, T. Fischer, P. Maunz, P. W. H. Pinkse, and G. Rempe. "Observation of cavity-mediated long-range light forces between strongly coupled atoms." *Phys. Rev. Lett.*, **84**, 4068– (2000). Cited on page 69.

[Nakamura02]   Y. Nakamura, Y. A. Pashkin, T. Yamamoto, and J. S. Tsai. "Charge echo in a Cooper-pair box." *Phys. Rev. Lett.*, **88**, 047901 (2002). Cited on page 57.

[Neeley10]   M. Neeley, R. C. Bialczak, M. Lenander, E. Lucero, M. Mariantoni, A. D. O'Connell, D. Sank, H. Wang, M. Weides, J. Wenner, Y. Yin, T. Yamamoto, A. N. Cleland, and J. M. Martinis. "Generation of three-qubit entangled states using superconducting phase qubits." *Nature*, **467**, 570–573 (2010). Cited on page 70.

[Ott11]   H. W. Ott. *Electromagnetic compatibility engineering.* John Wiley & Sons (2011). Cited on page 58.

[Pashkin09]   Y. A. Pashkin, O. Astafiev, T. Yamamoto, Y. Nakamura, and J. Tsai. "Josephson charge qubits: a brief review." *Quantum information processing*, **8**, 55–80 (2009). Cited on page 57.

[Pobell06]   F. Pobell. *Matter and Methods at Low Temperatures.* Springer, 3rd edition, (2006). Cited on pages 28 and 30.

[Pozar93]   D. M. Pozar. *Microwave Engineering.* Addison-Wesley Publishing Company (1993). Cited on page 14.

[Pozar11]   D. M. Pozar. *Microwave engineering.* John Wiley & Sons, Inc., 4th edition (2011). Cited on pages 10 and 12.

[Rabi37]   I. I. Rabi. "Space quantization in a gyrating magnetic field." *Phys. Rev.*, **51**, 652–654 (1937). Cited on page 55.

[Raimond82]   J. M. Raimond, P. Goy, M. Gross, C. Fabre, and S. Haroche. "Statistics of millimeter-wave photons emitted by a rydberg-atom maser: An experimental study of fluctuations in single-mode superradiance." *Phys. Rev. Lett.*, **49**, 1924–1927 (1982). Cited on page 81.

[Ramsey50]   N. F. Ramsey. "A molecular beam resonance method with separated oscillating fields." *Phys. Rev.*, **78**, 695–699 (1950). Cited on page 57.

[Reed10]   M. D. Reed, L. DiCarlo, B. R. Johnson, L. Sun, D. I. Schuster, L. Frunzio, and R. J. Schoelkopf. "High-fidelity readout in circuit quantum electrodynamics using the Jaynes-Cummings nonlinearity." *Phys. Rev. Lett.*, **105**, 173601–4 (2010). Cited on page 36.

[Rice88]   P. Rice and H. Carmichael. "Single-atom cavity-enhanced absorption. i. photon statistics in the bad-cavity limit." *Quantum Electronics, IEEE Journal of*, **24**, 1351–1366 (1988). Cited on page 46.

[Rice96]   P. Rice and R. Brecha. "Cavity induced transparency." *Optics communications*, **126**, 230–235 (1996). Cited on page 46.

[Ristè13]   D. Ristè, M. Dukalski, C. A. Watson, G. de Lange, M. J. Tiggelman, Y. M. Blanter, K. W. Lehnert, R. N. Schouten, and L. DiCarlo. "Deterministic entanglement of superconducting qubits by parity measurement and feedback." *Nature,* **502**, 350–354 (2013). Cited on pages 57 and 92.

[Rohlsberger10] R. Rohlsberger, K. Schlage, B. Sahoo, S. Couet, and R. Ruffer. "Collective Lamb Shift in Single-Photon Superradiance." *Science,* **328**, 1248–1251 (2010). Cited on page 81.

[Roos04]   C. F. Roos, M. Riebe, H. Häffner, W. Hänsel, J. Benhelm, G. P. T. Lancaster, C. Becher, F. Schmidt-Kaler, and R. Blatt. "Control and measurement of three-qubit entangled states." *Science,* **304**, 1478–1480 (2004). Cited on page 70.

[Saffman10]   M. Saffman, T. G. Walker, and K. Mølmer. "Quantum information with Rydberg atoms." *Rev. Mod. Phys.*, **82**, 2313–2363 (2010). Cited on page 3.

[Scheibner07]   M. Scheibner, T. Schmidt, L. Worschech, A. Forchel, G. Bacher, T. Passow, and D. Hommel. "Superradiance of quantum dots." *Nat. Phys.*, **3**, 106–110 (2007). Cited on page 81.

[Schmidlin09]   S. Schmidlin. *Generation of amplitude and phase controlled microwave pulses for qubit manipulation in Circuit QED.* Master's thesis, ETH Zurich (2009). Cited on page 56.

[Schneider02]   S. Schneider and G. Milburn. "Entanglement in the steady state of a collective-angular-momentum (dicke) model." *Physical Review A*, **65**, 042107 (2002). Cited on page 92.

[Schoelkopf02]   R. J. Schoelkopf, A. A. Clerk, S. M. Girvin, K. W. Lehnert, and M. H. Devoret. "Qubits as spectrometers of quantum noise." *cond-mat/0210247* (2002). Cited on page 20.

[Schoelkopf08]   R. J. Schoelkopf and S. M. Girvin. "Wiring up quantum systems." *Nature*, **451**, 664–669 (2008). Cited on page 82.

[Schuster05]   D. I. Schuster, A. Wallraff, A. Blais, L. Frunzio, R.-S. Huang, J. Majer, S. M. Girvin, and R. J. Schoelkopf. "AC Stark shift and dephasing of a superconducting qubit strongly coupled to a cavity field." *Phys. Rev. Lett.*, **94**, 123602 (2005). Cited on page 49.

[Schuster07]   D. I. Schuster. *Circuit Quantum Electrodynamics.* Ph.D. thesis, Yale University (2007). Cited on pages 43 and 49.

[Schwinger58]   J. Schwinger. *Selected papers on quantum electrodynamics.* Courier Dover Publications (1958). Cited on page 2.

[Scully97]   M. O. Scully and M. S. Zubairy. *Quantum Optics.* Cambridge University Press (1997). Cited on page 44.

[Shankar13]   S. Shankar, M. Hatridge, Z. Leghtas, K. M. Sliwa, A. Narla, U. Vool, S. M. Girvin, L. Frunzio, M. Mirrahimi, and M. H. Devoret. "Autonomously stabilized entanglement between two superconducting quantum bits." *Nature*, **504**, 419–422 (2013). Cited on page 92.

[Simons01]   R. N. Simons. *Coplanar waveguide circuits, components and systems.* Wiley Series in Microwave and Optical Engineering. Wiley Inter-Science (2001). Cited on page 10.

[Skribanowitz73]   N. Skribanowitz, I. P. Herman, J. C. MacGillivray, and M. S. Feld. "Observation of dicke superradiance in optically pumped hf gas." *Phys. Rev. Lett.*, **30**, 309–312 (1973). Cited on page 81.

[Smolin12]   J. A. Smolin, J. M. Gambetta, and G. Smith. "Efficient method for computing the maximum-likelihood quantum state from measurements with additive gaussian noise." *Phys. Rev. Lett.*, **108**, 070502 (2012). Cited on page 75.

[Steffen03]   M. Steffen, J. M. Martinis, and I. L. Chuang. "Accurate control of josephson phase qubits." *Phys. Rev. B*, **68**, 224518 (2003). Cited on page 54.

[Steffen13a]   L. Steffen. *Quantum Teleportation and Efficient Process Verification with Superconducting Circuits.* Ph.D. thesis, ETH Zurich (2013). Cited on pages 8, 19, 22 and 39.

[Steffen13b]   L. Steffen, Y. Salathe, M. Oppliger, P. Kurpiers, M. Baur, C. Lang, C. Eichler, G. Puebla-Hellmann, A. Fedorov, and A. Wallraff. "Deterministic quantum teleportation with feed-forward in a solid state system." *Nature,* **500**, 319–322 (2013). Cited on page 92.

[Steiger13]   D. Steiger. *Inductance calculations for the design of superconducting qubits.* Master's thesis, ETH Zurich (2013). Cited on page 58.

[Tavis68]   M. Tavis and F. W. Cummings. "Exact solution for an N-molecule-radiation-field Hamiltonian." *Phys. Rev.,* **170**, 379–384 (1968). Cited on pages 18, 69 and 70.

[Teklemariam02]   G. Teklemariam, E. M. Fortunato, M. A. Pravia, Y. Sharf, T. F. Havel, D. G. Cory, A. Bhattaharyya, and J. Hou. "Quantum erasers and probing classifications of entanglement via nuclear magnetic resonance." *Phys. Rev. A,* **66**, 012309 (2002). Cited on page 70.

[Thompson92]   R. J. Thompson, G. Rempe, and H. J. Kimble. "Observation of normal-mode splitting for an atom in an optical cavity." *Phys. Rev. Lett.,* **68**, 1132–1135 (1992). Cited on page 43.

[Thompson98]   R. J. Thompson, Q. A. Turchette, O. Carnal, and H. J. Kimble. "Nonlinear spectroscopy in the strong-coupling regime of cavity QED." *Phys. Rev. A,* **57**, 3084– (1998). Cited on page 69.

[Tuchman06]   A. K. Tuchman, R. Long, G. Vrijsen, J. Boudet, J. Lee, and M. A. Kasevich. "Normal-mode splitting with large collective cooperativity." *Phys. Rev. A,* **74**, 053821–4 (2006). Cited on page 69.

[Uhlenbeck30]   G. E. Uhlenbeck and L. S. Ornstein. "On the theory of the brownian motion." *Phys. Rev.,* **36**, 823–841 (1930). Cited on page 47.

[Vandersypen04]   L. M. K. Vandersypen and I. L. Chuang. "NMR techniques for quantum control and computation." *Rev. Mod. Phys.,* **76**, 1037 (2004). Cited on page 3.

[vanLoo13]   A. van Loo, A. Fedorov, K. Lalumière, B. Sanders, A. Blais, and A. Wallraff. "Photon-mediated interactions between distant artificial atoms." *Science,* **342**, 1494–1496 (2013). Cited on pages 81 and 82.

[Vion02]   D. Vion, A. Aassime, A. Cottet, P. Joyez, H. Pothier, C. Urbina, D. Esteve, and M. H. Devoret. "Manipulating the quantum state of an electrical circuit." *Science,* **296**, 886–889 (2002). Cited on page 57.

[Vion03]   D. Vion, A. Aassime, A. Cottet, P. Joyez, H. Pothier, C. Urbina, D. Esteve, and M. H. Devoret. "Rabi oscillations, Ramsey fringes and spin echoes in an electrical circuit." *Fortschritte der Physik,* **51**, 462–468 (2003). Cited on page 55.

[Wallraff04] A. Wallraff, D. I. Schuster, A. Blais, L. Frunzio, R.-S. Huang, J. Majer, S. Kumar, S. M. Girvin, and R. J. Schoelkopf. "Strong coupling of a single photon to a superconducting qubit using circuit quantum electrodynamics." *Nature,* **431**, 162–167 (2004). Cited on pages 18 and 43.

[Wallraff05] A. Wallraff, D. I. Schuster, A. Blais, L. Frunzio, J. Majer, S. M. Girvin, and R. J. Schoelkopf. "Approaching unit visibility for control of a superconducting qubit with dispersive readout." *Phys. Rev. Lett.,* **95**, 060501–4 (2005). Cited on pages 34 and 35.

[White02] G. K. White and P. J. Meeson. *Experimental Techniques in Low-Temperature Physics; 4th ed.* Monographs on the Physics and Chemistry of Materials. Oxford Univ. Press, Oxford (2002). Cited on pages 28 and 29.

[Wu10] H. Wu, R. E. George, J. H. Wesenberg, K. Mølmer, D. I. Schuster, R. J. Schoelkopf, K. M. Itoh, A. Ardavan, J. J. L. Morton, and G. A. D. Briggs. "Storage of multiple coherent microwave excitations in an electron spin ensemble." *Phys. Rev. Lett.,* **105**, 140503 (2010). Cited on page 69.

[Zhu90] Y. Zhu, D. J. Gauthier, S. E. Morin, Q. Wu, H. J. Carmichael, and T. W. Mossberg. "Vacuum rabi splitting as a feature of linear-dispersion theory: Analysis and experimental observations." *Phys. Rev. Lett.,* **64**, 2499–2502 (1990). Cited on page 46.

List of Publications

1. **J. A. Mlynek**, A. A. Abdumalikov Jr, C. Eichler, and A. Wallraff, "Observation of dicke superradiance for two artificial atoms in a cavity with high decay rate", *Nature Communications*, **6** (2014)

2. **J. A. Mlynek**, A. A. Abdumalikov, J. M. Fink, L. Steffen, M. Baur, C. Lang, A. F. van Loo, and A. Wallraff, "Demonstrating W-type entanglement of Dicke states in resonant cavity quantum electrodynamics", *Phys. Rev. A* **86**, 053838 (2012)

3. C. Eichler, Y. Salathe, **J. Mlynek**, S. Schmidt, and A. Wallraff, "Quantum-limited amplification and entanglement in coupled nonlinear resonators", *Phys. Rev. Lett.* **113**, 110502 (2013)

4. F. Nissen, J. M. Fink, **J. A. Mlynek**, A. Wallraff, and J. Keeling, "Collective suppression of linewidths in circuit qed", *Phys. Rev. Lett.* **110**, 203602 (2013)

5. M. Pechal, S. Berger, A. A. Abdumalikov Jr., J. M. Fink, **J. A. Mlynek**, L. Steffen, A. Wallraff, S. Filipp, "Geometric Phase and Nonadiabatic Effects in an Electronic Harmonic Oscillator", *Physical Review Letters* **108**, 170401 (2012)

6. A. C. Wilson, C. Ospelkaus, A. VanDevender, **J. A. Mlynek**, K. Brown, D. Leibfried, and D. Wineland, "A 750-mw, continuous-wave, solidstate laser source at 313 nm for cooling and manipulating trapped 9be+ ions", *Applied Physics B*, **105**, 741–748 (2011)

Acknowledgments

Throughout the years I spent working on this thesis, I received a lot of support from many people. Without them, the realization of this thesis would not have been possible.

First I would like to thank ANDREAS WALLRAFF for giving me the opportunity to work in the fascinating field of superconducting circuits. I deeply appreciate his advice and the his generosity in giving me the intellectual freedom to pursue my own projects and ideas. I thank him for his constant encouragement and his valuable advice.

I want to thank PATRICE BERTET, the co-examiner of my thesis, for commenting on the draft of this thesis and for the helpful and enjoyable discussions we had about the results.

I also would like to thank ABDUFARRUKH ABDUMALIKOV for being my first point of contact whenever I needed some serious input and help. I am still impressed about his broad knowledge on all aspects of the experiment and especially the deep theoretical insights that he was willing to constantly share. Both the overall success of this thesis as well as my personal education as a physicist benefitted greatly from his collaboration and friendship.

I would also like to thank CHRISTOPHER EICHLER for contributing to the experiments with great ambition and valuable guidance. His creative and cheerful spirit enriched all the numerous discussions about physics and everyday life.

I thank JOHANNES FINK for taking care of me during the early part of my thesis and for saving me from various pitfalls with his great experience, humor and patience. I would also like to express my thanks to MATTHIAS BAUR, who helped me a lot with the generation of all kind of crazy microwave pulses and who, together with GABRIEL PUEBLA, guided me into the beautiful Swiss mountains. Both of them were responsible for some unforgettable skiing and climbing experiences. I would like to thank CHRISTIAN LANG, who was a great office mate and the lab's master in FPGA programming. I thank LARS STEFFEN for being an always good-humored and helpful office mate and of invaluable help in the clean room, especially related to our nasty evaporator.

Of course I would like to express my gratitude to the whole QUDEV-team for making the past years such a fun time and the lab such a cheerful

and fruitful place to work.

Last but not least I would like to thank my family and friends for accompanying me all over the years and for being able to distract me from physics whenever I felt the need for it. I thank my parents DAGMAR UND JÜRGEN MLYNEK and my brother SIMON for their constant interest in my work and for always being there for me. I deeply thank MIRIAM for her love, her understanding, her patience and her endurance during all the time we spent together somewhere in between Berlin and Zurich.